12-2016

# Photoelectrochemical and photophysical studies of carbon nanotube and molybdenum disulfide based light harvesting devices

Hanyu Zhang
*Purdue University*

*Graduate School Form*
*30 Updated 12/26/2015*

**PURDUE UNIVERSITY**
**GRADUATE SCHOOL**
**Thesis/Dissertation Acceptance**

This is to certify that the thesis/dissertation prepared

By Hanyu Zhang

Entitled

PHOTOELECTROCHEMICAL AND PHOTOPHYSICAL STUDIES OF CARBON NANOTUBE AND MOLYBDENUM DISULFIDE BASED LIGHT HARVESTING DEVICES

For the degree of Doctor of Philosophy

Is approved by the final examining committee:

Jong Hyun Choi
Chair

David R. McMillin

You-Yeon Won

Liang Pan

To the best of my knowledge and as understood by the student in the Thesis/Dissertation Agreement, Publication Delay, and Certification Disclaimer (Graduate School Form 32), this thesis/dissertation adheres to the provisions of Purdue University's "Policy of Integrity in Research" and the use of copyright material.

Approved by Major Professor(s): Jong Hyun Choi

Approved by: Jay P. Gore 10/14/2016
Head of the Departmental Graduate Program Date

# PHOTOELECTROCHEMICAL AND PHOTOPHYSICAL STUDIES OF CARBON NANOTUBE AND MOLYBDENUM DISULFIDE BASED LIGHT HARVESTING DEVICES

A Dissertation

Submitted to the Faculty

of

Purdue University

by

Hanyu Zhang

In Partial Fulfillment of the

Requirements for the Degree

of

Doctor of Philosophy

December 2016

Purdue University

West Lafayette, Indiana

Dedicated

to

My Parents

My Wife, Enming, and Our Daughter, Wendy

谨以此文

献给

我的父母

我的妻子，恩铭，和我们的女儿，菀芝

# ACKNOWLEDGEMENTS

I owe my deepest gratitude to my advisor, Professor Jong Hyun Choi, for patient guidance, encouragement and serving a dedicated mentorship and showing me an outstanding model for the duration of my MS and PhD studies.

I would like to express my gratitude to Professor David McMillin, who provided plenty invaluable suggestions and continuously supported my research for past five years.

I would like to thank our collaborators, Matthew A. Bork, Sean N. Natoli, Professor Damien Voiry and Manish Chhowalla for constructive advices and valuable assistances.

I also would like to thank my peers, Jungwook Choi, Benjamin A. Baker, Tae-Gon Cha, Haorong Chen, Jing Pan, Feiran Li and Haodong Du with whom I have worked. For the students I mentored, Adalberto A. Gonzalez, Arjun Ramani, Morgan Sawyer and Kelley J. Riedy, I would like to express my thanks to them who provided many helps during the past few years.

Finally, I would like to acknowledge the National Science Foundation, the School of Mechanical Engineering at Purdue University for their support for my graduate studies.

TABLE OF CONTENTS

Page

# LIST OF TABLES

# LIST OF FIGURES

Figure Page

Figure Page

Figure Page

Figure Page

Figure Page

# LIST OF ABBREVIATIONS

SWCNT: single wall carbon nanotubes

Asc: L-ascorbic

DAsc: dehydroascorbic acid

ITO: indium tin oxide

PTFE: polytetrafluoroethylene

IPA: isopropyl alcohol

DMSO: dimethyl sulfoxide

TMDC: transition metal dichalcogenide

$H_2$T4: 5,10,15,20-tetra-(N-methyl-4-pyridyl)- porphyrin

ZnT4: zinc (II) 5,10,15,20-tetra-(N-methyl-4-pyridyl)- porphyrin

PtT4: platinum (II) 5,10,15,20-tetra-(N-methyl-4-pyridyl)- porphyrin

PdT4: palladium (II) 5,10,15,20-tetra-(N-methyl-4-pyridyl)- porphyrin

CuT4: copper (II) 5,10,15,20-tetra-(N-methyl-4-pyridyl)- porphyrin

ZnPP: zinc (II) protoporphyrin IX

FePP: iron (III) protoporphyrin IX

GaPP: gallium (III) protoporphyrin IX

$H_2$TPP: tetraphenylporphyrin

ZnTPP: zinc(II) tetraphenylporphyrin

HOMO: highest occupied molecular orbital

LUMO: lowest unoccupied molecular orbital

$MoS_2$: molybdenum disulfide

DSSC: dye sensitized solar cell

SEM: scanning electron microscopy

AFM: atomic force microscopy

RBM: radial breathing mode

CB: conduction band

CBM: conduction band minimum

VB: valence band

VBM: valence band maximum

InGaAs: indium gallium arsenide

# ABSTRACT

Zhang, Hanyu. Ph.D., Purdue University, December 2016. Photoelectrochemical and Photophysical Studies of Carbon Nanotube and Molybdenum Disulfide Based Light Harvesting Devices. Major Professor: Jong Hyun Choi, School of Mechanical Engineering.

There is a critical need in utilizing solar radiation as a renewable energy source. While photovoltaic solar cells are widely used, much attention has been devoted in the past decade to developing nanotechnology for potential cost reduction and improved device efficiency and reliability. Low-dimensional materials offer unique physical properties which may be exploited for solar energy harvesting and conversion. Understanding their fundamental properties and developing relevant manufacturing strategies will thus pave the road toward high-performance, cost-effective, light-harvesting devices.

This thesis has investigated single-wall carbon nanotubes (SWCNTs) and molybdenum disulfide ($MoS_2$) nanolayers for their light-harvesting ability in donor-acceptor systems. These materials were studied with three specific goals: (i) introducing innovative light-harvesting designs, (ii) understanding their fundamental photophysical and photoelectrochemical properties, and (iii) providing potential solutions to improve the system performance.

First, novel light-harvesting complexes were designed using semiconducting SWCNTs and cationic porphyrins as acceptors and donors, respectively. These complexes were assembled by synthetic DNA oligonucleotides that recognize porphyrins, while noncovalently functionalizing SWCNTs. The SWCNT-DNA-porphyrin hybrids were used to manufacture large-area thin films through solution-phase processing and membrane filtration methods. From extensive studies of optical absorption, emission, and photocurrents, new detailed insights on photo-processes were gained for photoelectrochemical conversion.

A regenerative donor-acceptor light-harvesting system was introduced and demonstrated to counteract photoinduced degradation of porphyrin molecules. The photo-damaged chromophores were dissociated from the complex by modulating the chemical environment, while DNA-SWCNTs were preserved. When fresh porphyrins were reintroduced and reassociated with DNA-SWCNTs, photocurrents were fully recovered. As proof-of-principle, A 50% increase in photocurrents was demonstrated through four successive regenerations within 90 minutes, compared to the complex without regeneration. Such dynamic strategy could improve the overall device efficiency and extend the operation lifetime.

Lastly, a novel solution-phase manufacturing process was developed to fabricate large-area two-dimensional $MoS_2$ nanolayers for light harvesting applications. The $MoS_2$ nanolayers were functionalized with 8 porphyrin species from 3 families to mitigate charge recombination by defects and small crystallites. A strong correlation between

porphyrin species and photocurrents was observed, where interfacial porphyrins suppress charge recombination within $MoS_2$ nanolayers, thus enhancing the photoelectrochemical performance of the devices. A photocurrent enhancement mechanism was proposed based on the energy difference between the valence band of $MoS_2$ and highest occupied molecular orbital level of porphyrins.

Overall, the innovative designs and the scientific insights on photophysics and photoelectrochemical conversion in this thesis will form the basis for developing next-generation solar energy harvesting devices.

# CHAPTER 1. INTRODUCTION

## 1.1 Solar Energy and Recent Advances

Fossil fuels started to be utilized from ancient age and became the dominant source of energy production at 20$^{th}$ century due to its vast supply and low-cost production or excavate. The rapidly increasing energy consumption due to human development are raising the competition over fossil fuel resources, causing increased economic pressures, especially potential environment and climate damage. By the year of 2050, at least 10 TW of carbon emission free power must be available, based on the estimation rate of worldwide growth in energy consumption, which is as much as the energy that produced today worldwide from all sources combined.[1-3] The clean or renewable energy production methods, such as geothermal, hydroelectric, wind power and solar energy, are candidates to provide this carbon emission free power, while the solar energy is the most abundant and accessible resource. For example, ~120,000 trillion W of solar radiation strike the earth, while the second highest resource, geothermal energy, integrated over earth's entire land surface, can provide only 1/10000 comparing to solar energy.[3] Yet, only 0.1 ‰ energy of solar radiation incident on the earth's surface is utilized worldwide, but only less than 1% of the world's energy are from solar energy.[4]

However, the challenge that prevents solar energy utilization as major energy resource is production cost compared to the economically cheap fossil fuel based production techniques.[3] The current utilization of solar energy relies on the conventional "first generation" crystalline silicon based systems. Although the silicon solar cell devices reach the converting efficiencies above 20%, the crystal growth processes of silicon are relative expensive which limits their vast production and deployment. The "second generation" solar cells are based on thin film technologies. The products, such as amorphous silicon [5], cadmium telluride (CdTe)[6] and copper indium gallium selenide (CIGS)[7], have overall advantage in efficiency vs. price but the costly elements used in second generation solar cells and deposition processes prevent their further penetration in energy market.[8] Meanwhile, further advancing techniques provide possible lower material cost and processing prices. These manufacturing-enabled based solar cells involve dye sensitized solar cells (DSSCs), organic, and polymer solar cells. [3, 8-15] The efficiencies from various types of solar cells and their development trend have been demonstrated in Figure 1.1. The developing nanotechnologies provide possible improving methods for next generation photovoltaic devices, by exploiting the properties of various materials.[3, 16-20]

This thesis explores the potential component materials for light harvesting, namely, single-wall carbon nanotubes (SWCNTs), porphyrins and $MoS_2$, and elucidated the photo-physical properties of these materials.

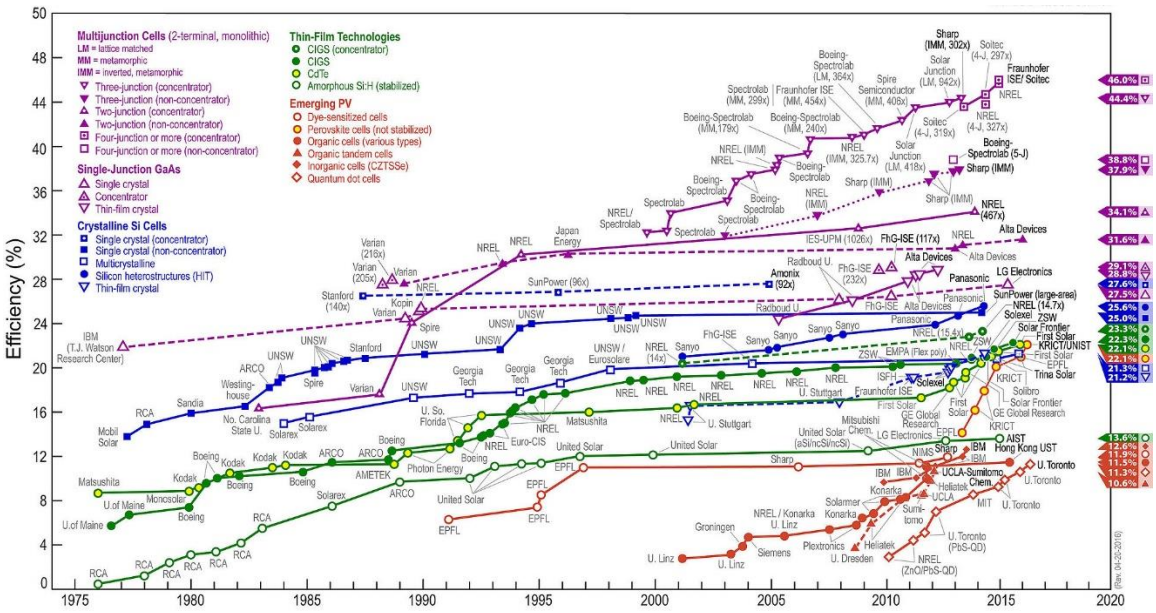


Figure 1.1. Recent Solar Cell Efficiencies Summary (http://www.nrel.gov/ncpv/).

## 1.2 Light Harvesting Applications of Carbon Nanotubes, Porphyrins and $MoS_2$

### 1.2.1 Single-Wall Carbon Nanotubes (SWCNTs)

Single-wall carbon nanotubes (SWCNTs) have been extensively studied in photoelectrochemical cells in solar energy applications due to their extraordinary optical and electronic properties.[21, 22] They have been explored as direct photoactive materials, charge separation enhancers and charge shuttling enhancer as well as electrode materials in solar cells.[23] In this section, the physical properties of SWCNTs and recent advances of SWCNTs in photovoltaics applications are briefly reviewed.

The physical properties of SWCNTs can be determined as a function of chirality (n, m) indices, such as electronic type.[24, 25] When (n-m) is divisible by 3, it is a metal, and otherwise a semiconductor.[25] The theoretical 1-D density of states is shown in Figure

1.2, including a semiconducting tubes (Figure 1.2a) and a metallic nanotube (Figure 1.2b). In Figure 1.2a, the forbidden energy region between the valence and conduction bands indicates a semiconducting nanotube, where (n, m) = (10, 0). In Figure 1.2b, a metallic SWCNT (n=9, m=0) gives continuous band of energy levels between the valence and conduction bands. The density of states structure based on chirality theory are consistent well with experimental results.[24]

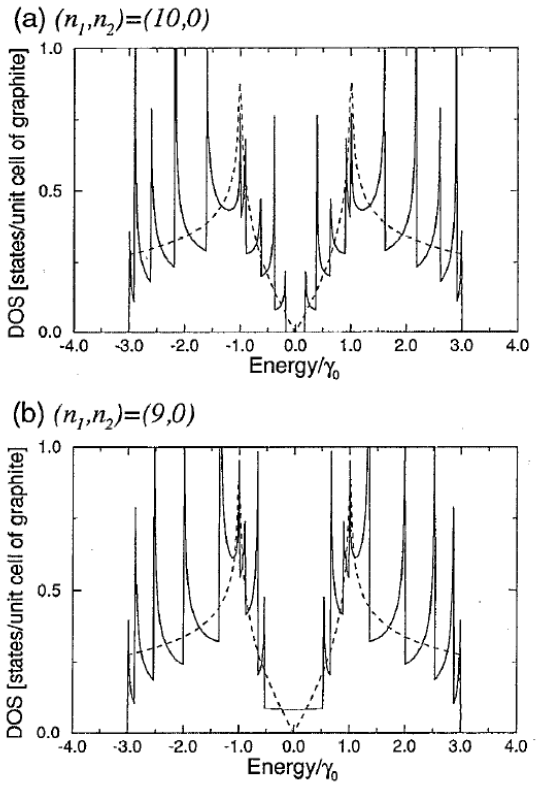


Figure 1.2. Density of Electronic States of Single-Walled Carbon Nanotubes. (a) Semiconducting SWCNT with Finite Bandgap. (b) Metallic SWCNT with Continuous Energy Levels (Saito, 1992).

To accurately access energy level transitions in SWCNTs, known as van Hove singularities, multiple studies have been investigated in individual nanotube dispersion.

The synthesis of nanotubes gives π-π stacked large bundles and combined both metallic and semiconducting SWCNTs.[26] The presence of metallic nanotubes in bundles will convert the electronic type toward metallic, increasing the charge recombination significantly.[26-28] With bundles of metallic behavior, it is difficult to observe distinct optical behaviors such as discrete absorption and photoluminescence. Thus, it is critical that SWCNTs need to be dispersed individually.

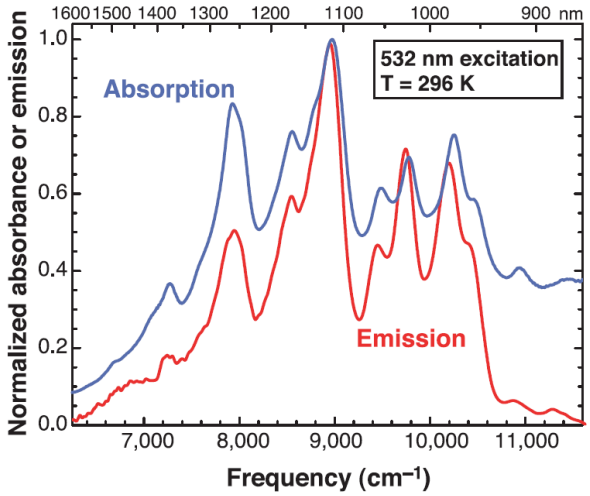


Figure 1.3. Absorption and Emission Spectra of Dispersed SWCNT, Showing near-Infrared van Hove Singularities of Several Species (O'Connell, 2002).

The nanotube fluorescence was observed for the first time back in 2002, after developing a processing method based on surfactant coated SWCNT via ultrasonication.[28] The absorption and photoluminescence peaks have been demonstrated as closely align with theoretical calculation.[28, 29] Figure 1.3 shows the corresponding absorption and emission of surfactant suspended SWCNT. The multiple peaks from the absorption and

photoluminescence transitions between the conduction band and valence band represent various species highly dispersed SWCNT in solution.[30]

Due to their 1D structure, and excellent conductivity, and similarity to the fluorine ($C_{60}$) molecules commonly explored in organic solar cells, carbon nanotubes can be served as a potential candidate for photoactive layers of solar cells, usually behaved as the electron acceptor due to low conduction band energy.[18] For example, the value of the electron mobility of semiconducting carbon nanotubes has been experimentally demonstrated to be on the order of 100,000 $cm^2/V{\cdot}s$, higher than any previously measured material and roughly 100 times that of bulk silicon.[22] The capability of carbon nanotubes to ballistically (no scattering of electrons) transport electrons is a foundation for their exploration in improving photovoltaic device performance, particularly by increasing electrical conductivity and lowering electrical heating.[31] Combining with a high surface area (1587 $m^2/g$ in individual separated SWCNT) and outstanding electronic properties, it is an ideal material for effectively dissociating excited hole-electron pairs and efficiently conducting the excited electrons toward electrode.[18, 32]

The electronic types also play a major factor in the effectiveness of carbon nanotubes in solar energy harvesting devices. Excited state lifetime obviously is much longer in semiconducting nanotubes comparing to metallic ones. Thus, semiconducting nanotubes are served as either direct light absorber, donating the photoexcited electron to the external circuit; or as an electron shuttle, accepting a photoexcited electron from another molecule and transporting it to electrode. With semiconducting tubes, the charge loss

during transportation is minimized attributed to less recombination. In contrast, metallic nanotubes tend to enhance charge recombination and lower the device performance in the light absorbing or electron transport layer, resulting from the continuous electronic pathway for relaxation of the photoexcited electron.[28]

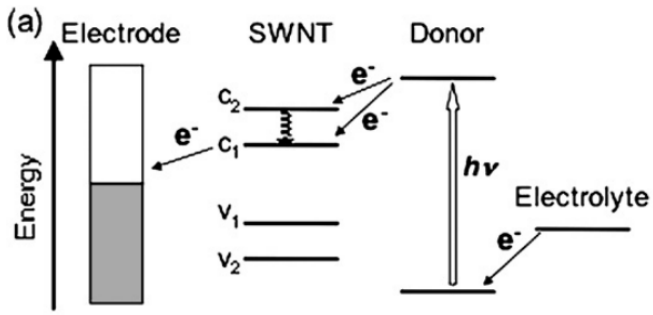


Figure 1.4. General Energy Diagram for Using SWCNTs as Acceptors (Umeyama, 2008).

Given their electronic types and excellency properties, SWCNTs are utilized in multiple ways. Majorly, SWCNTs serve as electron acceptor layers or electron transporting layers (Shown in Figure 1.4) and photoactive layers in solar cells. Some studies also explored nanotubes in the active layer of DSSCs and as electrode materials in photovoltaic cells, but it is not the focus in this thesis.

To utilize SWCNTs as electron acceptor layers or electron transport layers, there are basically two type methods to characterize SWCNTs surface chemistry covalent and non-covalent functionalization.[18, 33, 34] In both cases, research in light harvesting systems has been focusing SWCNTs as charge acceptors or transporter. The electron donors or

chromophores are attached to SWCNTs as much as possible to ensure the system performance. A possible route is using molecules to glue the charge donors and acceptors together. Covalent functionalization describes that the spacer molecules or chromophores are covalently attached to SWCNTs. [33] Non-covalent functionalization is realized through π- π bonding between SWCNT surfaces (acceptor) and target molecules (donor), which conserves the electron structures of the SWCNT and provides a relative steady bonding. [35]

In terms of covalent functionalization, chemical bonds have been investigated, including via carboxylic groups, hydroxyl group, pyridy isoxazolino, and sodium 4-styrenesulfonat. Herranz and his coworker established covalent bonding by carboxylic acid groups between SWCNTs and chromophores. [36] These groups are typically formed on SWCNT surface through acid treatment. Hydroxyl group containing porphyrin donors are connected to acceptors possibly through amide or ester bonds. They reported that the photo excited porphyrins quenched and these transduction rates and efficiencies are closely related to the length of the spacer molecules.[34] Torre and coworker used a similar method with aminophyhalocyanines as donors. [37] Another method includes pyridy isoxazolino groups along the carbon nanotube wall. [38] In this case, the electron transfer from excited state of donors to SWCNTs has not been observed. Instead, energy transfer mechanism was proposed.

To better preserve the pristine properties of SWCNTs, non-covalently chemistry is to graft SWCNTs with desired dye molecules. Since Zheng et al. demonstrated for the first

time the ability of DNA oligonucleotides to suspend carbon nanotubes in 2003,[39] there has been an explosion of research for utilizing the nanoscale self-assembly and recognition of biomolecules with nanotubes in devices.

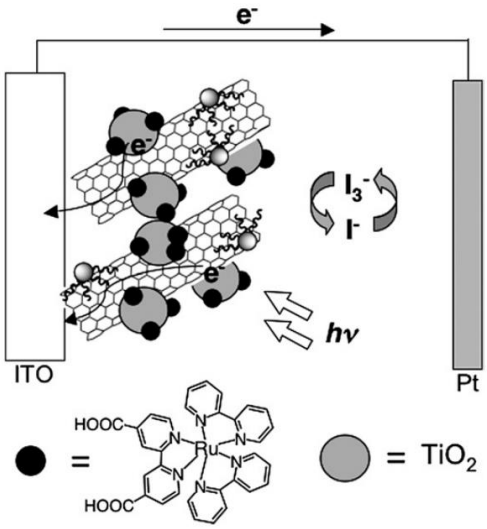


Figure 1.5. Schematic Illustration for SWCNT Serving in DSSC (Umeyama, 2008).

A recent effort by Choi et al. utilized biomolecules with SWCNT for a new class of dynamic solar energy harvesting cells, utilizing biomolecules for both structural support and assembly, as well as regeneration capabilities.[40] Guldi and his coworkers has demonstrated a high-performance device using carbon nanotubes as the charge acceptors non-covalently incorporated with the donors in a photoelectrochemical cell via pyrene derivative bearing an ammonium group.[41, 42] With zinc porphyrin supermolecules as electron donors, the incident photon to converted electron (IPCE) value was maximum at 4.2%, huge improving over the device without SWCNTs.[43] SWCNTs has also been non-covalently implemented into conventional DSSCs with a ruthenium based dye, platinum counter electrode and $I^-/I^{3-}$ redox couple, shown in Figure 1.5.[18, 44] That semiconducting

carbon nanotubes facilitate electron transport from $TiO_2$ to anodes provide a possible way to improve the performance of DSSCs. With further research building on this first effort, there is much potential for large increases in highly efficient flexible solar cells based on SWCNT acceptors.

### 1.2.2 Porphyrins

In the photosynthesis cores of bacteria and plants, light is absorbed by Chlorophyll, which is composed by several pigments. At photosystem II, the harnessed solar energy is converted efficiently to chemical energy. Inspired by this clean and efficient energy transfer in naturally occurring photosynthetic reaction centers, porphyrins have been designed and synthesized for light harvesting applications. Porphyrin chromophores have been explored in DSSC and light-harvesting donor-acceptor complexes.[35, 45-47] As effective photo-sensitizers, porphyrin molecules display several necessary characteristics including favorable redox potentials with respect to common electrolytes and strong photo-absorption by the electron-rich π-systems.[48] Furthermore, the optical properties of porphyrins can be readily tuned by both external anchoring ligand and metal ion at the core.[49-51]

In typical light-harvesting systems, it is possible to forming a chemical bond between the dye and the charge acceptors, both covalently or non-covalently. In terms of covalent functioning group, carboxylic acid is one popular binding group for porphyrins, while other functioning ligand such as 8-hydroxylquinoline (HQ) have been demonstrated.[52, 53]

A porphyrin has two major anchoring position – four *meso*-positions and eight *β*-positions, as shown in Figure 1.6. These parts may be functionalized with linkers containing anchoring groups such as carboxylic acids and HQ substitutes that attach to the surface of an acceptor. Thus, for non-covalent functionalization, the opposite electronic charge of porphyrin ligand and binding site can introduce static electric force which can anchor porphyrin chromophores. For example, positively charged pyridine group in *meso*-position of porphyrin can adsorb on negative charged DNA backbone via electrostatic attraction.[54]

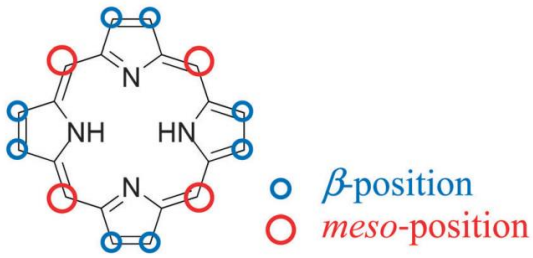


Figure 1.6. Possible Functionalization Spots on Porphyrin Ring Including Four *meso*- and Eight *β*- Positions (Li, 2012).

The intrinsic advantages of porphyrin-based dyes are their rigid molecular structures with large absorption coefficients in the visible region and their many reaction sites for functionalization; tuning the optical, physical, electrochemical and photovoltaic properties of porphyrins becomes feasible. In general, porphyrins show a Soret band at 400–450 nm and Q bands at 500–650 nm. To investigate the potential porphyrins for light harvesting, not only the functionalization group but also of different energy states of

a porphyrin were considered since the excite porphyrin need to have enough potential to donate electron to the acceptors.

In detail, the energy states are including ground, reduced, oxidized and excited states.[55] For a porphyrin molecule, S, the reduction potential of the molecule with a Fermi level in the energy scale is given as $E^0_{F,redox}(S^-/S)$, which describes electron transfer from an electron donor to an unoccupied level of S. Similarly, $E^0_{F,redox}(S/S^+)$, Fermi level of oxidation potential of S, indicates an electron transfer from the occupied state to acceptor molecule. The energy difference between reduction and oxidation potentials can be approximated as the difference of the lowest unoccupied (LUMO) and highest occupied (HOMO) states in the molecule. [48]

Once a porphyrin gets excited, it can be easily reduced or oxidized since there is an excitation energy ΔE* stored in the molecule. The stored excitation energy ΔE* corresponds to the energy transition between the ground and excited states, that is, ΔE* = ΔE(S/S*). The Fermi levels of excited molecules can be estimated by adding or subtracting ΔE* from the ground state redox potential of the molecule. Finally, the excited state oxidation ($E^*_{F,redox}(S^*/S^+)$) and reduction ($E^*_{F,redox}(S^-/S^*)$) potentials are described in Equations (1) and (2), respectively.[48, 56]

$$E^*_{F,redox}(S^*/S^+) = E^0_{F,redox}(S/S^+) + \Delta E\,(S/S^*) \quad (1)$$

$$E^{*}_{F,redox}(S^{-}/S^{*}) = E^{0}_{F,redox}(S^{-}/S) - \Delta E\,(S/S^{*}) \qquad (2)$$

For example, palladium *meso*-Tetra (N-methyl-4-pyridyl)porphine (PdT4) and ZnT4,[57] as shown in Figure 1.7, demonstrate their the energy transitions between each states, including ground and excited states as well as reduced and oxidized format.

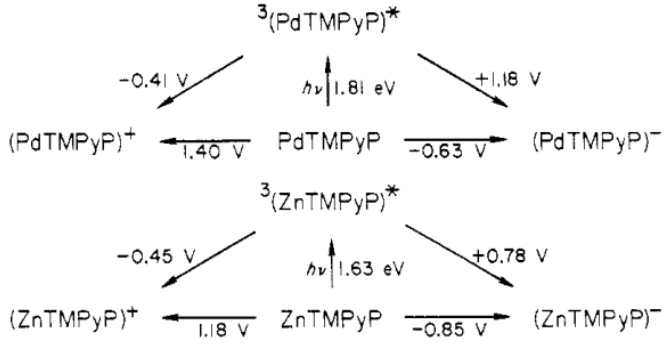


Figure 1.7. Latimer Diagrams of Palladium *meso*-Tetra (N-Methyl-4-Pyridyl)Porphine (PdT4) and ZnT4 Between Each States and Energy Potential Differences (Kalyanasundaram,1982).

Due to the tunability and cost-effectiveness, the porphyrins are one of the major components in light-harvesting research area. In this thesis, several porphyrins with different ligands and metal cores are utilized for understanding the photo-physical interaction mechanisms within a light-harvesting photoelectrochemical cell.

### 1.2.3 Molybdenum Disulfide ($MoS_2$)

Transition metal dichalcogenide (TMDC) is a class of the materials which have a layered structure of X-M-X planes, where X represents chalcogen atom and M is transition metal.

Each X-M-X layer holds to another layer via van der Waals interaction which is introduced by X-X. Such material family has garnered significant interest, because of the access to atomically thin layers and their unique layer-number-dependent physical properties.[58, 59]

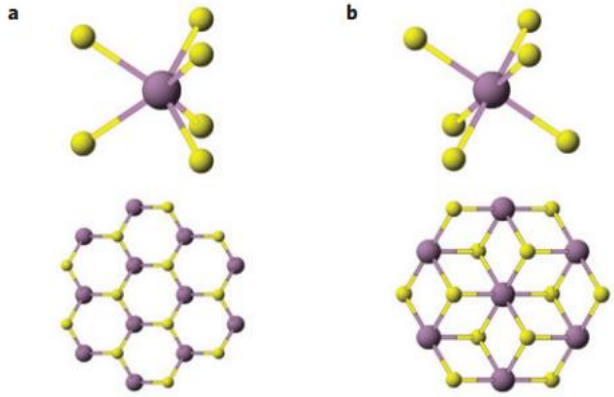


Figure 1.8. Schematic Crystal Structures of $MoS_2$ – (a) 2H or Trigonal Prismatic Coordination and (b) 1T or Octahedral Coordination (Kappera, 2014).

There are two polytypes of single layer molybdenum disulfide ($MoS_2$) has been mainly invested, namely, 1T and 2H, shown in Figure 1.8.[60, 61] 2H type with trigonal prismatic coordination is naturally abundant and widely used in industry as dry lubricant and catalysts due to the cost effectiveness. A recent discovery indicates the transition from in-direct bandgap at 1.3 eV to direct bandgap centered at around 1.88 eV. As a result from converting bulk semiconductor to atomic thin semiconductor, $MoS_2$ shows its photoluminescence (Figure 1.9).[58]

This advantage intrigued optical/electronic properties of two-dimensional (2D) TMD materials suitable for many applications due to their promising potential, such as

transistors, photodetectors, hydrogen evolution reaction (HER) and carbon dioxide reduction devices as well as solar cells,[62, 63] where the 2D semiconductor demonstrates high in-plane carrier mobility and on/off ratio.[64-66] These qualities should be useful in electronics applications.[58, 63, 67-69]

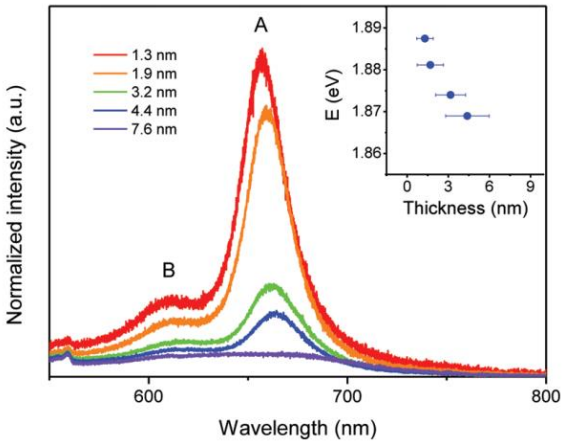


Figure 1.9. Photoluminescence Spectra of $MoS_2$ Films at Different Thicknesses (Eda, 2011).

$MoS_2$ has been applied in many studies due to chemical stability against photo-damage. The good stability against photo-damage[70] and the wide range of visible absorption render $MoS_2$ useful as photoelectrode materials.[71] Such a promising photoelectrode material has been demonstrated and operated in a photoelectrochemical cell.[70, 72-79] Due to the cost-effectiveness and excellent electronic properties, $MoS_2$ has been also explored as an additive agent in DSSCs.[74-76] In one study, the atomically-thin layer of $MoS_2$ coated on the counter electrode considerably enhanced the overall performance of DSSCs.[75]

Table 1.1. Different Methods to Achieve Thin TMDCs (Bhimanapati, 2015).

| Technique | | Mono- and few-layer materials available to date | | | | | Achievements | Challenges |
|---|---|---|---|---|---|---|---|---|
| | | *Single phase TMD* | *TMD alloy* | *Doped TMD* | *Vertical heterostructures* | *Lateral heterostructures* | | |
| *Top-down* | Mechanical exfoliation (and CVT) | 1T, 2H $MoX_2$<br>1T, 2H $WX_2$<br>BP,$SnX_2$, 1T, 2H (Nb,Ti,Zr,Nb,Ta)$X_2$ | $Mo_xW_{1-x}S_2$<br>$Mo_xW_{1-x}Se_2$ | Au-doped $MoS_2$,<br>Re-doped $MoS_2$,<br>Nb-doped $MoS_2$ | 2H ($MoS_2$-$WS_2$),<br>2H ($MoS_2$-$WSe_2$),<br>2H $MoS_2$-graphene,<br>2H $WS_2$-graphene,<br>2H $MoX_2$-hBN,2H $WX_2$-hBN,<br>2H $WSe_2$-1T $SnSe_2$,<br>2H $MoS_2$-BP | - | High crystallinity | Thickness control, yield, not scalable |
| | Liquid exfoliation | 1T,2H $MoX_2$<br>1T,2H $WX_2$,2H $TiS_2$,2H $TaS_2$,<br>(Nb,Ti,Zr,Nb,Ta)$X_2$ | - | - | - | - | High scalability | Small crystallites, thickness control, yield. |
| *Bottom- up* | Powder Vaporization | 1T, 2H $MoX_2$<br>1T, 2H $WX_2$ | $MoS_xSe_{2-x}$<br>$Mo_xW_{1-x}S_2$ | Mn-doped $MoS_2$<br>Co-doped $MoS_2$ | 1T $MoX_2$-2H $MoX_2$,<br>2H $MoX_2$-2H $WX_2$,2H $MoS_2$-BP,<br>2H $MoX_2$-GR, 2H $WX_2$-GR,<br>2H $MoS_2$-2H $WSe_2$-GR,<br>2H $WS_2$-hBN, 2H $MoS_2$-$SnS_2$,<br>2H $WS_2$-$SnS_2$, 2H $WSe_2$-$SnS_2$ | Graphene-hBN,<br>1T $MoS_2$-2H $MoS_2$,<br>2H $MoS_2$-$WS_2$<br>2H $MoX_2$-2H $MoX_2$<br>2H $WX_2$-2H $WX_2$ | High scalability | Defect control, uniformity, stoichiometry control |
| | MOCVD | 1T $MoX_2$,<br>$WX_2$ | - | - | $MoS_2$-$WSe_2$-graphene | - | High scalability | Defect control |
| | MBE | 2H $MoSe_2$<br>2H $WSe_2$<br>1T $PtSe_2$ | - | - | $MoSe_2$-graphene | - | High scalability | Defect control, domain size |

X- S,Se, BP- Black phosphorous, GR- graphene

To take full advantage of the $MoS_2$ properties in solar energy harvesting applications, there are several challenges. One of them is accessing the large-area atomic layers. As described in Table 1.1, there are two distinct approaches to obtain atomically-thin TMDCs: “top-down” including mechanical cleavage and liquid exfoliation, and “bottom-up” such as chemical vaper deposition (CVD).[80] In recent advances in liquid exfoliation of $MoS_2$, Chhowalla and co-workers achieved mono-layers through Li ion intercalation and forced hydration.[81]. Thus, large-area ultrathin films of $MoS_2$ nanolayers became available via liquid process and membrane filtration deposition. The exfoliated $MoS_2$ layers in water were deposited on a filter membrane which were subsequently transferred to conductive transparent glass, such as indium tin oxide (ITO), serving as electrodes. [72, 82] This approach is cost-effective and shows great potential of creating large-area 2D materials.[80, 83, 84]

It is critical to investigate the issues in large-area fabrication by liquid exfoliation, such as the small crystallites and crystal defects. For $MoS_2$ as an example, it is reported that the photoexcited carriers are captured by defects in $MoS_2$ via Auger scattering process, based on the observation that carrier density and temperature affected recombination dynamics.[62, 85] Defects of monolayer $MoS_2$ come from sulfur and molybdenum vacancies and interstitials as well as grain boundaries and impurity atoms.[86] Both edge sites and defects can facilitate charge recombination and reduce charge transport to electrode.[72, 87, 88]

In order to address the issues such as the defects embedded in crystallites, the surface treatments of $MoS_2$ may be investigated. Several recent reports demonstrated that surface functionalization could significantly modulate the physical and chemical properties of $MoS_2$, which may then be exploited in optoelectronic, electrochemical, and catalytic applications.[84, 89, 90] For example, researchers showed that p doping such as oxygen plasma irradiation and chemical dopants could suppress the nonradiative recombination and enhance the photoluminescence quantum efficiency such phenomena may be explained as depletion of trion and formation of exciton.[88, 89, 91] Thus, surface engineering of $MoS_2$ is a potential research direction to improve charge separation and promote charge transfer in $MoS_2$ applications.

## 1.3 Organization

As discussed above, SWCNTs, porphyrins and $MoS_2$ are potential materials, which have their distinct advantages to serve in photoelectrochemical cells. Many researchers have explored each individual material for light harvesting applications, but there are still many challenges regarding these materials, such as interactions between SWCNT and porphyrins, photo-degradation of porphyrins during light harvesting and charge recombination in $MoS_2$. This thesis addressed these important issues in individual chapters.

In Chapter 2, materials and method section, the material information is listed, including the resource of all materials, the processing and storage methods. The liquid phase processing procedure is described. In detail, to achieve non-covalently functionalized individual carbon nanotubes, we used a two-stage surfactant replacement method. To obtain 2D $MoS_2$ flakes, we follow the method based on lithium intercalation along with aqueous exfoliation. Processed carbon nanotubes and $MoS_2$ are deposited via vacuum membrane filtration. All general instruments utilized in this work and characterization methods are described in Chapter 2. The specific materials and instruments used in individual studies are described in each chapter.

Chapter 3 describes a light-harvesting platform based on the DNA-template SWCNT – porphyrin. With this platform, photo-processes in the donor/ acceptor SWCNT nanohybrids are preliminarily studied. To understand the details of the charge separations and transporting processes, it is important to comprehend the mechanism of the

porphyrins and porphyrin-DNA complex. The porphyrin species have various features such as excited states lifetime, band gap and redox potentials. All these properties are strongly relative to photo-conversion processes in the nanohybrids as well as overall system performance. We investigated five metalloporphyrin species with various excited state lifetime to understand their photophysical processing and interaction with DNA-SWCNT.

In Chapter 4, we demonstrate that photo-bleached porphyrins can be replaced with fresh porphyrins to maintain the photocurrent output in a light-harvesting cell. It is achieved via dissociation porphyrins from DNA-coated carbon nanotubes. The photocurrents can fully recover after fresh porphyrin molecules are reintroduced to the system. By continuously replacing the porphyrin, the photocurrent output of the light-harvesting cell can be maintained and highly improved comparing the system without porphyrin recovery.

$MoS_2$ based optical and photoelectrochemical studies are described in Chapter 5. With the light-harvesting platform introduced in Chapter 3, we utilize porphyrins as interfacial molecules for large-area $MoS_2$ nanolayers to facilitate their light-harvesting performance. With surface treatment, porphyrins physically absorb on $MoS_2$ film. Recombination due to small crystalline and defects of $MoS_2$ are lessoned. A higher efficient charge injection and photocurrent output is achieved.

# CHAPTER 2. MATERIALS AND METHODS

## 2.1 Materials Preparation

*SWCNT*: The SWCNTs used in this thesis are CoMoCAT and electronic type separated carbon nanotubes, which were obtain from Sigma Aldrich and NanoIntegris, respectively. The CoMoCAT SWCNTs are produced by CVD using metal catalysts. This standard procedure can produce scalable large quantity. The average diameter is about 1 nm with length of ~1 μm. Electronic type sorted SWCNTs are synthesized by an arc-discharge method. The reported mean diameter is 1.4 nm with a distribution range of 1.2- 1.7 nm, and the length ranges from 100 nm to 4 μm.

*DNA*: All DNA sequences used in Chapter 3 and 4 were purchased from Integrated DNA Technologies. The detailed sequences are described in materials and methods section in corresponding chapters. DNA were solubilized in ultra-pure water (18.2 MΩ) for storage (-20°C) without further purification.

*Chromophores*: The $H_2T4$ (Figure 2.1a) was obtained from Frontier Scientific as powder and stored at -20 °C. Metalloporphyrins (MTMPyP4) where M= Zn(II), Pt(II), Pd(II) and Cu(II) were synthesized by Professor McMillin's group in Purdue Chemistry (Figure 2.1b) [92, 93]. The anions of T4 were tosylate group ($Tos^-$) or nitrate ion ($NO_3^-$). Since the

T4 are stable in water solution, all T4 porphyrin samples were dissolved in ultra-pure water and stored for months in dark environment at room temperature. All protoporphyrins (Chapter 4 and 5) were purchased as powder from Frontier Scientific. Due to the environmental sensitivities of protoporphyrins, amber vials and centrifuge tubes were used for storage. Protoporphyrins were dissolved in dimethyl sulfoxide (DMSO) and stored at -20 °C for months. The exposure of protoporphyrins in room light can introduce fast degradation, leading a visible color or absorption spectra changes. All other porphyrins and dyes were only used in single experiment and which are described in corresponding chapters.

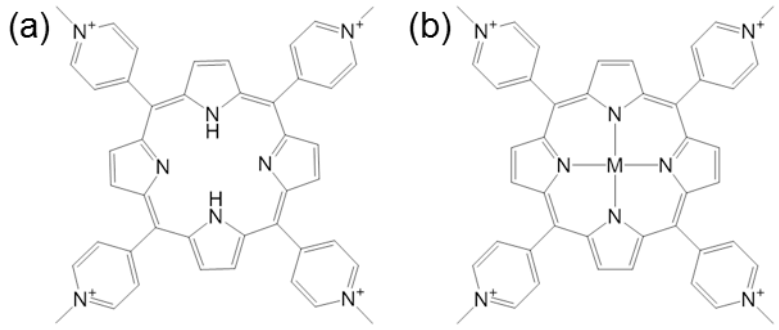


Figure 2.1. The Molecular Structures of $H_2T4$ (a) and Metal-Centered MT4 (b), Where M= $Zn^{II}$, $Pt^{II}$, $Pd^{II}$, or $Cu^{II}$.

*Membranes*: Several different membranes with various pore sizes were applied in multiple experiments. The detailed information is narrated in methods section in each chapter. Here is a brief summary. Aluminum oxide and polycarbonate isopore membrane filters with 25 mm diameter and 0.2 μm were obtained from Fisher Scientific. The aluminum oxide membranes (used in Chapter 3) can be dissolved high concentration

NaOH solution, while polycarbonate ones are solubilized in non-polarized solution, such as chloroform. Laminated polytetrafluoroethylene (PTFE) films, where PTFE laminate onto polypropylene non-woven layer, with 25mm diameter and 0.2 μm pore diameter were purchased from VWR International. The PTFE has high chemical compatibility and is hard to be dissolved in commonly used organic solvent. Thus, PTFE membranes have its own advantages in organic solvent involved solution filtration process compared to polycarbonate membrane. PTFE membranes were used in Chapter 3, while polycarbonate membranes were applied in Chapter 4 and 5.

*Other Chemicals and Materials*: Tribasic sodium phosphate was obtained from Mallinckrodt Chemical Works. Isopropyl alcohol (IPA) was supplied from Avantor Performance Materials. ITO coated glass squares with a surface resistivity of 70 to 100 ohm and other reagents including sodium chloride, sodium azide, sodium iodide, iodine, monosodium /disodium phosphate, L-ascorbic acid (Asc), sodium cholate, Tris base, ethylenediaminetetraacetic acid (EDTA) were purchased from Sigma-Aldrich. Membrane tubing for dialysis (12-14 kD and 100 kD) were purchased from Fisher Scientific. $MoS_2$ crystals were purchase from Alfa Aesar with form of ~325 mesh powder. The butyllithium was obtained from Sigma-Aldrich as 1.6 M solution in hexane, which is moisture and oxygen sensitive. All the preparations and intercalation process were carried out in a nitrogen-protected environment.

## 2.2 Solution Processing and Fabrication

### 2.2.1 Surfactant Assisted Exfoliation

The CoMoCAT tubes were ultrasonicated in aqueous solution with 1 wt.% sodium cholate under 20 W for 1 hour using a Cole Parmer sonicator with a 3 mm stepped micro tip. To prevent in-efficient sonication, the solution was placed in ice-water mixture bath. The resulting solution was pure black. Then, the solution was centrifuged using a Beckman Coulter L-100XP ultracentrifuge at 175,000 g or 32000 rpm for 2 hours. The supernatant was collected and stored in room temperature for months. Before each experiment, the surfactant was replaced by DNA. the SWCNTs solution was dialyzed with DNA in a 12-14 kD membrane tubing against aqueous solution in Figure 2.2. The dynamic diffusion process took up to 6 hours. Choosing 12 -14 kD pore size dialysis membranes was chosen, because the sodium cholate molecules pass through the pore easily but not the 24 base DNA oligonucleotide. The dialysis was performed in standard Tris-HCl buffer at the solution pH 7.4. The buffer solution was replaced every 4 to 6 hours for 6 times, resulting in surfactant free DNA-SWCNT solution. The $2^{nd}$ stage dialysis with 100 kD membrane tubing was performed for 24 hours to remove free excess DNA molecules from the SWCNT-DNA solution.

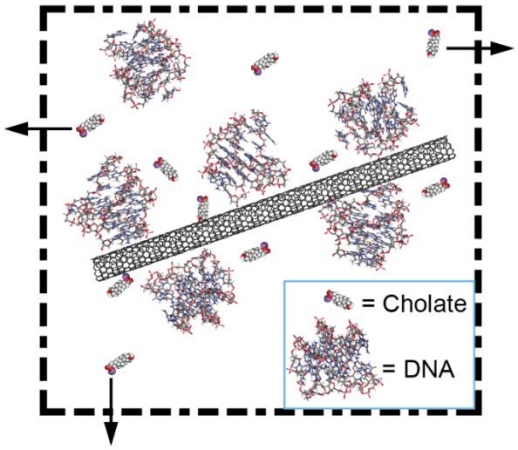


Figure 2.2. Schematic of DNA Adsorption Process onto Carbon Nanotubes via Membrane Dialysis.

Electronic type sorted carbon nanotubes were obtained via density gradient ultra-centrifugation (DGU) purification method.[94] Following the same procedure as the CoMoCAT nanotube preparation method, these tubes were dispersed in aqueous solution with 1 wt.% sodium cholate through tip sonication for 1 hour at 20 W and centrifugation at 15,000 g or 30000 rpm. The SC-dispersed SWCNT solution was subject to surfactant replacement via two-stage dialysis.

### 2.2.2 Lithium Introduced Exfoliation

Approximately 3 g of $MoS_2$ crystals were placed into a three-neck flask before nitrogen purging. 3 mL of 1.6 M butyllithium solution in hexane was added into the flask using a hexane pre-wetted syringe (Figure 2.3). Lithium ion diffusing into $MoS_2$ layers and intercalation was achieved after 48 hours, shown in Figure 2.4. With positive nitrogen

pressure, a glass frit with a second three-neck flask was connected to the previous flask. The glass frit has medium porosity (10-15 μm) which can filter all $Li_xMoS_2$. As shown in Figure 2.5, after flipping the whole setup, the mixture remained on the frit. Once the positive nitrogen pressure was applied at first flask while the second flask is under vacuum, all liquids passed through the frit and $Li_xMoS_2$ was left on it.

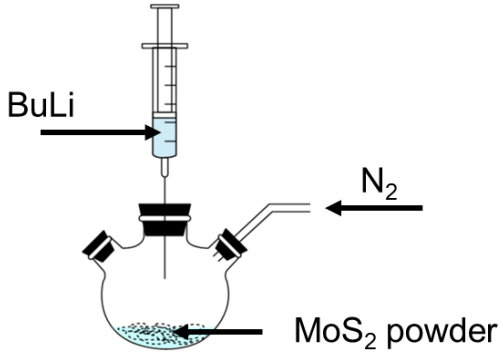


Figure 2.3. Adding Butyllithium into $MoS_2$ in Hexane under Nitrogen.

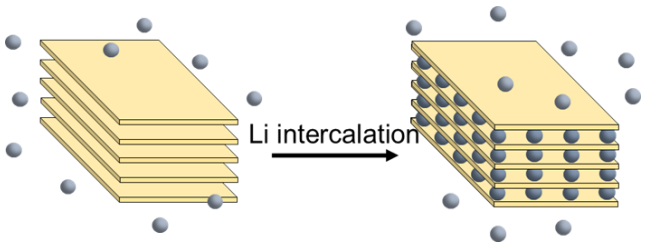


Figure 2.4. Lithium Ion Diffusion into $MoS_2$ Layers and Intercalation.

To remove excess butyllithium, the $Li_xMoS_2$ was washed by 60 mL dry hexane. Exfoliation was achieved by immersing the $Li_xMoS_2$ in water and applying tip-sonication at 5 W for 1 hour, resulting in a dark black mixture. $Li_xMoS_2$ was exfoliated into monolayers by forced hydration which was generated from Li interaction with $H_2O$ molecules. The mixture was centrifuged at 5000 rpm for 20 min to remove un-exfoliated

material. A stable colloidal green-black suspension was obtained. The solution with nitrogen purging can be stored in a refrigerator for months.

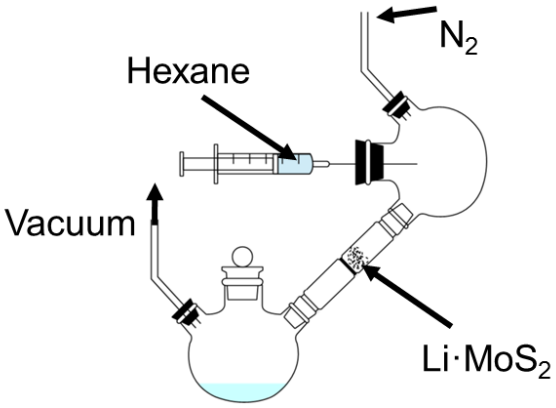


Figure 2.5. Filtering $Li_xMoS_2$ and Washing out Excess Butyllithium Solution with Hexane.

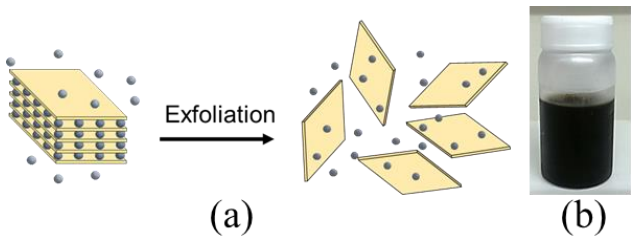


Figure 2.6. (a) Water Involved Exfoliation by Forced Hydration. (b) Retrieved $MoS_2$ Supernatant for Measurement.

### 2.2.3 Filtration-Based Film Fabrication

*SWCNT*: Here we are taking PTFE membrane for example. In each chapter, there are detailed membrane information introduced. The 25 mm diameter PTFE films (0.2 μm) were used to make the nanohybrid films through a vacuum filtration process, shown in Figure 2.7a. The DNA-SWCNT solution was diluted in water to promote evenly

distributed films. At the starting point, the PTFE films were wetted by passing through 5 mL IPA because of their initial water resistant properties. Then, the DNA-SWCNT films were deposited by passing the DNA-SWCNT solutions through the filter. After the deposition of DNA-SWCNT films, 5 mL water were passed through the films to remove unbounded and weakly bounded DNA sequences. To functionalize the DNA-SWCNT films, 200 nmol porphyrin solutions (approximately 1:1 porphyrin to DNA sequences after dialysis) were slowed filtered through the deposed films. After porphyrin functionalization, 5 mL water was applied to wash free or weakly bounded porphyrins. Then, the PTFE films with nanohybrids were pressed on to ITO glass slides which were wetted by IPA for 1 hour to obtain a better nanohybrids adsorption. The PTFE films were continuously pushed against ITO slides by clamps and placed on a hot plate at 60 °C for 6 hours to evaporate the liquids such as water and IPA. Lastly, the PTFE films were gently peeled off, leaving the nanohybrids on the ITO slides, shown in Figure 2.8.

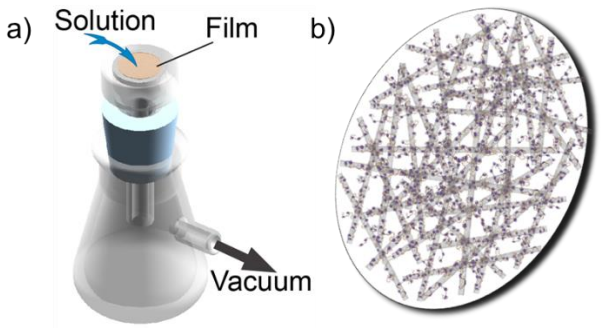


Figure 2.7. (a) The Film Deposition via Vacuum Filtration. (b) The Schematic of Deposited Nanohybrids Film.

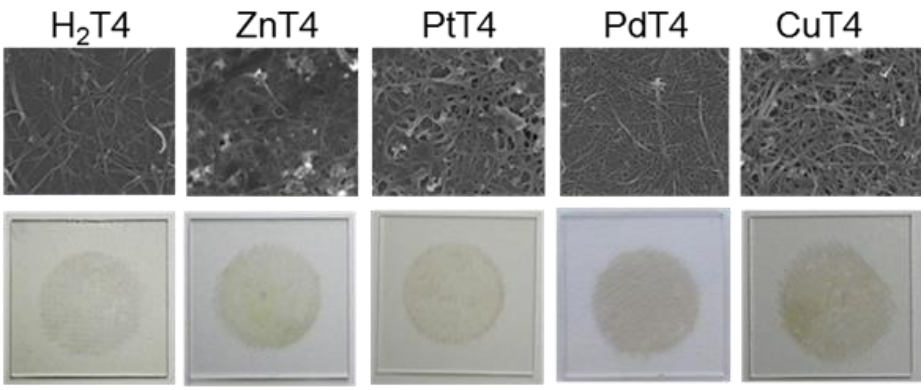


Figure 2.8. Scanning Electron Microscope (SEM) Images (Top Row) and Optical Photographs (Bottom Row) of the Deposited Porphyrin-DNA-SWCNT Nanohybrids Films.

*$MoS_2$*: To deposit $MoS_2$ suspended solution for thin film fabrication, we employed the water-aspirator-driven membrane filtration setup, which was similar to the SWCNT processing methods. The membrane was a 50 nm-pore size polycarbonate membrane. Chemically exfoliated $MoS_2$ solution was initially diluted in DI water, which can help achieve the uniform dispersion of $MoS_2$ flakes. The solution passed through the membrane pores and $MoS_2$ flakes stayed on the polycarbonate membrane surface. It is a self-regulating process. As one or more flakes covered a pore, the flow rate through the pore would drastically decrease. At other uncovered pores, however, the flow rate increases, resulting a uniformly deposited film of $MoS_2$ flakes. The film thichness may be controlled by adjusting the amount the $MoS_2$ flakes in the solution. After the deposition, we transferred the film onto any substrates (e.g. ITO or silicon wafer) by facing the $MoS_2$ film membrane against the substrate. The potential air bubbles were driven away by mild water rinsing. After evaporation of all water at room temperature, the contact between the film and the substrate was steady and uniform. Lastly, the $MoS_2$ film on substrate was

obtained by dissolving the polycarbonate membrane using chloroform. $MoS_2$ stayed on the substrate surface via van der Waals interactions, as shown in Figure 2.9. The resulting the $MoS_2$ film could be as thin as ~1 nm or mono/bi-layer, depending on the quality of $MoS_2$ flakes from the chemical exfoliation.

Figure 2.9. Deposited, Transparent $MoS_2$ Film on ITO Coated Glass Substrate.

## 2.3 Characterization

*Ultraviolet-visible spectroscopy*: A Perkin Elmer Lambda 905 UV/visible/near-IR spectrophotometer was used to record the absorption spectra for porphyrin solutions and solid phase films. The detector has an integration time of 0.2 s with a default slit-width of 2 nm. For titration experiments in Chapter 3, the absorption of DNA-SWCNT titrations were measured through a 10 mm × 2 mm quartz cuvette due to the limited amount of DNA-SWCNT solution sample. This cuvette held much less volume (approximately 200 µL), while producing clear signals. In contrast, DNA titrations with T4 were performed with a 10 mm × 10 mm quartz cuvette.

It is worth mentioning that the surface treatment was performed for the cuvettes used in solution measurements. Porphyrins, especially cationic porphyrins, could adsorb on cuvette surface due to ion paring since the cuvette carries the negative charge. While monolayer of adsorbed porphyrin molecules might not affect the solution concentration significantly, inaccurate absorption spectra would be measured due to the surface adsorption, if the initial concentration of the added porphyrins is low. Thus, for cationic porphyrins, silanization of cuvette surface was necessary to overcome this issue. We used ~5% dimethyldichlorosilane in heptane (Sigma Aldrich) for surface treatment. After overnight soaped in the silanization solution, the cuvette surface became strongly hydrophobic and minimized the cationic porphyrin adsorbing.

For solid phase films, we used a sample holder with a clamp. Therefore, the position of sample films might vary during each measurement. The uniformity of each sample plays an important role on the consistency of absorption spectra between measurements.

*Photoluminescence*: Photoluminescence experiments were carried out using a Horiba Jobin Yvon Fluorolog 3 fluorometer. A 450 W Xenon lamp with a Czerny-Turner-type double monochromator was used for photo-excitation. The emission signals were recorded with a photomultiplier tube and an indium gallium arsenide (InGaAs) detector for UV/visible and near-infrared spectra, respectively. Each detector was connected a Czerny-Turner-type single monochromator for dispersion of emitted light. In this thesis, the photomultiplier tube was used for porphyrin emission measurements since it could detect up to ~900 nm wavelength. The excitation wavelengths for each porphyrin

solution were at their Soret band maxima. The emission spectra were corrected by absorption strengths at given excitation wavelengths, as shown in Equation (3).

$$E_{corrected} = \frac{E}{1 - 10^{-A}} \quad (3)$$

where E represents the measured emission intensity and A is the absorbance.
With the liquid nitrogen cooled InGaAs detector, we recorded the emission in near-infrared range up to ~1600 nm. For example, the emission spectra of singlet oxygen centered at ~1280 nm were obtained with this detector. It should be noted, however, that our measurements were performed from 950 to 1400 nm because water absorption dominated beyond the wavelengths. The detailed photoluminescence measurement conditions are discussed in individual chapters.

Raman microscopy: The Raman signatures were acquired by a Renishaw confocal Raman microscope under a 633 nm (1.96 eV) laser excitation. Switching from microscope image to laser measurement, the laser spot need to be calibrated. To obtain Raman signatures (and photoluminescence) from solution samples by Raman microscope, a low power (5×) objective was recommended, since the focal distance is large enough so that the solution sample would not contaminate the objective lens. For solid samples, such as DNA-SWCNT nanohybrid films and $MoS_2$ nanolayers, a high power (100×) objective was used.

Photoelectrochemistry: The electrochemical measurements were carried out with a Princeton 263A galvanostat. For electrochemical cell, we used an ITO/glass slide coated with SWCNT-based nanohybrids or $MoS_2$ flakes as working electrode and a platinum-coated glass as a counter electrode. The reference electrode was short-circuiting by connected it with the counter electrode. Detailed electrolyte conditions are described in the material and method section of each Chapter. The light source of photoelectrochemical measurements in Chapter 3 was a 450 W Xenon lamp with a double monochromator equipped in the Florolog-3 fluorometer. An optical fiber was used to guide the light from the fluorometer to the electrochemical cell. In Chapter 4 and 5, a 150 W Xenon lamp was employed for illumination. In Chapter 4, the excitation light was passing through a Thorlabs FGS900S bandpass (315 – 710nm) filter, while in Chapter 5, a long-pass filter (>400 nm, Thorlabs Inc.) and a short-pass filter (<710 nm, Thorlabs Inc.) were used for visible illumination correction.

# CHAPTER 3. PHOTOCONVERSION IN SWCNT-DNA-PORPHYRIN HYBRIDS

## 3.1 Introduction

The extraordinary properties of carbon nanotubes and relevant surface chemistry are described in Chapter 1. The SWCNTs, conjugating with DNA-porphyrins, are examined for light harvesting and energy conversion. This chapter presents an investigation the interaction between $H_2T4$ and SWCNTs with and without the interfacial DNA molecules from optical and photoelectrochemical measurements. The SWCNT-DNA-porphyrins nanohybrids are explored with various cations metalloporphyrin species for photoelectrochemical performance.

Four cationic metalloporphyrins, including ZnT4, PtT4, PdT4, and CuT4 along with $H_2T4$ are explored as photoactive donor molecules. Each of these chromophores shows distinct emission features. For example, $H_2T4$ and ZnT4 exhibit primarily singlet-state transitions, whereas PtT4 and CuT4 demonstrate efficient intersystem crossing, displaying phosphorescence from triplet states.[57, 95, 96] Interestingly, PdT4 shows both fluorescence and phosphorescence signatures in its spectrum.[49, 57, 92]

From steady-state fluorescence measurements, we find that these porphyrins undergo strong charge transfer interactions with semiconducting nanotubes, which is consistent

with our observation of emission quenching of singlet oxygen generated by porphyrins. The excited state lifetime measurements indicate that photo-excited electrons are transferred to carbon nanotubes from their singlet states rather than their triplet states. The porphyrin-SWCNT-based donor-acceptor complexes generate stable anodic photocurrents in a photoelectrochemical cell with an efficiency of approximately 1.5% at the excitation wavelengths except CuT4, which has a unique relaxation mechanism.

## 3.2 Materials and Methods

In this study, twenty-four base-long human telomere sequence (5'-$(AGGGTT)_4$-3') strands are used to functionalize SWCNTs non-covalently. The functionalization procedures are described in Chapter 2. Here, the molar ratio of DNA to SWCNT is estimated to be roughly 100 strands or 2,400 nucleobases per 1-μm of nanotube.[97-99] As a control experiment, we incorporated another noncovalent anionic pyrene derivative, pyrenebutyric acid (PBA), to functionalize SWCNT for porphyrin adsorption.

As discussed in Chapter 2, photoelectrochemical measurements were carried out using the galvanostat. The light source was a 450 W Xenon lamp with a Czerny-Turner type double monochromator and having a bandpass of ca. 15 nm. The output powers at different wavelengths were measured by a Newport 1918-C power meter. The illumination area was ca. 0.866 $cm^2$.

For steady-state photoluminescence measurement, the excitation wavelengths for $H_2T4$, ZnT4, PtT4, and PdT4 emission were 421, 437, 401 and 417 nm, respectively. The emission spectra of $H_2T4$, ZnT4, and PdT4 were obtained using 5-nm slit widths for both excitation and emission, while 8-nm slit widths were used to record PtT4 emission. All emission spectra are corrected for the absorption strengths at the respective excitation wavelengths.

The phosphorescence lifetime measurement of PtT4 and PdT4 were performed by a detection system that includes Hamamatsu R928 phototube, a PACIFIC Instruments, and a Tectronix TDS 520 digital oscilloscope. Photo-excitation for this system is a VSL-337-NDS nitrogen dye laser incorporated with a dye component α-NPO in toluene which was tuned at the wavelength to ca. 408 ± 15 nm range. Fluorescence lifetime measurements were carried out by an Optical Building Blocks Corporation EasyLife X lifetime fluorometer with an excitation LED at 409 nm.

Raman spectra were taken with the Renishaw confocal Raman microscope coupled a 633 nm diode laser. SEM images (shown in Figure 2.8) were recorded using an FEI NOVE nanoSEM FESEM high-resolution system. The band deconvolution of the radial breathing mode (RBM) peaks of SWCNT used a Lorentz function.

The electrochemical measurements, which is described in Chapter 2 in detail, are were carried out with a two electrode setup, where a deposited ITO slides as working electrode and a platinum coated glass as counter electrode. Here, we examined the short-circuit

photocurrent, meaning zero bias voltage was applied and reference electrode was connected to the counter electrode. The electrolytes used in this chapter included: (i) air-saturated or $N_2$-purged, 100 mM NaI, 1 mM $I_2$ and 6 mM Asc at pH 5.5, (ii) 1 mM Asc in phosphate buffer at pH 7.5 and (iii) 5mM Asc in 10mM phosphate buffer at pH 7.0.

## 3.3 Results and Discussion

### 3.3.1 Optical Characterization of SWCNT-DNA-Porphyrin Hybrids

The optical signatures of SWCNT-DNA-Porphryin hybrids were examined using a spectraphotometer and a confocal Raman microscope. We observed strong optical transductions immediately after porphyrin functionalization with SWCNT-DNA. Figure 3.1a shows the optical absorption signatures of free $H_2T4$ in water and SWCNT-DNA in buffer solution along with the deposited SWCNT-porphyrin films with and without DNA. Free solution $H_2T4$ shows the strong Soret band at ~421 nm and four Q-band peaks ranging from 520 to 650 nm.[100] The Soret band is much prominent in the SWCNT-DNA-$H_2T4$ film than in the SWCNT-$H_2T4$ film sample, indicating the role of DNA for assembling SWCNTs and $H_2T4$. SWCNT-DNA solution shows distinct absorption bands in the near-IR and visible region, indicative of excitionic transitions between the 1st and 2nd van Hove singularities, namely, $E_{11}$ and $E_{22}$.

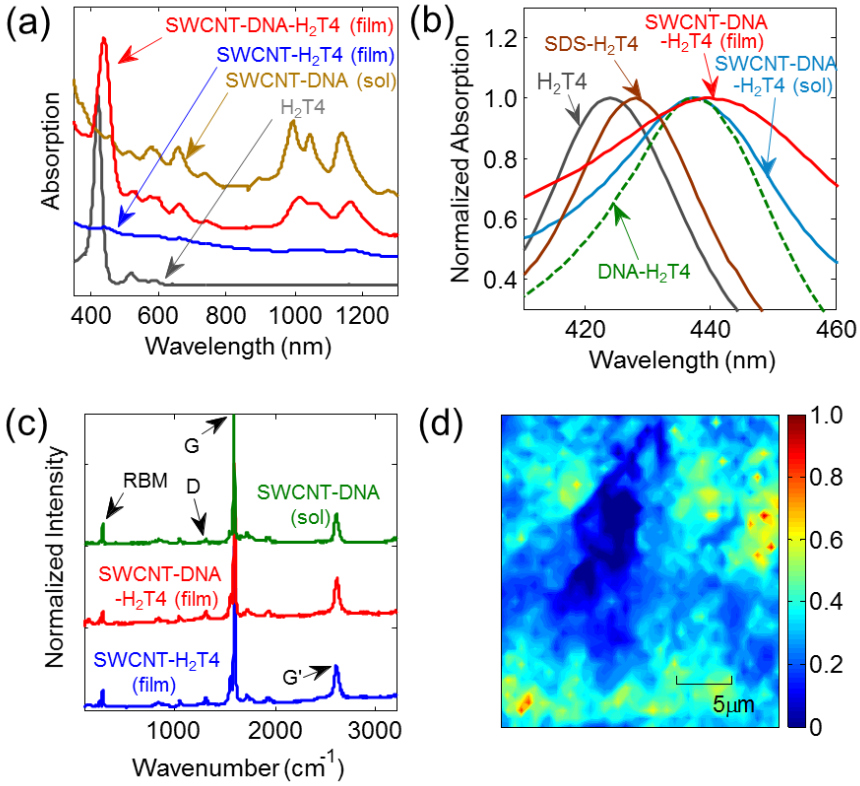


Figure 3.1. (a) SWCNT-DNA Solution and $H_2T4$ Solution Absorption Spectra along with Absorption Spectra of Deposited SWCNT-DNA-$H_2T4$ and SWCNT-$H_2T4$. (b) Soret Band Absorption of $H_2T4$ in Free Solution and with Surfactant (SDS) and DNA as Well as Deposited SWCNT-DNA-$H_2T4$. (c) Raman Spectra of SWCNT-DNA (Solution), SWCNT-DNA-$H_2T4$ (Film), and SWCNT-$H_2T4$ (Film). (d) 2D Contour Plot of Deposited SWCNT-DNA-$H_2T4$ Film Based on The G Peak of Carbon Nanotubes.

In Figure 3.1b, the Soret band of $H_2T4$ exhibits a significant spectral redshift (c.a. 21 nm) in the presence of DNA and DNA-SWCNT both in solution and solid phase.[101] When cationic $H_2T4$ porphyrins interact with anionic surfactant SDS, however, simple electrostatic interaction between them leads to a relatively smaller redshift, i.e. ~7 nm. These results suggest strong affinity between DNA-SWCNTs and porphyrins both in solution and on films. The 24-mer human telomere sequence has a dissociation equilibrium constant ($K_d$) of ~ 200 nM toward $H_2T4$ porphyrins.[102] This strong

interaction is attributed to the G-quadruplex structure of the oligonucleotides stabilized by $K^+$ and $Na^+$.[103] This interaction modulates the porphyrin properties which can be observed by probing porphyrin absorption signatures.

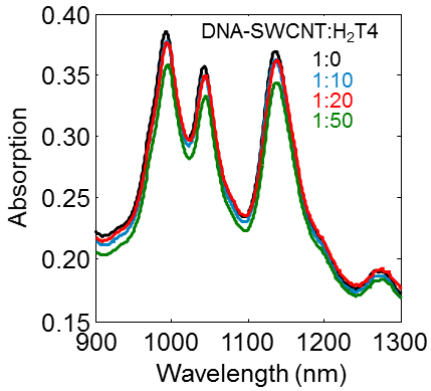


Figure 3.2. Absorption Spectra of SWCNT-DNA in Solution upon Serial Addition of $H_2T4$ Porphyrin Solution.

Addition of DNA strands does not significantly change the $E_{11}$ bands of carbon nanotubes, indicating that the pristine SWCNT surface is well preserved (Figure 3.2). Raman signatures in Figure 3.1c provides additional evidence of preservation of pristine carbon nanotubes with noncovalent DNA interaction in both solution and solid-state films. The disorder (D) bands of carbon nanotube at ~1320 $cm^{-1}$ is indicative of structural defects, such as grain boundaries and vacancies, often introduced by covalent reactions (e.g. carboxyl group at the surface). Here, the intensity of D peak in solid films is barely changed compared with DNA-SWCNT solution, suggesting sp2 carbon systems are preserved. Figure 3.1d, plotted based on the G-band of $H_2T4$-DNA-SWCNT film, demonstrates a percolation network of randomly deposited tubes. The RBM signatures are shown in Figure 3.3b, showing the presence of common CoMoCAT species.

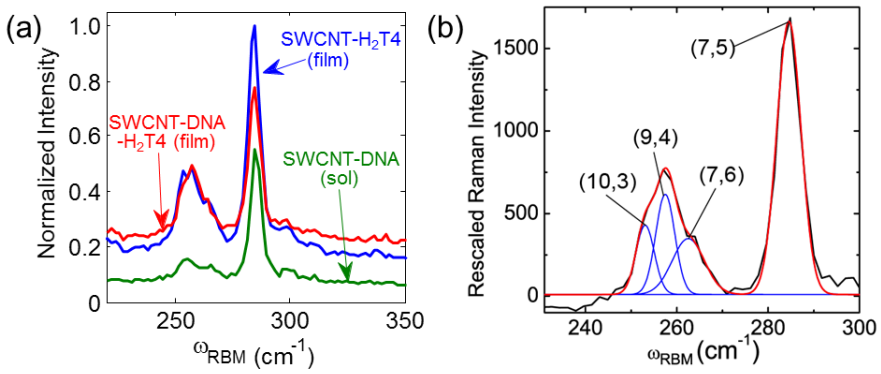


Figure 3.3. (a) RBM Signatures of CoMoCAT SWCNT-DNA-$H_2$T4 (Solution and Film) and Deposited SWCNT-$H_2$T4 Film. (b) Deconvolution of RBM Raman Spectra of SWCNT-DNA-$H_2$T4 Nanohybrids Film.

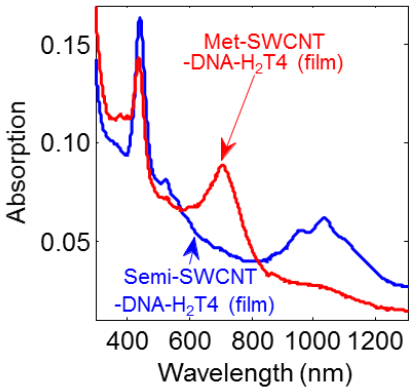


Figure 3.4. Absorption Spectra of the Deposited Film Samples Made of Metallic (Met, in Red) and Semiconducting (Semi, in Blue) Nanotubes.

Similar to the CoMoCAT SWCNT-DNA-porphyrin films, the absorption spectra of eletronic type sorted SWCNT-DNA interacting with porphyrins are presented in Figure 3.4, which semiconducting and metallic SWCNT-DNA-$H_2$T4 assemblies deposited on the ITO-coated glass. These samples typically include ~4 μg SWCNTs that are also responsible for the broad background in the UV and visible range. In addition to the Soret bands near 440 nm, strong absorption maximum in the red spectrum is due to the optical

transitions of metallic species between the first van Hove singularities (i.e., $E_{11}^{M}$). In comparison, the blue spectrum shows the broad absorption signatures from 900 to 1200 nm which are assigned to the optical transitions of semiconducting species in the 2nd van Hove singularities (i.e., $E_{22}^{S}$). The Raman signatures of deposited semiconducting SWCNT-DNA-porphyrin hybrids are shown in Figure 3.5a. Deconvolution of the RBM mode suggests that the nanotube diameters are in the range of 1.35 to 1.65 nm. Here, the tube diameter ($d_t$) is derived from the RBM frequency, $\omega_{RBM}$, using $d_t = 248/\omega_{RBM}$.[104]

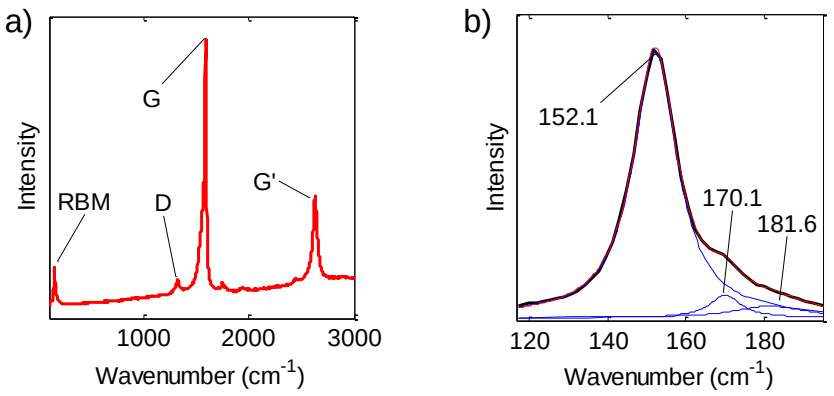


Figure 3.5. (a) Raman Spectra of the Deposited Film Samples (SWCNT-DNA-$H_2$T4). (b) The Zoom in and Deconvolution of RBM Peaks from (a).

### 3.3.2 Effects of Porphyrin Species on Photophysics

We further investigated and compared metallic T4 porphyrins with $H_2$T4. Figure 3.6 shows absorption and photoluminescence spectra of the porphyrins with DNA at various molar ratios of nucleobases to porphyrin ranging from 0 to 24. Absorption spectra (Figure 3.6a through Figure 3.6e) show that all these porphyrins have prominent Soret bands at

400-440 nm and Q bands at 500-750 nm. $H_2T4$ displays four bands from Q transitions, while metalloporphyrins only shows two peaks due to their increased symmetry.[56, 105]

In detail, in the absence of 24-mer DNA, $H_2T4$, ZnT4, PtT4, PdT4, and CuT4 display Soret peaks at 422, 435, 401, 417 and 425 nm, respectively. These Soret bands demonstrate strong hypochromic and bathochromic shifts as the amount of DNA is increased; $H_2T4$, ZnT4, PtT4, PdT4 and CuT4 exhibit 40, 28, 46, 45 and 34% hypochromism and 16, 11, 14, 15 and 9 nm red-shifts, respectively, at the DNA/porphyrin ratio of 24:1.

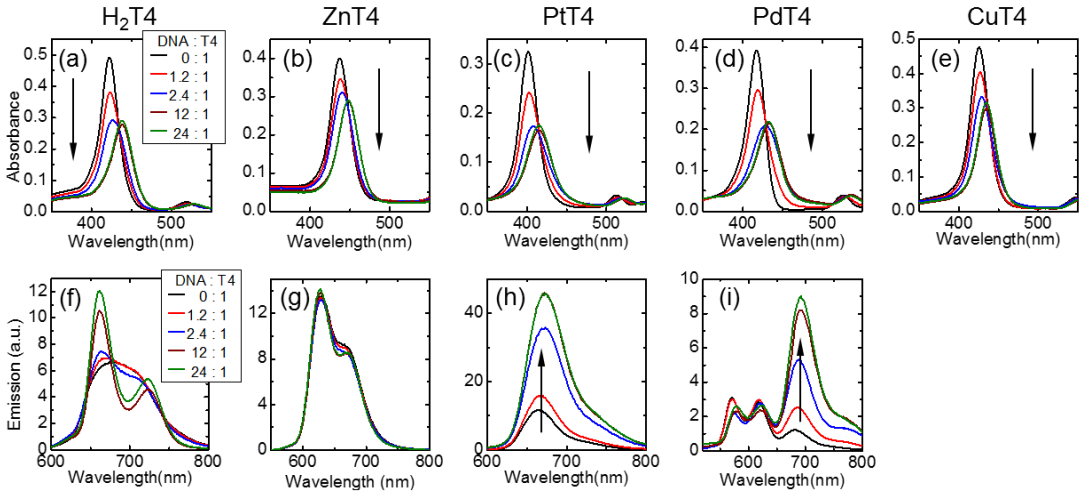


Figure 3.6. Steady-State Absorption (Upper Row) and Emission (Bottom Row) Spectra of (a) and (f) $H_2T4$. (b) and (g) ZnT4. (c) and (h) PtT4. (d) and (i) PdT4. (e) CuT4 upon Adding DNA.

In summary, the strong red shifts attribute to nucleobases stacking with porphyrin cores, perturbing π-transitions of porphyrins.[106-109] It is worth noting that the porphyrins can

also interact with DNA electrostatically, as four cationic pyridine ligands of the porphyrins bind to negatively charged DNA phosphate backbone.[108, 110]

In parallel, the photoluminescence spectra of porphyrins at different amounts of DNA show specie dependence behaviors (Figure 3.6f through i). Without DNA strands, $H_2T4$ demonstrate strong fluorescence from 650 to 750 nm (Figure 3.6f).[57] This broad emission signature is due to a solvent effect,[111] and becomes better resolved in less polar solvents, such as ethanol, or with interaction with DNA strands.[49] With the molar ratio of DNA/ $H_2T4$=12 or higher, two distinct fluorescence peaks at ~660 and 730 nm are observed. However, the total intensity (i.e. area under the curve) remains roughly constant for all the conditions examined. ZnT4 fluoresces from 600 to 700 nm. The fluorescence signature of free solution ZnT4 molecules is well defined with two distinct emission peaks at ~620 and 660 nm compared to $H_2T4$. The emission spectra are nearly the same for all DNA/porphyrin ratios from 0 to 24. Despite minor differences in their emission characteristics, both $H_2T4$ and ZnT4 porphyrins demonstrate similar photophysics in that after excitations to their respective Soret bands ($S_2$), rapid relaxation to lower-lying Q-bands ($S_1$) occurs from which fluorescence emission is generated.

Figure 3.6 shows the emission spectra of PtT4 which are starkly different from those of $H_2T4$ and ZnT4. The PtT4 system undergoes an intersystem crossing efficiently from a singlet to a triplet state, resulting in phosphorescence peaking at ~680 nm.[51] The phosphorescence signal increases with DNA addition, reaching a 4 times greater signal as the DNA/porphyrin ratio increases from 0 to 24. The increase of the emission signals is

attributed to better isolation of the porphyrins from oxygen molecules dissolved in buffer which would otherwise interact with the triplet state, forming singlet oxygen and/or superoxide, and thereby diminishing the emission.[92, 112] The PtT4-DNA interaction reduces the accessibility of the oxygen molecules and protects the porphyrin from emission quenching via energy transfer. The same quenching mechanism is not observed with $H_2$T4 and ZnT4 because their emissions are primarily from singlet states, which have excited state lifetimes that are significantly shorter than diffusion timescale of dissolved oxygen.[56]

Interestingly, PdT4 molecules exhibit both singlet and triplet state emissions. Figure 3.6i shows three distinct emission features of PdT4, where the 2 peaks at ~580 and 620 nm correspond to fluorescence, and the signature at ~690 nm is phosphorescence.[49, 92, 113] A fraction of the excited states emits fluorescence, while the radiative decay of the triplet state is efficient enough to generate phosphorescence. As seen with $H_2$T4 and ZnT4 in Figure 3.6f and g, the fluorescence features of PdT4 do not change significantly with the addition of DNA. In contrast, the phosphorescence signal increases significantly with DNA, demonstrating five times enhanced intensity at the DNA/porphyrin ratio of 24:1 compared with the emission in the absence of DNA. Similar to the PtT4 case, DNA plays a critical role in isolating PdT4 from oxygen molecules that quench the phosphorescence.[92] CuT4 also emits phosphorescence, but it is not measured here because its signal is weak since its emission lifetime is very short-lived.[96, 114, 115]

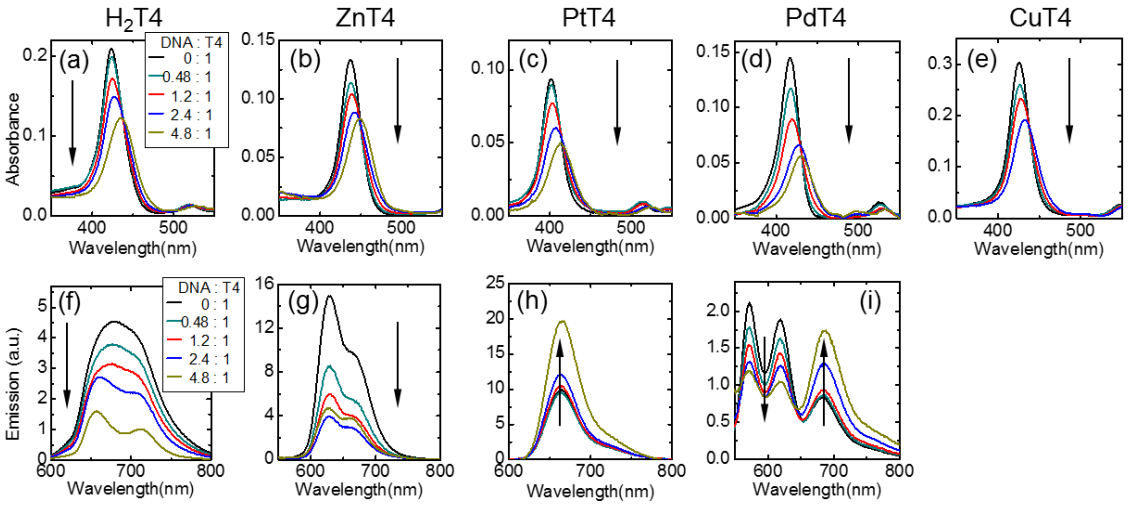


Figure 3.7. Steady-State Absorption (Upper Row) and Emission (Bottom Row) Spectra of (a) and (f) $H_2T4$, (b) and (g) ZnT4, (c) and (h) PtT4, (d) and (i) PdT4, and (e) CuT4.

Figure 3.7 shows absorption and emission spectra of porphyrins interacting with DNA-SWCNT. The Soret bands demonstrate hypochromic and bathochromic shifts with increasing DNA-SWCNTs, as seen with porphyrins interacting with DNA. At the DNA/porphyrin ratio of 4.8:1, $H_2T4$, ZnT4, PtT4, PdT4 and CuT4 display 12, 12, 11, 13 and 7 nm redshifts and 41, 38, 47, 60 and 37% hypochromism, respectively. Interestingly, the bathochromism and hypochromism are more prominent with DNA-SWCNT than with DNA alone, as similar degrees of shifts are observed with DNA-SWCNTs at lower porphyrin/DNA ratios; for example, olive curves in Figure 3.7a-e (DNA/porphyrin = 4.8) display similar shifts with brown curves in Figure 3.6a-e (DNA/porphyrin = 12). However, our estimation of the number of DNA per nanotube is somewhat uncertain because the DNA conformation may differ at the SWCNT surface. In fact, we were unable to observe G-quadruplex-induced signals in circular dichroism (CD) spectra from the SWCNT-bound DNA samples.

The emission signals of porphyrins with DNA-SWCNTs show important differences from those with DNA alone. The emission spectra of $H_2$T4, ZnT4, and PdT4 were obtained using 5-nm slit widths for both excitation and emission, while 8-nm slit widths were used to record PtT4 emission. The emission signals are corrected for absorption strengths at the excitation wavelengths, which are 421, 437, 401, and 417 nm for $H_2$T4, ZnT4, PtT4, and PdT4, respectively. While $H_2$T4 and ZnT4 porphyrins interacting with DNA display largely unchanged emission, their fluorescence intensities gradually decrease with increasing concentration of DNA-SWCNTs. More than half of the fluorescence intensity is quenched at the DNA/porphyrin ratio of 4.8:1 (olive curves in Figure 3.6f and g). It is also noted that with increasing DNA-SWCNT concentration, $H_2$T4 fluorescence becomes better resolved (Figure 3.7f), as seen with porphyrin-DNA (Figure 3.6f). DNA strands bind strongly to the porphyrin, while solubilizing nanotubes in aqueous solution, and the interaction between porphyrin and carbon nanotube results in emission quenching. Here, no SWCNT aggregation was apparent under the experimental conditions. Previous studies on porphyrin-tethered carbon nanotubes showed strong charge transfer interaction between porphyrins and carbon nanotubes, which suppressed porphyrin emission.[46, 54, 97]

The phosphorescence signals of PtT4 are also modulated by carbon nanotubes as shown in Figure 3.7h, where a smaller increase of the emission intensity is observed with DNA-SWCNTs (Figure 3.7h) compared to DNA alone (Figure 3.6h). At DNA/porphyrin ratio of ~2.4, the emission intensity increases by ~20% in the presence of SWCNTs, whereas a ~250% increase is observed with PtT4 with DNA strands alone. The fact that the

presence of SWCNTs lessens the increase of PtT4 emission suggests three possible quenching mechanisms. Photo-excited electrons of the porphyrin can be either transferred to SWCNTs before the intersystem crossing or quenched directly from a triplet state (T) by nanotubes. If the DNA conformation changes at the nanotube surface, the PtT4 molecules may also be more exposed to dissolved oxygen molecules. These quenching mechanisms are discussed below in detail with emission lifetime and photoelectrochemical measurements.

The effects of carbon nanotubes on both fluorescence and phosphorescence emission are also observed with PdT4 (Figure 3.7i). The fluorescence peaks at ~580 and ~620 nm gradually decrease with increasing concentrations of DNA-SWCNTs, displaying approximately half of the original PdT4 emission signal at the ratio of DNA/PdT4 =2.4 (shown in blue). While the fluorescence signals are quenched with increasing DNA-SWCNTs concentrations, the phosphorescence signature at ~690 nm is gradually enhanced. However, the extent of increase in the triplet state emission is significantly less for DNA-SWCNTs than the case with no SWCNTs; for example, 50 vs. 400% increases are observed at the DNA/PdT4 ratio of 2.4. These results are consistent with SWCNT-induced fluorescence quenching in $H_2$T4 and ZnT4 and the smaller increase of PtT4 phosphorescence in the presence of carbon nanotubes. The emission of CuT4 in the presence of DNA-SWCNTs was not quantifiable due to its weak intensity.

### 3.3.3 Photoelectrochemistry Results

Along with the optical measurements of DNA and SWCNT-DNA with various porphyrins, the photoelectrochemical measurements were carried out to further shed light into the interactions and photophysics within the SWCNT-DNA porphyrin nanohybrids. Figure 3.8 presents the benefit of DNA-assisted assembly of SWCNTs and $H_2T4$ over anionic pyrene derivative (i.e. PBA). Under the same experimental conditions (e.g. amount of SWCNTs and deposition method), DNA-templated $H_2T4$-SWCNT shows twice-larger photocurrents than PBA-assembled sample. These results verify the role of DNA unambiguously, while facilitating the charge transfer process between $H_2T4$ and SWCNT.

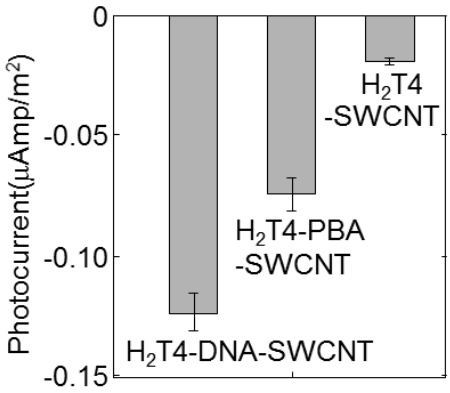


Figure 3.8. Photocurrent of SWCNT-DNA- $H_2T4$, SWCNT-PBA- $H_2T4$, and SWCNT-$H_2T4$ Films under White Light Excitation.

As discussed in Chapter 1, semiconducting nanotubes are preferred to serve as photoanode due to their ability of the shuttling separated charges. To examine this

hypothesis, we used highly enriched (99%) semiconducting and metallic nanotubes, which were sorted by density-gradient ultracentrifugation techniques (Figure 3.9).[94]

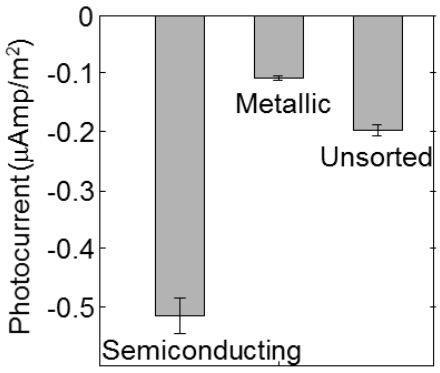


Figure 3.9. Short-Circuit Photocurrent of SWCNT-DNA-$H_2$T4 Films Made of Semiconducting, Metallic and Unsorted Tubes.

Here, we observed a significant enhancement in short-circuit photocurrent from the film based on semiconducting nanotubes as compared to the films with unsorted and metallic SWCNTs. This result shows that the presence of metallic tubes limits the efficiency of donor-acceptor nanohybrids in photoelectrochemical cells. Metallic SWCNTs can suppress the overall performance due to continuous electronic pathways, which significant reduces excited states lifetime and leads fast relaxation photo-generated electrons. With Soret band excitation at ~5 W/cm$^2$, photocurrents of 0.5 μAmp cm$^{-2}$ were obtained from the semiconducting nanotube film, providing an incident photon-to-current efficiency (IPCE) of nearly 1%. In comparison, only ~0.1 μAmp cm$^{-2}$ was measured from the metallic tube film under the same experimental conditions. The 5-fold photocurrent enhancement demonstrates the importance of the nanotube types in donor-acceptor light

harvesting systems. The development of better SWCNT sorting methods will further improve in the quality of SWCNT for solar energy conversion.

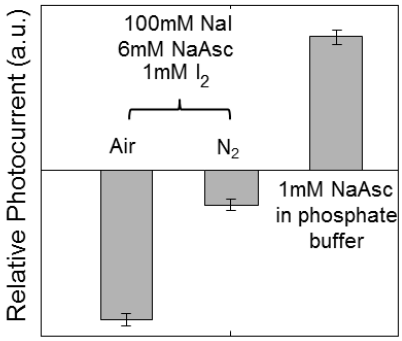


Figure 3.10. Relative Photocurrent of Semiconducting SWCNT-DNA-$H_2$T4 Film as a Function of Electrolyte Conditions.

To demonstrate the role of the electrolytes, we explored two redox couples as shown in Figure 3.10. A semiconducting SWCNT film generated cathodic (negative) photocurrents in the aqueous solution of 0.1 M NaI, 1mM $I_2$ and 6 mM Asc at pH 5.5, where separated holes were collected at the ITO working electrode. The photo-excited electrons are meditated via the redox couple in electrolyte solution. Given the transparent electrolyte solution, presence of $I^{3-}$ is negligible since its absorption peak around ~460 nm is not observed in electrolyte. The 460 nm absorption indicates the conversion of $I^{3-}$ to $I^-$ in the presence of Asc.[116] With nitrogen purging, molecular oxygen concentration is reduced, leading to drastic decrease of photocurrents; oxygen concentration in electrolyte is important for charge separation in nanohybrid films.[117]

In contrast, negative (anodic) photocurrents were measured in 1 mM Asc solution at pH 7.5 from the same nanohybrids film. In this case, $N_2$ purging barely influenced the signal magnitude. The photo-excited electrons from the porphyrin molecules were injected to the semiconducting nanotubes and transported to the working electrode. The oxidized chromophore was subsequently reduced by the redox couple in electrolyte, which is described in in Equation (4). An electronic circuit is completed by diffusion and reduction of DAsc at the counter electrode. Therefore, the photocurrent direction can be modulated by changing the electrolyte conditions, which may result from the bipolar characteristics of carbon nanotubes previously demonstrated in the electronic studies.[118]

$$\mathrm{Asc} \rightarrow \mathrm{DAsc} + 2\,\mathrm{e}^- + 2\,\mathrm{H}^+ \qquad (4)$$

The interactions between photo-excited porphyrins and SWCNTs are exploited for light harvesting in a photoelectrochemical cell. The absorption spectra of deposited SWCNT-DNA with various porphyrins on an ITO electrode are shown in Figure 3.11. With Asc and its oxidized product, DAsc, as a redox couple in phosphate buffer, porphyrin-based complexes generate consistent anodic photocurrents, where photo-induced electrons are collected at the ITO. Figure 3.11b shows typical, time-resolved photocurrents from a PdT4-DNA-SWCNT film sample. Irradiation at 440 nm rapidly produces photocurrents at approximately 700 nAmp/cm$^2$ which becomes zero with the light turned off. These photocurrents originate from the porphyrin photo-absorption as the Soret and Q-band absorption signatures match well with photocurrent signals (Figure 3.11c).

Here, photocurrent signals as a function of excitation wavelength are shown in blue dots, while absorption spectrum of the complexes in a deposited film is presented in red. The film absorption spectrum is plotted after subtraction of the DNA-SWCNT absorption, representing porphyrin signatures only. This observation confirms a charge transfer process from the Q-band ($S_1$) to the bound nanotube, while not excluding the possibility of $S_2$ state participation as well. Our photoelectrochemical measurements suggest that the photo-generated electron-hole pairs in porphyrin molecules are separated at the DNA-SWCNT interface and the electrons are collected at the working electrode. The oxidized chromophore molecules are then regenerated by Asc, converting into DAsc which is subsequently reduced at the Pt counter electrode in the photoelectrochemical cell.

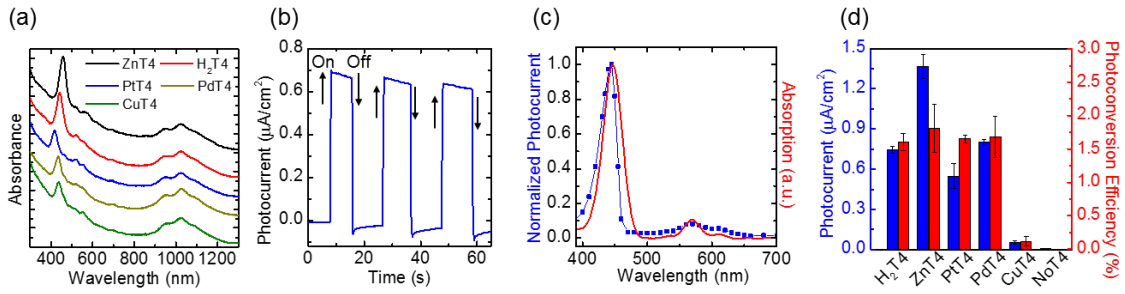


Figure 3.11. (a) Absorption Spectra of $H_2T4$, ZnT4, PtT4, PdT4, and CuT4 Based DNA-SWCNT Films. (b) Photocurrent of PdT4-DNA-SWCNT Complexes with Photo-Excitation at 440 nm. (c) Action Spectra of ZnT4-DNA-SWCNT Complexes. (d) Photocurrents and Corresponding Photo-Conversion Efficiencies of the Deposited DNA-SWCNT Films with Various Porphyrins and without Any Porphyrin.

The photocurrents of $H_2T4$, ZnT4, PtT4, PdT4 and CuT4 nanohybrids and their photo-conversion efficiencies are shown in Figure 3.11d. Here, a nanohybrid film without any photosensitizers was also tested as a control; negligible photocurrent was observed. This evidences that porphyrins were serving as charge donors instead of DNA or nanotubes.

The films incorporating $H_2$T4, ZnT4, PtT4, and PdT4 show approximately 1.5% photo-conversion efficiencies, indicating that the intersystem crossing barely affects photo-conversion performance. It is interesting that PtT4 generates a photocurrent comparable to those of $H_2$T4 and ZnT4. The result is striking because PtT4 does not exhibit fluorescence, hence it is likely to undergo intersystem crossing, rendering a phosphorescence and 100 or more times longer emission lifetime than of $H_2$T4 or ZnT4, which majorly experiences fluorescence.[92] In each case, the rate of electron injection from $S_1$ into SWCNT/ITO must compete with intersystem crossing. The explanation may be that, like PdT4, PtT4 has higher energy $S_1$ state, which in turn means the driving force for electron injection ought to be greater. An alternative explanation could be that only a subpopulation of porphyrin is properly disposed for efficient electron injection. The films containing copper porphyrin nanohybrids generated significant smaller photocurrents (~40 nAmp) with the same experiment conditions. The photocurrent and photo-conversion efficiency with CuT4 may result from extremely short excited singlet-state lifetime in CuT4, which is roughly 65 fs.[119] Therefore, it is unlikely for electron transfer to SWCNTs to occur.

We also examined the porphyrin-DNA-SWCNT film sample processed with the buffer containing $Li^+$ which is known to destabilize G-quadruplex conformation[120] instead of $Na^+$. We observed the photocurrents comparable to those in Figure 3.11, suggesting the G-quadruplex may not be involved in the photo-conversion processes.

### 3.3.4 PtT4 Lifetime and Singlet Oxygen Measurements

The interactions between chromophore porphyrins and SWCNTs were investigated via examining singlet oxygen ($^1O_2$) emission from PtT4. Singlet oxygen, which emits at ~1270 nm,[121, 122] is generated from dissolved oxygen in buffer by accepting energy transfer from the triplet state of photo-excited porphyrin.[92, 122, 123] Figure 3.12a shows the singlet oxygen emission in the presence of PtT4 with DNA and DNA-SWCNTs. The singlet oxygen emission signal diminishes in the presence of DNA which protects porphyrin chromophores from interacting with the oxygen molecules in solution, thereby slowing the buildup of singlet oxygen.[92] In comparison shown in Figure 3.12b, anionic surfactant SC molecules barely changed the emission signals of singlet oxygen even at an orders-of-magnitude higher concentration than the DNA strands, consistent with effective screening by oligonucleotides. The presence of carbon nanotubes generates significantly greater quenching of the singlet oxygen emission. PtT4 molecules with DNA-SWCNTs demonstrate nearly complete quenching, while PtT4 with SC-SWCNTs shows approximately 70% quenching at the same nanotube concentrations. This observation indicates that the nanotube does not greatly alter the porphyrin/DNA interaction. Thus, one would expect an increase of singlet oxygen emission from PtT4 samples with DNA-SWCNTs, for example, if the DNA is unable to protect the porphyrins from interaction with oxygen molecules due to any change of its conformation. However, several mechanisms may be at work in nanotube-induced quenching of singlet oxygen emission. Carbon nanotubes interacting with PtT4 molecules may intercept the photo-excited electrons before they undergo the intersystem crossing or directly quench triplet states,

thus preventing singlet oxygen generation.[92] It is also possible that SWCNTs can directly interact with the singlet oxygen and quench the emission to some degree.[124]

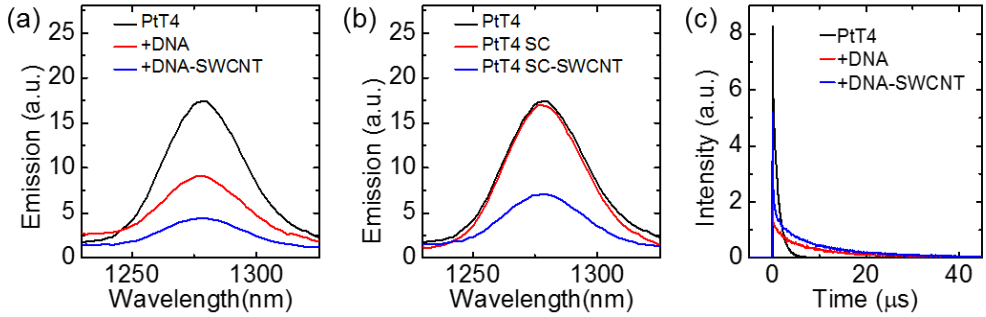


Figure 3.12. Near-IR Emissions of Singlet Oxygen Generated by PtT4 in the Presence of (a) DNA Strands and DNA-Coated SWCNTs, (b) SC and SC Encapsulated SWCNTs. (c) Excited State Decay Measurements of PtT4 with DNA and DNA-SWCNTs.

To probe the prevalence of nanotube interaction with porphyrins via their singlet-state versus triplet-state, we performed the excited state lifetime measurements of PtT4 with DNA and DNA-SWCNTs (Figure 3.12c). The phosphorescence lifetime of PtT4 alone demonstrates a single-exponential decay function with a decay time of approximately 1.0 μs, which is affected by oxygen molecules in buffer. In the presence of DNA and DNA-SWCNTs, the PtT4 emission lifetime drastically increases due to a better isolation of porphyrins from oxygen molecules in solution. Here, two distinct (fast and slow) components are observed, as the signal is best fitted with a double exponential decay function. In the presence of the DNA, the fast decay of ~1.9 μs and the slow decay of ~9.9 μs are measured. In the presence of DNA-SWCNTs, decay lifetime components of ~1.1 and ~9.3 μs are recorded. The fact that both slow components with DNA and DNA-SWCNTs are similar indicates that the presence of SWCNTs does not play significant

roles in phosphorescence emission and that SWCNTs do not quench the triplet state of the porphyrins directly.

### 3.3.5 Charge Transfer Mechanisms in Nanohybrids

Our results suggest that charge transfer to nanotubes may occur from $S_1$ and/or $S_2$. For the $S_2$ state, a charge transfer process may be driven by the high energy, but $S_2$ has a very fast internal relaxation time.[125] In contrast, the lower-lying $S_1$ state may have a comparable timescale with a transfer reaction rate. Our photoelectrochemical measurement provides direct evidence of a charge transfer from $S_1$ to nanotubes.

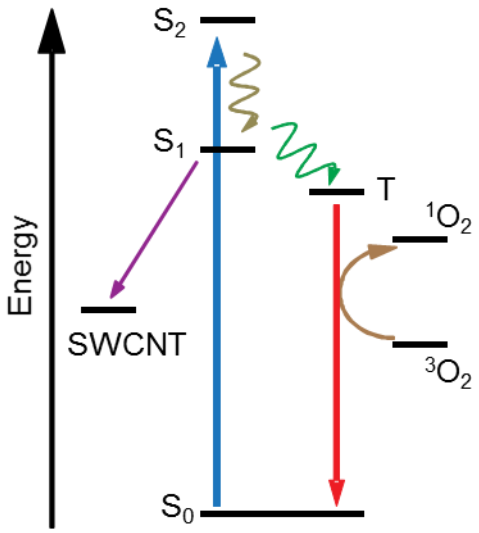


Figure 3.13. Proposed Photophysical Mechanism.

With all the aforementioned observations and discussions, we summarize the photophysical interactions in porphyrin-DNA-nanotube complexes in Figure 3.13. The

most probable scenario upon photo-excitation at the Soret band ($S_2$) is that the system rapidly relaxes to the lower-lying singlet state ($S_1$), where an electron may be transferred to nanotubes and converted to photocurrents. Once electrons undergo an intersystem crossing to a triplet state (T), they return to the ground state ($S_0$) via either emitting phosphorescence or generating singlet oxygen molecules via energy transfer which emit in the near-IR. The photoelectrochemical measurement results favor a fast electron transfer mechanism from photo-excited chromophores to SWCNTs before intersystem crossing, consistent with our singlet oxygen emission experiments. Once the intersystem crossing to the triplet state is completed, especially in PtT4 and PdT4, the interaction of the triplet state with oxygen molecules may yield $^1O_2$, which emits phosphorescence in the near-IR spectrum. However, CuT4 likely experiences different relaxation pathways as electrons excited to $S_2$ may bypass $S_1$ and transition to a triplet state,[119] which probably explains the weak photocurrents from CuT4-nanotube complexes.

## 3.4 Summary

SWCNT/porphyrin nanohybrids were assembled using DNA to harvest light and convert photon energy into photocurrents. We elucidated the photophysical processes in the light-harvesting nanohybrids made of semiconducting SWCNT and various T4 porphyrins. The absorption spectra of porphyrins demonstrated significant bathochromic and hypochromic shifts upon adding 24-mer DNA and DNA-coated SWCNTs. The singlet transition signals (fluorescence) of $H_2$T4, ZnT4 and PdT4 were barely altered in the presence of DNA oligonucleotides, while a largely fluorescence quenching occurred with

DNA-SWCNT nanohybrids. The phosphorescence signatures of PtT4 and PdT4 significantly enhanced with increasing DNA concentration, because DNA molecules insulated porphyrins from oxygen molecules. Thus, oxygen could not quench porphyrin phosphorescence via energy transfer. In contrast, phosphorescence increased to a significantly less extent when DNA-SWCNTs were introduced. The transient measurements showed that the triplet state lifetime was barely charged with DNA-SWCNTs, indicating that SWCNTs quenched the porphyrin emission primarily from the singlet states before the intersystem crossing. With Asc and DAsc as a redox couple, photocurrents were measured in a photoelectrochemical cell. Stable anodic photocurrents were obtained from all porphyrin complexes with similar magnitudes except CuT4. We estimate ~1.5% quantum yield for all porphyrins but CuT4 which induces a rapid relaxation. Our observation suggests that different combinations of SWCNT and porphyrin species may be further explored to maximize charge transfer, which could be useful for designing light-harvesting donor-acceptor complexes. In parallel, developing specific DNA-targeting small molecules such as porphyrins and phthalocyanines can provide a selective DNA/chromophore binding. Such efforts could form the basis for a novel platform to study charge transfer processes at the nanoscale.

# CHAPTER 4. REGENERATIVE SWCNT-DNA-PORPHYRIN HYBRIDS

## 4.1 Introduction and Design

In natural photosynthesis, a reaction center helps collect sunlight in form of intricate light-harvesting complexes combined proteins and pigments. A charge separation and electron transfer reactions take place at the reaction center. Inspired the natural photosynthesis system, synthetic light-harvesting complexes have been heavily investigated for solar energy conversion. Gust et al. created series of donor-acceptor light harvesting complexes and studies their opto-electrochemical properties.[126, 127] Gust and his co-worker showed that each component in donor-acceptor complexes can be accurately tuned and facilitated for intra/inter-molecular charge transfer.[128] A portion of excited electron energy was downregulated to prevent the complexes being damaged from intensive light illumination, mimicking the natural protecting mechanisms against photodegradation.[129, 130] Several other groups constructed and investigated multiple novel donor-acceptor complexes with promising photoelectrochemical properties for artificial photosynthesis.[131-133]

Despite the recent advances in creating novel synthetic light-harvesting complexes and studying the charge transfer processes, the system stability remains one of the most critical issues in the way of applying donor-acceptor complexes for solar energy

conversion applications. In particular, photodegradation of photosensitizing donor is prevalent, resulting a real-time decline of energy conversion efficiency. At demonstrated in Chapter 3, photoexcited porphyrin chromophores as popular and effective photosensitizer molecules may trigger energy transfer from the chromophore to solubilized molecular oxygen and generates chemically reactive oxygen species that can oxidize and damage the porphyrin molecules.[134-136] Thus, it is necessary to develop a strategy that can prevent or alleviate such inevitable adverse photodegradation process, which would promote donor-acceptor complexes as feasible solar energy conversion materials and novel platforms to understand charge transfer processes.[137]

Here we design synthetic light-harvesting molecular donor-acceptor complexes capable of counteracting photo-induced degradation. To achieve this concept, we develop a facile oligonucleotide-based assembly strategy that allows us to exchange photo-damaged donor molecules, while acceptors remain intact in a photoelectrochemical cell in Figure 4.1a. Such strategy could form a basis for improving overall system performance and service lifetime of donor-acceptor complexes for light harvesting.

We use anionic gallium (III) protoporphyrin IX chloride or GaPP (Figure 4.1b) and high-purity semiconducting SWCNTs as a model of molecular donors and acceptors. We use modified 30-mer oligonucleotide strands, originally identified via an *in-vitro* selection process for selectively binding hemin or iron (III) protoporphyrin IX chloride (FePP), which has the same molecular structure as GaPP except for a change of the metal cation.[138] We demonstrate that photo-bleached porphyrins can be dissociated from

DNA-coated carbon nanotubes immobilized on an ITO surface, and that the photocurrents fully recover after fresh GaPP molecules are reintroduced to the system for re-association.

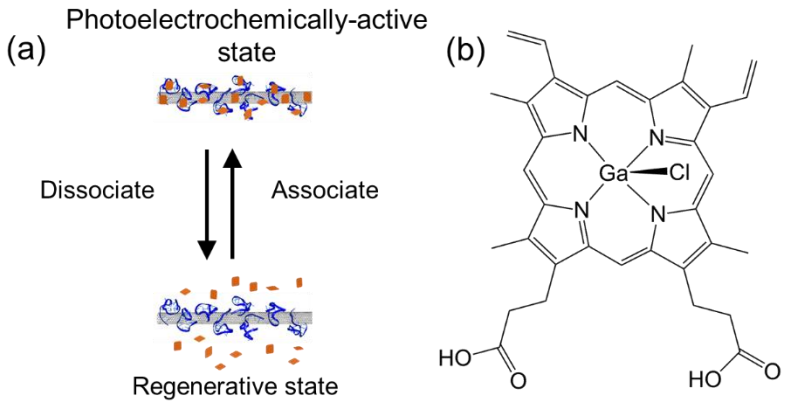


Figure 4.1. (a) Schematic of a Light-Harvesting Photoelectrochemically-Active System Capable of Reversibly Assembling Donor Chromophores. (b) Gallium (III) Protoporphyrin IX Chloride (GaPP).

## 4.2 Materials and Methods

The light-harvesting donor-acceptor complex samples are prepared by depositing DNA-dispersed carbon nanotubes in aqueous solution on a membrane using a vacuum filtration system, followed by transferring them onto an ITO substrate and immersing the transferred sample in a GaPP-containing solution for 1 hour. The 30-mer single-stranded DNA oligonucleotides (T12PS2M or 5'–$T_{12}GTG_3TAG_3CG_3TTGG$–3') are used for noncovalently linking GaPP, while dispersing nanotubes in aqueous solution. The G-rich part of the DNA strand forms a G-quadruplex conformation, facilitating target porphyrin recognition, while the 5'-$T_{12}$ leader sequence is designed to adhere to the nanotube surface.[39]

The detailed SWCNT processing and film making procedures are described in Chapter 2. Specifically, to functionalize GaPP, the films were immersed in the solution containing 6 μM GaPP, 100 mM KCl, and 10 mM $MgCl_2$ in Tris buffer (pH 8.0) with 30 vol. % DMSO for 30 min. For regeneration experiments, the GaPP-DNA-SWCNT films were immersed in 30 wt. % hydrogen peroxide for 1 hour to disassociate GaPP molecules from the films. We explored longer incubation times such as 3 and 6 hours, but no significant differences in GaPP absorption of the Soret band were observed, suggesting that the majority of GaPP molecules are disassociated within 1 hour. Following the dissociation, the films were incubated again in a mixture of Tris buffer and DMSO (7:3 by volume) containing 6 μM GaPP, 100 mM KCl, and 10 mM $MgCl_2$ at pH 8.0 for 30 min. The procedure can be repeated multiple times as there were no apparent changes in the absorption spectra and photoelectrochemical measurements.

As a control, we employed Fenton reaction to cleave DNA and irreversibly release photo-bleached porphyrin. Here, the DNA-SWCNT film was immersed in 100 mM $H_2O_2$ solution with 50 μM of $FeSO_4$ for 1 hour. The film was then clean by DI water. Two control DNA sequences of 24-base-long consecutive poly thymine (T24) and poly adenine (A24) incorporated in DNA-SWCNT films are also tested.

For photoelectrochemical measurement, the experimental setup is described in Chapter 2. In short, the complexes deposited on the ITO slide and a platinum-coated glass were used as the working and counter electrodes, respectively. The reference electrode was short-

circuited with the counter electrode. Several combinations of ferrocyanide ($Fe(CN)_6^{4-}$) and ferricyanide ($Fe(CN)_6^{3-}$) were examined as the redox couple in aqueous solution, listed in Table 4.1.

Table 4.1. Electrolytes Used in This Chapter.

| | |
|---|---|
| (i) 150 mM ferrocyanide and 150 mM ferricyanide | Figure 4.3 and Figure 4.9 |
| (ii) 150 mM ferrocyanide and 10 mM ferricyanide | Figure 4.13 |
| (iii) 250 mM ferrocyanide and 50 mM ferricyanide | Figure 4.4 |
| (iv) 50 mM ferrocyanide and 250 mM ferricyanide | Figure 4.4 |
| (v) 10 mM Asc | Figure 4.3 |

## 4.3 Results and Discussion

The absorption spectrum of the deposited GaPP-DNA-SWCNT film on the ITO substrate is shown in Figure 4.2a. Here, two prominent features are observed. The Soret band of GaPP is found at ~410 nm, while the peak around 1000 nm arises from the electronic transition between the second van Hove singularities ($E_{22}$) of the semiconducting SWCNTs.[139, 140] Minor signatures between 450 and 600 nm such as Q band of GaPP and $E_{33}$ of SWCNT are also presented. The prominent Raman features (i.e. RBM, D, G and G' bands) of DNA-SWCNTs nanohybrids are shown in Figure 4.2b. A minimal D peak suggests that the noncovalent interaction of DNA with the nanotube surface does not disturb the electronic band structure of the nanotubes significantly.

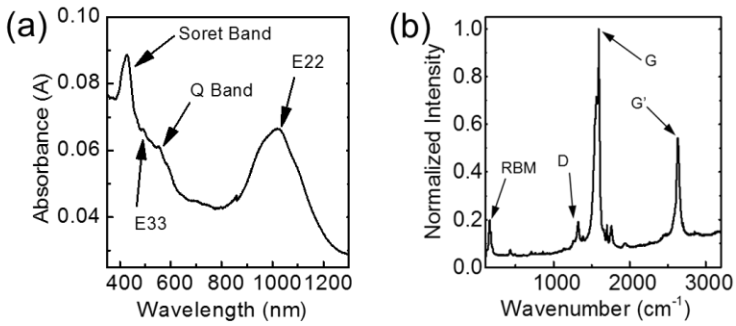


Figure 4.2. (a) Absorption Spectrum of GaPP-DNA-SWCNT Film. (b) Raman Spectrum of the GaPP-DNA-SWCNT Complex Film Recorded with Laser Excitation at 633 nm.

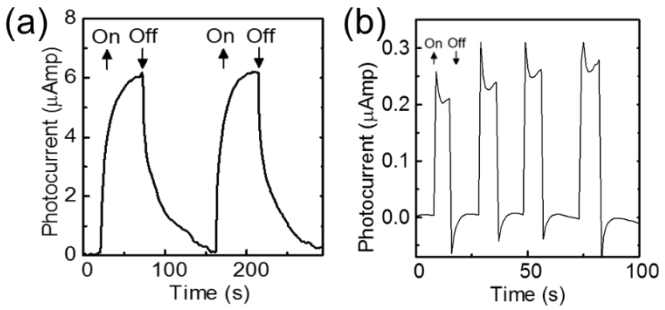


Figure 4.3. (a) Photocurrent Generated by GaPP-DNA-SWCNT Complexes. (b) Photocurrent of GaPP-DNA-SWCNT Film Obtained with the Electrolyte Containing 10 μM Asc, Demonstrating a Significantly Faster Photocurrent Kinetics than with $Fe(CN)_6^{3/4-}$.

The use of the GaPP-DNA-SWCNT complexes for photocurrent generation was examined in a photoelectrochemical cell using 150 mM ferrocyanide ($Fe(CN)_6^{4-}$) and 150 mM ferricyanide ($Fe(CN)_6^{3-}$) as a redox couple. Figure 4.3a shows that the limiting photocurrent of approximately 6 μAmp was measured from the complex sample containing 4 μg of carbon nanotubes when the 350-700 nm light at ~400 mW/cm$^2$ was turned on, and quickly diminished with the light off. The kinetics of the photocurrents in Figure 4.3a is attributed to $Fe(CN)_6^{3-/4-}$ as other redox couples such as Asc/DAsc under

similar conditions demonstrates fast photocurrent activities in response to light irradiation (Figure 4.3b).[141]

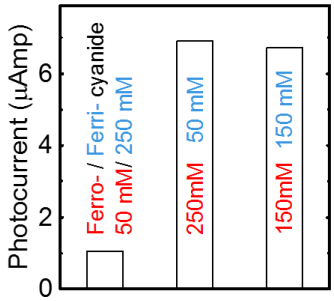


Figure 4.4. Photocurrents of the GaPP-DNA-SWCNT Film at Various $Fe(CN)_6^{3-/4-}$ Concentrations.

We found that ferrocyanide plays a more important role in the photocurrent generation than ferricyanide. We varied concentrations of ferricyanide/ferrocyanide while their total amount was fixed at 300 mM (Figure 4.4). The photocurrents generated with 250 or 150 mM ferrocyanide were nearly identical at approximately 6.5 μAmp, whereas only ~1 μAmp was observed with 50 mM ferrocyanide. In these anodic photocurrent experiments, the electrons generated from the photo-irradiated sample are collected at the ITO, the working electrode. Photo-absorption of GaPP chromophores leads to charge separation at the interface with carbon nanotubes.[142, 143] The photo-generated electrons are transferred to the carbon nanotubes, which shuttle the electrons to the working electrode.[43] The oxidized GaPP molecules are reduced by ferrocyanide in the electrolyte which becomes an oxidizing product, ferricyanide, shown in Equation (5). The ferricyanide molecules diffuse to the platinum counter electrode and become reduced to ferrocyanide, completing the entire photoelectrochemical circuit.[141]

$$[Fe(CN)_6]^{3-} + e^- \rightarrow [Fe(CN)_6]^{4-} \quad (5)$$

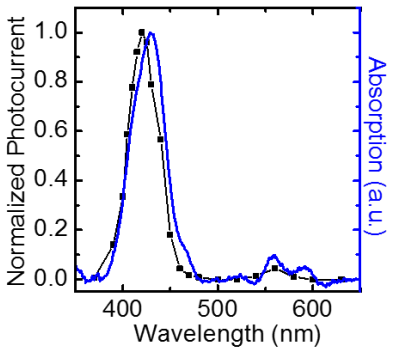


Figure 4.5. Spectral Resolved Photocurrents (Black Dots) of GaPP-DNA-SWCNT Film with GaPP Absorption Spectrum (Blue Line).

The photo-conversion process is confirmed by the action spectra in Figure 4.5, where photocurrent and optical absorption are plotted as a function of irradiating wavelength from 350 to 650 nm. The black-dotted line indicates the normalized photocurrent collected under light illumination at the corresponding wavelengths; the absorption spectrum of the GaPP portion of the GaPP-DNA-SWCNT complexes with the SWCNT background subtracted. Both spectra are in excellent agreement with regard to GaPP signatures at ~410 nm (Soret) and between 550 and 600 nm (Q band). This observation indicates that both transitions (Soret and Q) can contribute to the transfer of photo-excited electrons to the carbon nanotube acceptor.

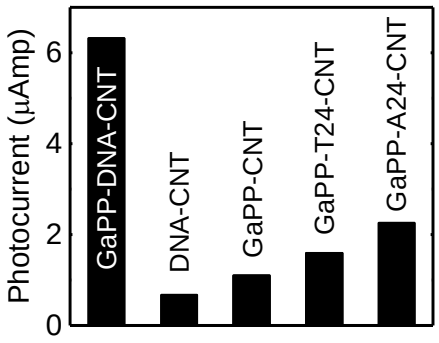


Figure 4.6. Photocurrents of GaPP-DNA-SWCNT, DNA-SWCNT, GaPP-SWCNT, GaPP-T24-SWCNT and GaPP-A24-SWCNT Films.

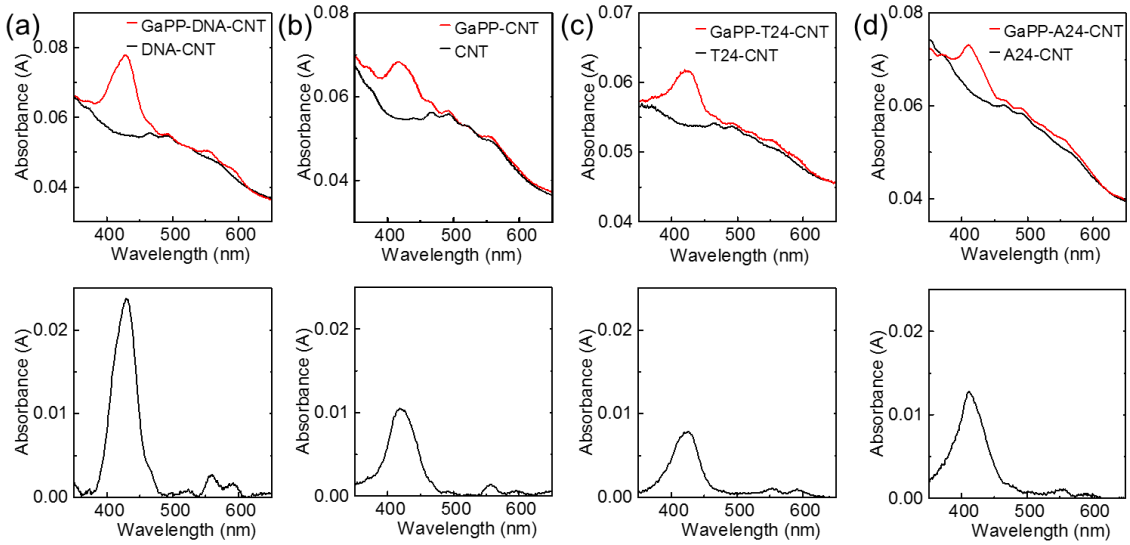


Figure 4.7. Absorption Spectra of (a) Designed DNA-SWCNT Film with and without GaPP, (b) the DNA-Free SWCNT Films with and without GaPP, (c) T24-SWCNT Films with and without GaPP, and (d) A24-SWCNT Films with and without GaPP.

The photocurrent of the GaPP-DNA-SWCNT film is compared with those of several control samples under identical conditions including the same amount of carbon nanotubes in the films (Figure 4.6). The DNA-SWCNT film with no GaPP molecules barely demonstrate measurable photocurrents (~0.5 μAmp) as expected, consistent with

GaPP chromophores being electron donors for this light-harvesting complex system, which has been shown in Chapter 2. The GaPP-SWCNT film fabricated without DNA strands also shows a small amount of photocurrent (~1 μAmp), consistent with its absorption spectrum indicating a minimal amount of GaPP chromophores (Figure 4.7). In Figure 4.7, the GaPP absorption spectra in the second-row panels are obtained by subtracting the black curves (the carbon nanotube absorption) from the red curves in the first-row panels. The signatures at ~410 nm are the Soret band, and the two less prominent features at ~560 and 580 nm are the Q bands of the GaPP. Two control DNA sequences of 24-base-long consecutive poly thymine ($T_{24}$) and poly adenine ($A_{24}$) demonstrate photocurrents of approximately 2 μAmp, about three times smaller than that of the GaPP-DNA-SWCNT film. Correspondingly, the optical absorption spectra of the control samples with T24 and A24 strands show reduced amounts of GaPP chromophores (Figure 4.7). This result indicates that the ability of T12PS2M DNA for selective binding of GaPP is well retained on the nanotubes, while nonspecific adsorption of anionic GaPP on the DNA-SWCNT film is less important.

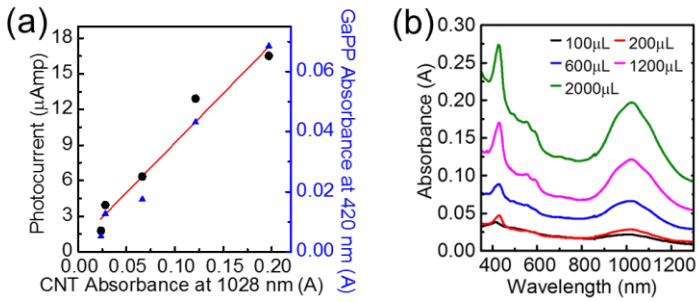


Figure 4.8. (a) Photocurrents at Different Amount of the GaPP-DNA-SWCNT Complexes (Black Dots) along with the Corresponding Soret Band Absorption of GaPP (~410 nm, Blue Dots). (b) Absorption Spectra of Various Amount of GaPP-DNA-SWCNT Films Used in (a).

The amount of light harvesting complexes used in the film determines the resulting photocurrents. Figure 4.8a shows that the increased amount of DNA-functionalized carbon nanotubes (black circles) capture a greater number of GaPP molecules (blue triangles), resulting in an increasing photocurrent. The corresponding absorption spectra showing the Soret and $E_{22}$ bands are presented in Figure 4.8b. The signatures around 410 nm are the Soret band of GaPP, while those near 1,000 nm are the $E_{22}$ transitions of semiconducting carbon nanotubes. The increasing amount of DNA-SWCNT incorporates more porphyrin chromophores, which ultimately results in generation of greater photocurrents showed in Figure 4.3.

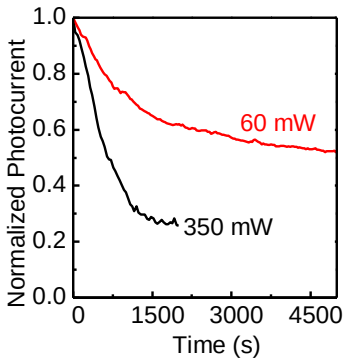


Figure 4.9. Photocurrent Decays of the GaPP-DNA-SWCNT Complexes under Light Illumination at 60 and 350 mW.

Considering the photo-degradation of porphyrins under illumination, it is important to demonstrate the resulting photocurrent decay due to the photobleaching. Here, the photoelectrochemical properties of the donor-acceptor complexes are also a strong function of light irradiation intensity as shown in Figure 4.9. The rate of photocurrent decay was much faster at 350 mW than at 60 mW which we attribute to a more rapid

photo-induced degradation of the porphyrin chromophores. With light illumination and dissolved oxygen in the electrolyte, GaPP molecules experience photo-oxidation, leading to degradation and ultimately photocurrent decay of the complex film.[134, 144]

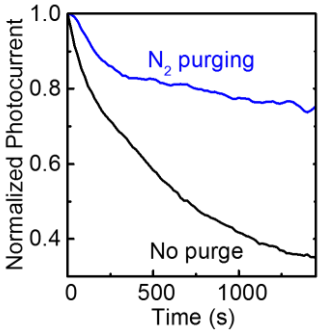


Figure 4.10. Photocurrent Decays of the GaPP-DNA-CNT Complexes in the Electrolytes with (Blue) and without (Black) $N_2$ Purging.

With the $N_2$ purged electrolyte, the GaPP-DNA-SWCNT complex film experienced a slower rate of decay, indicating that the degradation effect was relieved by reducing the amount of dissolved oxygen in the electrolyte (Figure 4.10). Here, both the electrolytes contained 150 mM ferricyanide and 150 mM ferrocyanide and all other conditions were identical including the light intensity of 350 mW at the sample. The $N_2$ purging was performed for 20 min before the photoelectrochemical measurement.

This photo-damage effect may also be counteracted by replacing photo-degraded chromophores with fresh porphyrins. In Figure 4.11, we show a series of optical absorption spectra and corresponding photocurrents recorded during the regeneration process. Initially, as shown in both Figure 4.11a and b, a DNA-coated SWCNT film (black line and bar) was characterized with no GaPP Soret signature and minimal current

signals under illumination. This film was then incubated with a GaPP-containing solution to allow the DNA strands to interact with GaPP molecules, forming the light-harvesting complexes. The donor-acceptor system demonstrates a strong Soret feature and photocurrent (shown in red in Figure 4.11).

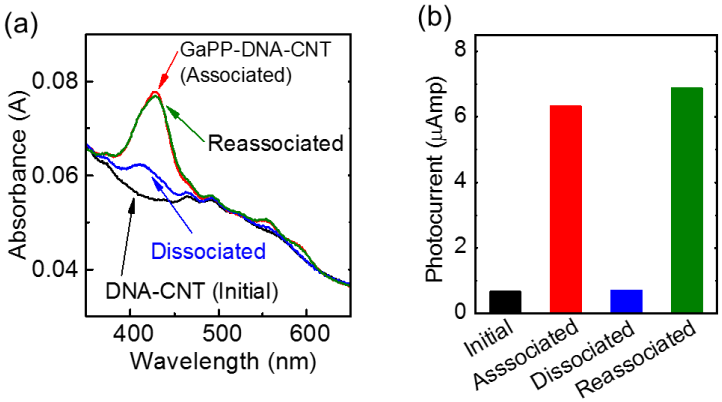


Figure 4.11. Absorption Spectra (a) and Corresponding Photocurrents (b) During the Sequential Regeneration Process: (i) Initial DNA-SWCNT Film with No GaPP (black), (ii) The DNA-SWCNT Film after Association with GaPP (red), (iii) The GaPP-DNA-SWCNT Film After GaPP Dissociation (Blue), And (iv) the GaPP-DNA-SWCNT Film After Re-association with GaPP (Green).

Then, we submerged the complex film in the 30 wt. % hydrogen peroxide solution for 1 hour to displace GaPP molecules. For the porphyrin dissociation, $H_2O_2$-induced oxidation of GaPP results in the destruction of porphyrin rings and/or dissociation from the DNA strands.[145, 146] The hydrogen peroxide based treatment is found to be effective at removing the porphyrins, while carbon nanotubes were well retained on the ITO, as they show no apparent changes in their optical absorption. After the GaPP removal, the film may have some porphyrin residue as seen in absorption, but its contribution to photocurrents was trivial (shown in blue in Figure 4.11). Finally, the film was re-

functionalized with fresh donor chromophores by re-association with porphyrins in a new solution. The absorption spectrum and photocurrent signal of the final GaPP-DNA-SWCNT complex film (shown in green in Figure 4.11) are nearly identical with those of the original GaPP-DNA-SWCNT film (shown in red).

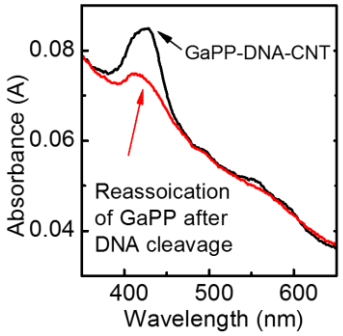


Figure 4.12. Absorption Spectra of GaPP-DNA-SWCNT Film before and after DNA Cleavage via the Fenton Reaction.

The results in Figure 4.12 also indicate that DNA-carbon nanotubes are intact after the hydrogen peroxide treatment. No significant effects on the carbon nanotubes are expected in the $H_2O_2$ treatment for 1 hour without temperature elevation,[147, 148] while their surface may be protonated at low pH and reversibly deprotonated at high pH.[149] To ascertain whether DNA strands remain intact after the treatment with 30 wt.% hydrogen peroxide solution, we performed a control experiment designed to damage DNA via the Fenton chemistry (Figure 4.12). Here, a GaPP-DNA-SWCNT film was exposed to 50 μM iron sulfate ($FeSO_4$) in 100 mM $H_2O_2$ solution for DNA cleavage after GaPP dissociation.[150] After the Fenton reaction, the film was washed thoroughly and the re-association with GaPP was carried out. With the DNA damaged, the Soret band of the GaPP-DNA-

SWCNT film was drastically lower at approximately 20 % of the intact GaPP-DNA-SWCNT film as the damaged oligonucleotides were unable to anchor the GaPP.

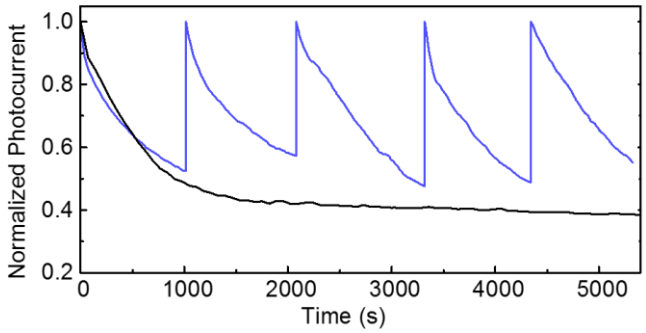


Figure 4.13. Photocurrent of the GaPP-DNA-SWCNT Complexes Produced through Four Regeneration Events (Blue) and That of the Complexes without Regeneration (Black).

Of considerable utility in this strategy is that the regeneration of donor chromophores can be repeated indefinitely. As proof-of-concept, we performed multiple regeneration cycles for a GaPP-DNA-SWCNT film, measured its photocurrent over time, and compared it with the film without porphyrin replacement. To facilitate photo-degradation of the donor chromophores, we used high light intensity at ~350 mW on the sample. As shown in Figure 4.13, the complex film without any regeneration demonstrates a continuous decay of photocurrent, quickly decreasing to 50 % of its initial photocurrent signal within the first thousand seconds (black curve). Another donor-acceptor complex film was regenerated after 1000 s by replacing the photo-damaged porphyrins through the $H_2O_2$ treatment and association with fresh porphyrins as described above. Such regeneration was repeated four times (blue curve). During the 90-min irradiation period, the overall photocurrent efficiency increased by 50% compared with no regeneration. We expect that for a 24-hour illumination period, the regenerated system would achieve 16 times more

photocurrent output than the film without replacement of photo-degraded chromophores. This novel approach may be potentially used for improving overall performance of donor-acceptor complexes and dramatically extending their light-harvesting service lifetime.

## 4.4 Summary

In this study, a novel strategy has been demonstrated, which counteracts the photo-degradation in all-synthetic molecular donor-acceptor complexes for light harvesting. Gallium protoporphyrins and semiconducting carbon nanotubes, the model donors and acceptors in this study, are assembled by using 30-mer oligonucleotides that have a strong affinity for the protoporphyrins. This complex demonstrates a consistent anodic photocurrent, originated from optical absorption of the porphyrin chromophores, followed by the excited-state electron transfer to carbon nanotubes on the ITO working electrode. The complex shows a superior ability for light harvesting and conversion compared to other samples without the porphyrins and based on other DNA sequences. Photo-induced degradation of the donor chromophores results in the decay of photocurrents over time. The regeneration of the complex film was demonstrated by sequentially dissociating the damaged donors from the complex and associating with fresh porphyrins, while the DNA-coated carbon nanotube acceptors were kept intact. The photocurrent recovered fully when the complex film was regenerated. Compared with the sample without regeneration, a 50 % increase in photocurrent was observed from four repeated regeneration cycles within a 90-min irradiation period. The bio-inspired

approach of dynamically replacing photo-degraded chromophores in the donor-acceptor complex could form a basis for solar energy harvesting systems with drastically improved overall performance and extended service lifetime.

# CHAPTER 5. PORPHYRIN-$MOS_2$ FOR IMPROVED LIGHT HARVESTING

## 5.1 Introduction

Chapter 1 discussed the advantages of $MoS_2$ nanolayers as light-harvesting materials as well as several related unaddressed issues. Chemically exfoliated $MoS_2$ nanolayers are mostly small flakes, which render them venerable for inefficient charge injection and high recombination due to the imperfection. This Chapter introduces an interfacial molecular engineering strategy to suppress charge recombination in large-area 2D $MoS_2$ films and thus enhance their photoelectrochemical properties. Here, 8 porphyrin species (with 3 ligand groups) were examined as interfacial molecules (Figure 5.1a): zinc(II)-, iron(III)-, gallium(III)-centered as well as metal-free protoporphyrin IX (ZnPP, FePP, GaPP, and $H_2$PP); metal-free and zinc(II)-centered tetra(N-methyl-4-pyridyl)porphines ($H_2$T4 and ZnT4); metal-free and zinc(II)-centered tetraphenylporphyrins ($H_2$TPP and ZnTPP).

The diversities in ligands and core metal ions of porphyrins provide distinct photophysical properties. For example, $H_2$T4 and ZnT4 have pyridium as the ligand group, rendering them cationic in aqueous electrolyte solution, whereas $H_2$TPP and ZnTPP should have net neutral charge due to the phenyl ligand.[151] With carboxylic moieties, ZnPP, FePP, GaPP and $H_2$PP are negatively charged in aqueous phase. Besides,

these porphyrins have a wide range of HOMO levels. By elucidating the relationship between porphyrin properties and photocurrents generated from porphyrin functionalized $MoS_2$ films, photoelectrochemical properties of nanolayered $MoS_2$ were investigated in this Chapter.

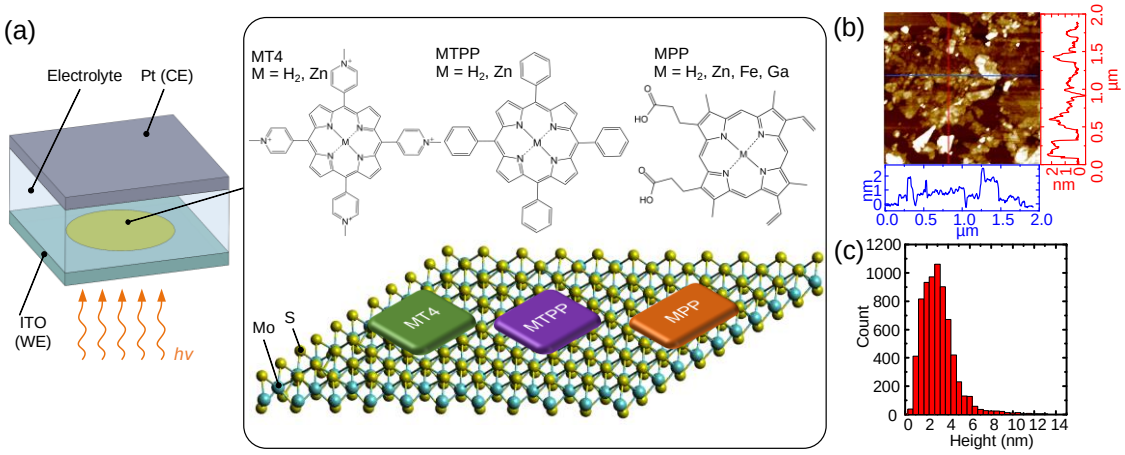


Figure 5.1. (a) Schematic of the $MoS_2$-Based Photoelectrochemical Cell. (b) Representative Atomic Force Microscopy (AFM) Image of a $MoS_2$ Film. (c) Histogram of the Film Thickness.

This Chapter also introduces a scalable manufacturing approach for large-area $MoS_2$ nanolayers. Chemical exfoliation of layered $MoS_2$ crystals was used to generate nanoflakes and subsequent solution phase deposition (similar to the method for SWCNT films in Chapters 3 and 4) was used to fabricate large-area 2D $MoS_2$ films. This approach could be adapted to manufacture large-area low-cost atomically thin light-harvesting nanolayers based on other TMDCs.

## 5.2 Materials and Methods

The detail synthesis and processing procedures for $MoS_2$ is discussed in Chapter 2, where the deposition methods of thin $MoS_2$ films are simultaneously mentioned. Liquid-exfoliated $MoS_2$ flakes were deposited and transferred onto the ITO/glass. Eight porphyrin molecules with 3 ligand groups were explored to enhance optoelectronic properties of $MoS_2$. The porphyrins include MT4 (tetra(N-methyl-4-pyridyl)porphines; M= $H_2$ and $Zn^{II}$), MTPP (tetraphenylporphyrins; M= $H_2$ and $Zn^{II}$), and MPP (protoporphyrin IX; M= $H_2$, $Zn^{II}$, $Fe^{III}$, and $Ga^{III}$). While MPP powders were dissolved in DMSO, T4 molecules were solubilized in DI water. Chloroform was used as the solvent of MTPPs. For porphyrin adsorption on $MoS_2$ nanolayers, the TMDC films were placed in 10 μM of each porphyrin solution for 15 min. The $MoS_2$ films were then rinsed with respective solvents to remove weakly bound porphyrins and characterized with atomic force microscopy (AFM), confocal Raman scattering measurement, and photoelectrochemistry.

For each film, ~1.8 μg of $MoS_2$ flakes was deposited, while for spectrally resolved photocurrent measurement discussed in Figure 5.8b, a thicker film (~18 μg) was introduced due to the weaker monochrome light. Here, the absorption spectra of the $MoS_2$ films were examined on transparent ITO/glass slides. Photoluminescence, Raman, and AFM measurements were carried out with $MoS_2$ films deposited on silicon wafers.

In this chapter, the AFM imaging was performed in air. Figure 5.1b shows an atomic AFM image of a typical deposited $MoS_2$ film with two height profiles along red and blue

lines. In Figure 5.1c, a statistical distribution of 3 random areas from 3 different films, showing an average thickness of about 2.8 nm or 5-6 $MoS_2$ layers over ~1 $cm^2$.

With Raman spectroscope, photoluminescence spectra of both $MoS_2$ films and porphyrins were obtained. The sample was irradiated by a HeNe laser (633 nm), and the 2D photoluminescence contours were created based on the photoluminescence at 660 nm, where is about the center of direct band gap of $MoS_2$.

Photoelectrochemical experiments were performed with same experiment setup as used in Chapter 4. In additions, one experiment involved applying bias-voltage in the cell. An Ag wire was served as the reference electrode. The spectrally-resolved photocurrent measurements were carried out with with an Oriel 1/8 m monochromator with 360 nm blaze grating. 10 mM Asc in DI water was the redox couple for all photoelectrochemical measurements.

## 5.3 Results and Discussion

### 5.3.1 Optical Experiments

The optical signatures of $MoS_2$, including absorption, photoluminescence and Raman, were examined before and after porphyrin functionalization. Lithium intercalation process converted original 2H semiconducting $MoS_2$ flakes to 1T metallic phase which remained after the deposition.[81] Thus, the $MoS_2$ films show no distinct excitonic band structures in their absorption spectrum (in Figure 5.2a).[81] After thermal annealing at 280

°C, 1T phase $MoS_2$ is converted to 2H semiconductor, as evidenced by distinct features in the absorption. Here, A and B indicate interband excitonic transitions at the K point of Brillouin zone, which locate at approximately 660 nm (1.88 eV) and 612 nm (2.03 eV), while the prominent bands are at ~430 nm.[58, 152, 153]

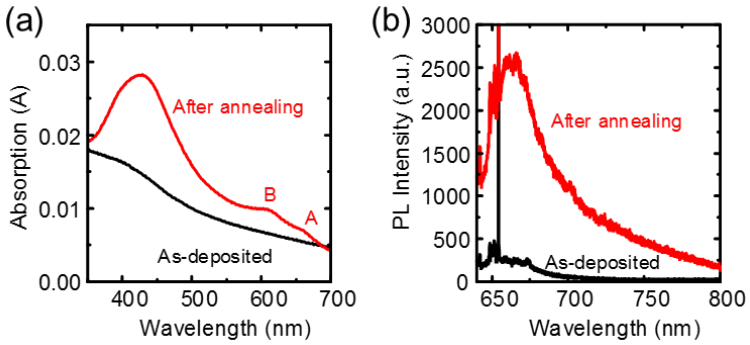


Figure 5.2. (a) Absorption Spectra and (b) Photoluminescence Spectra of $MoS_2$ Film before and after Thermal Annealing.

Along with the changes in the absorption spectra, thermal annealing effects can be observed in the photoluminescence spectra of the $MoS_2$ film in Figure 5.2b. No photoluminescence emission is observed in metallic 1T phase. Annealing at high temperature recovers original 2H phase and reduces crystal defects, rendering strong emission.[81] We did not observe the transition of exciton B at approximately 620 nm because of the 633 nm HeNe laser for photo-excitation in our Raman microscope.[59] A sharp peak in Figure 5.2b is observed at ~654 nm attributed to Raman signals from the silicon substrate(~520 $cm^{-1}$), and the less prominent peaks from 648 to 650 nm (from 380 to 405 $cm^{-1}$) are the Raman signatures of $MoS_2$ crystals.[154]

Absorption and photoluminescence signatures of $MoS_2$ interacting with porphyrins are demonstrated in Figure 5.3. Figure 5.3a presents the absorption spectra of the $MoS_2$ film before and after ZnT4 porphyrin functionalization. The $MoS_2$-porphyrin and the pristine film share the same absorption features with a minor difference near the Soret band of ZnT4 at ~450 nm.[155] The weak Soret and Q-band indicate very thin layer of porphyrins adsorbed on the $MoS_2$ surface.

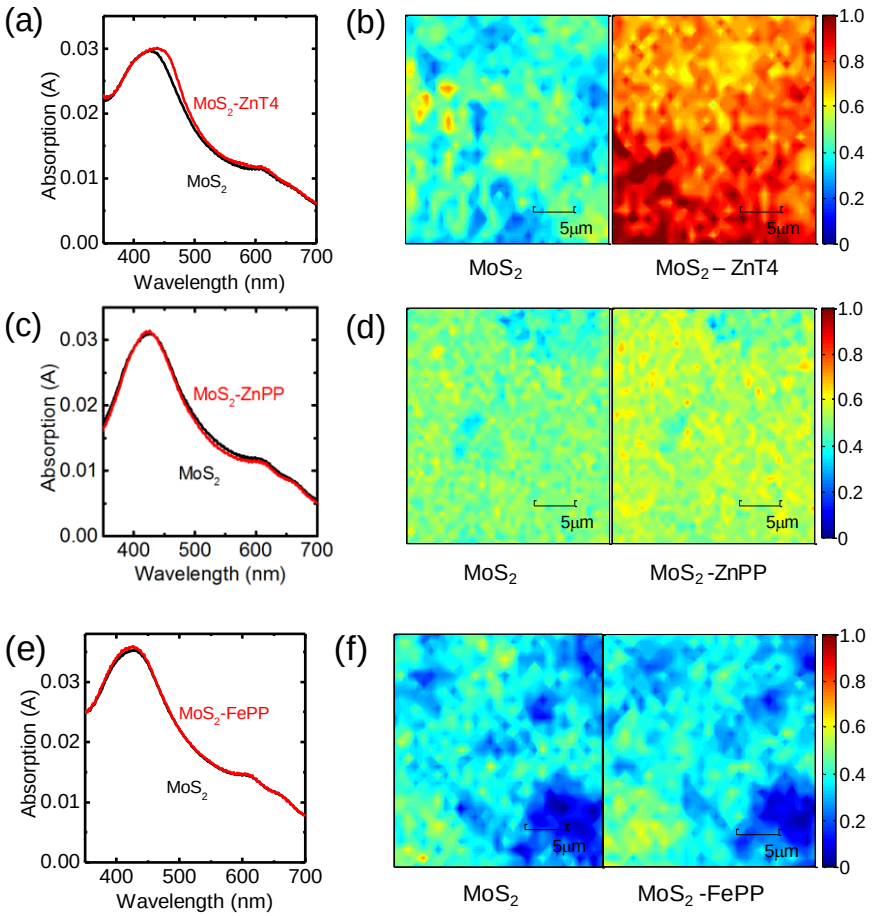


Figure 5.3. (a)(c)(e)(g) Absorption Spectra of the $MoS_2$ Film before and after ZnT4, ZnPP, FePP and ZnTPP Functionalization, Respectively. (b)(d)(f)(h) Raster-Scanned 2D Photoluminescence Map of the $MoS_2$ Film before (Left) and after (Right) after ZnT4, ZnPP, FePP and ZnTPP Functionalization.

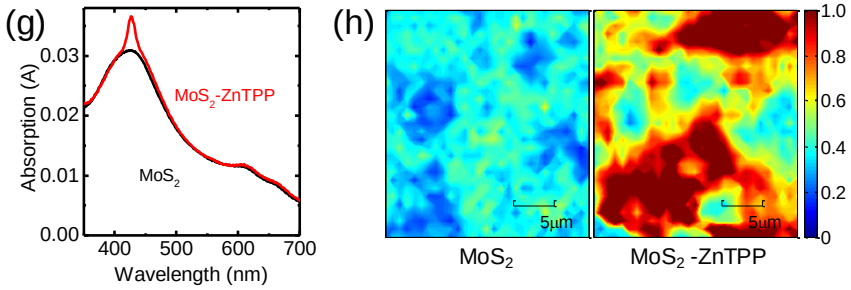


Figure 5.3. Continued.

To confirm the attachment of porphyrins, we monitored emission from an area (20 μm × 20 μm) of the $MoS_2$ film before and after ZnT4 adsorption. We reconstructed the spatially resolved emission contour of the pristine $MoS_2$ and ZnT4-MoS2 films (Figure 5.3b) based on the emission intensity measured at 660 nm. After ZnT4 functionalization, there is drastic increase in the emission across the entire area. As shown in Figure 5.4a, the new emerged emission signal is from ZnT4 upon being excited at 660 nm, which is the Q band region of ZnT4 (Figure 5.4b). From this observation, we conclude that ZnT4 porphyrins adsorb on $MoS_2$ films.

We observed similar adsorption behaviors with other porphyrin species including ZnPP and ZnTPP in Figure 5.3. While there are no significant differences in the absorption spectra before and after porphyrin adsorption, strong porphyrin emission can be observed compared with pristine $MoS_2$ films. Similar to ZnT4, as shown in Figure 5.4, both ZnPP and ZnTPP demonstrate strong photoluminescence signatures under 660 nm excitation, indicating that the emission increases are attributed to porphyrin functionalization.

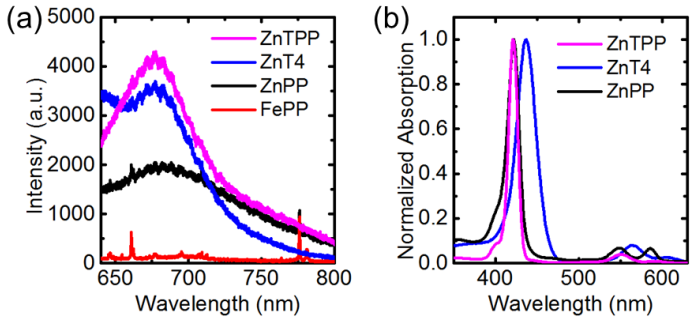


Figure 5.4. (a) Emission Spectra of ZnTPP in Chloroform, ZnT4 in Water, ZnPP and FePP in DMSO under 633 nm Excitation.

As shown in Figure 5.3e and f, there was no detectable difference between the pristine $MoS_2$ and FePP-adsorbed film due to the lack of emission from FePP (see Figure 5.4a). This is because iron-centered porphyrins demonstrates prominent nonradiative decay due to effective the d-orbital quenching.[156]

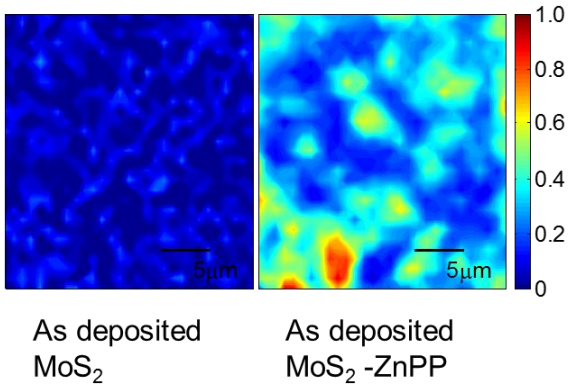


Figure 5.5. Raster-Scanned 2D Photoluminescence Maps of an as-Deposited (without Thermal Annealing) $MoS_2$ Nanolayers before (Left) and after (Right) ZnPP Adsorption.

To further verify the porphyrin adsorption on $MoS_2$ films, we recorded the spatially resolved photoluminescence contour of the as-deposited $MoS_2$ film (no annealing) with and without ZnPP. The un-annealed sample dominated by metallic 1T phase $MoS_2$ shows

no emission (Figure 5.2a), whereas clear emission signatures from the ZnPP functionalized $MoS_2$ un-annealed film demonstrate porphyrin attachment (Figure 5.5). All these results strongly suggest the adsorption of porphyrin molecules on $MoS_2$ films.

### 5.3.2 Photoelectrochemical Analyses

Figure 5.6 presents photocurrents of the $MoS_2$ film before and after thermal annealing along with un-exfoliated bulk $MoS_2$ sample. The chemically exfoliated $MoS_2$ flakes were deposited to form a large-area film on an ITO substrate, which should be in 1T metallic phase. In contrast, the bulk $MoS_2$ powder was briefly sonicated and deposited onto an ITO. Thus, the bulk $MoS_2$ sample retains its original semiconducting 2H phase. Anodic photocurrents were recorded from all $MoS_2$ films under visible light illumination. Photo-excited electrons were collected at the working electrode, while the holes are reduced through oxidation of the redox couple, Asc/DAsc. Then, the oxidized DAsc converts to Asc at the counter electrode (Pt cathode) via reduction by external electron flow, completing an electrical circuit loop.

As shown in Figure 5.6, approximately 120 nAmp photocurrents were obtained from the annealed $MoS_2$ under light irradiation, whereas bulk $MoS_2$ generated much weaker photocurrents of ~10 nAmp. The as-deposited metallic 1T phase $MoS_2$ film produced similar photocurrents of ~10 nAmp.[59, 73, 157]

Photocurrents of porphyrin functionalized $MoS_2$ are shown in Figure 5.7. In Figure 5.7a, photocurrents from a $MoS_2$ film before and after ZnPP functionalization are presented under 400-700 nm illumination. The photocurrents of the $MoS_2$-ZnPP film demonstrate almost one order of magnitude increase from the pristine film (from ~140 nAmp to ~1.1 μAmp).

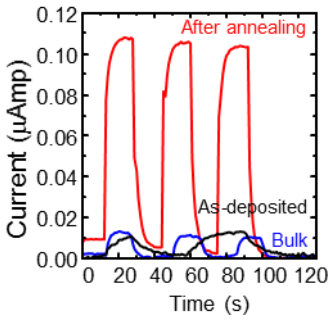


Figure 5.6. Photocurrents Generated from the Chemically Exfoliated Solution-Processed $MoS_2$ Film before (Black) and after (Red) Thermal Annealing.

To investigate the origination of the photocurrents, photo-absorption of pristine $MoS_2$ film is compared with spectrally resolved photocurrents (Figure 5.7b). The photocurrents of pristine $MoS_2$ and ZnPP functionalized $MoS_2$ films were recorded under irradiation from 350 to 800 nm with a 25 nm increment. As discussed in Materials and Methods Section of this Chapter, the annealed $MoS_2$ film (~18 μg) in this measurement is 10 times thicker than other $MoS_2$ samples (~1.8 μg). Due to a dramatic the light intensity decrease after the monochromator, we employed a larger amount of $MoS_2$ to acquire adequate photocurrents.

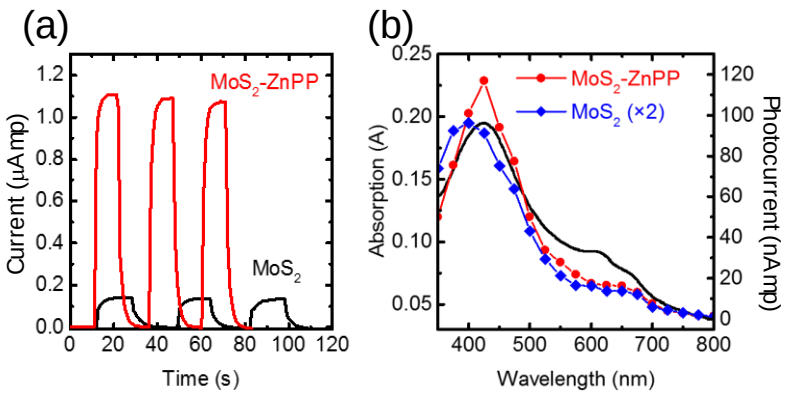


Figure 5.7. (a) Photocurrent Measurements of the $MoS_2$ Nanolayers with and without ZnPP Attachment. (b) Action Spectra of the $MoS_2$ Film before (Blue) and after (Red) Attachment of ZnPP along with Optical Absorption of Annealed Pristine Film.

Here, the spectrally resolved photocurrents from annealed $MoS_2$ and $MoS_2$-ZnPP films follow the absorption spectrum. The photocurrents of $MoS_2$-ZnPP are twice larger than those of the pristine film, displaying ~1% IPCE at 425 nm.

Important insights can be obtained from the action spectra (Figure 5.7). The photocurrents generated from 550 to 700 nm match the A and B excitonic bands, and the photocurrents from 350 to 500 nm closely follow the C excitonic signature. Interestingly, a small photocurrent signature at ~425 nm is observed, corresponding to the Soret band of functionalized ZnPP molecules. This observation suggests a charge transfer process from the photoexcited ZnPP to the conduction band of $MoS_2$. It should be noted that unlike this ZnPP-MoS2 result, the photocurrents the porphyrin-carbon nanotube hybrids in Chapters 3 and 4 match the absorption of the porphyrins instead of carbon nanotubes. Therefore, we conclude that the photocurrents are generated from the photoexcited $MoS_2$, while the functionalized porphyrins can serve as photo-sensitizers in a very modest way.

For the most part, porphyrins play an important role in separating photoexcited charges and suppressing their recombination in $MoS_2$.

Finally, the results in Figure 5.7 suggest that the photocurrents are not closely related to the thickness of $MoS_2$ films. The thin $MoS_2$-ZnPP film demonstrated nearly a 10-fold enhancement with porphyrins (Figure 5.7a), whereas the thicker film in Figure 5.7b produced merely a 2-fold increase over the annealed $MoS_2$ film. For the thicker film, the charge transfer distance is greater so that there is a greater possibility of recombination.

### 5.3.3 Bias Voltage Measurements

In order to better understand the change transfer mechanism, we applied external bias voltages on $MoS_2$ and $MoS_2$-ZnPP films and examined the corresponding photocurrents. As seen in Figure 5.8a and c, the short-circuit photocurrents from the annealed, pristine $MoS_2$ film are almost identical (~110 nAmp) as those in Figure 5.6 and Figure 5.7a. Upon applying a positive voltage across between the $MoS_2$/ITO and the counter electrode, photocurrents and dark currents (*i.e.* baseline or initial stable currents) increase simultaneously.

The photocurrents increased from ~110 to ~200 nAmp, while the baseline currents increased from ~0 to ~450 nAmp at 50 mV. With increasing bias voltage, both photocurrents and dark currents were gradually elevated. At 200 mV, the photocurrents from the annealed $MoS_2$ film were approximately 300 nAmp which is about three times

larger than that of zero bias voltage. A reverse trend was observed when negative bias voltages were applied. At -50 mV, the photocurrents were undetectable, while the baseline became approximately -300 nAmp. Negative bias voltage gradually promoted negative photocurrents, which implies that photoexcited electrons were drifted toward the counter electrode rather than the working electrode. The negative photocurrents reached about -250 nAmp at the bias voltage of -200 mV.

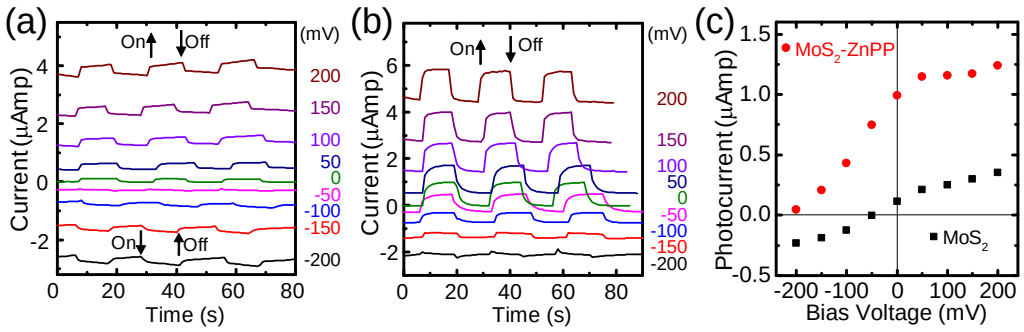


Figure 5.8. Current Profiles of (a) Annealed, Pristine $MoS_2$ and (b) $MoS_2$-ZnPP Films under Bias Voltage and Photo-Irradiation. (c) Extracted Photocurrents from (a) and (b).

The $MoS_2$-ZnPP film displayed similar phenomena with the pristine $MoS_2$ under bias voltages (Figure 5.8b and c). At 50 mV, the photocurrent from the ZnPP-$MoS_2$ film increased from ~1 to ~1.2 μAmp, while the baseline ascends from ~0 to ~0.55 μAmp. Both photocurrents and dark currents gradually increased with increasing bias voltage and reached ~1.4 and ~4.5 μAmp at 200 mV, respectively. Similar to the pristine $MoS_2$, the photocurrents monotonically decreased from ~1 to ~0 μAmp when negative bias voltage was changed from 0 to -200 mV. One would expect negative photocurrents at further negative bias voltages. The photocurrent mechanisms with bias voltage are discussed in the following section.

### 5.3.4 Charge Transfer Mechanisms between $MoS_2$ and Porphyrins

To elucidate the photocurrent behaviors of $MoS_2$ films with and without porphyrins as well as with bias voltages, we first define the photocurrent increment or $(I - I_o)/ I_o$ where I indicates the photocurrents of $MoS_2$ with porphyrins and $I_o$ is the photocurrents of the pristine film. We then complied the photocurrent enhancements of all 8 porphyrin species versus the HOMO level of the porphyrins against vacuum (Figure 5.9).

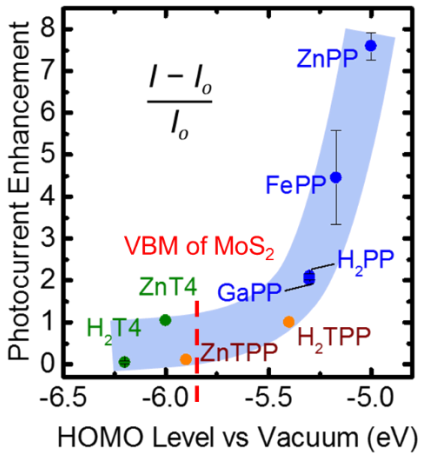


Figure 5.9. Photocurrent Enhancement of $MoS_2$ Films as a Function of Porphyrin Species.

The HOMO level values were extracted from several previous reports in the literature.[158-163] It is evident that the photocurrent enhancements are strongly correlated with the HOMO levels of porphyrins. The blue shade was inserted to guide the eye in the figure, and a curve fitting was performed which is discussed later. All the photocurrent measurement results to construct Figure 5.9 are presented in Figure 5.10

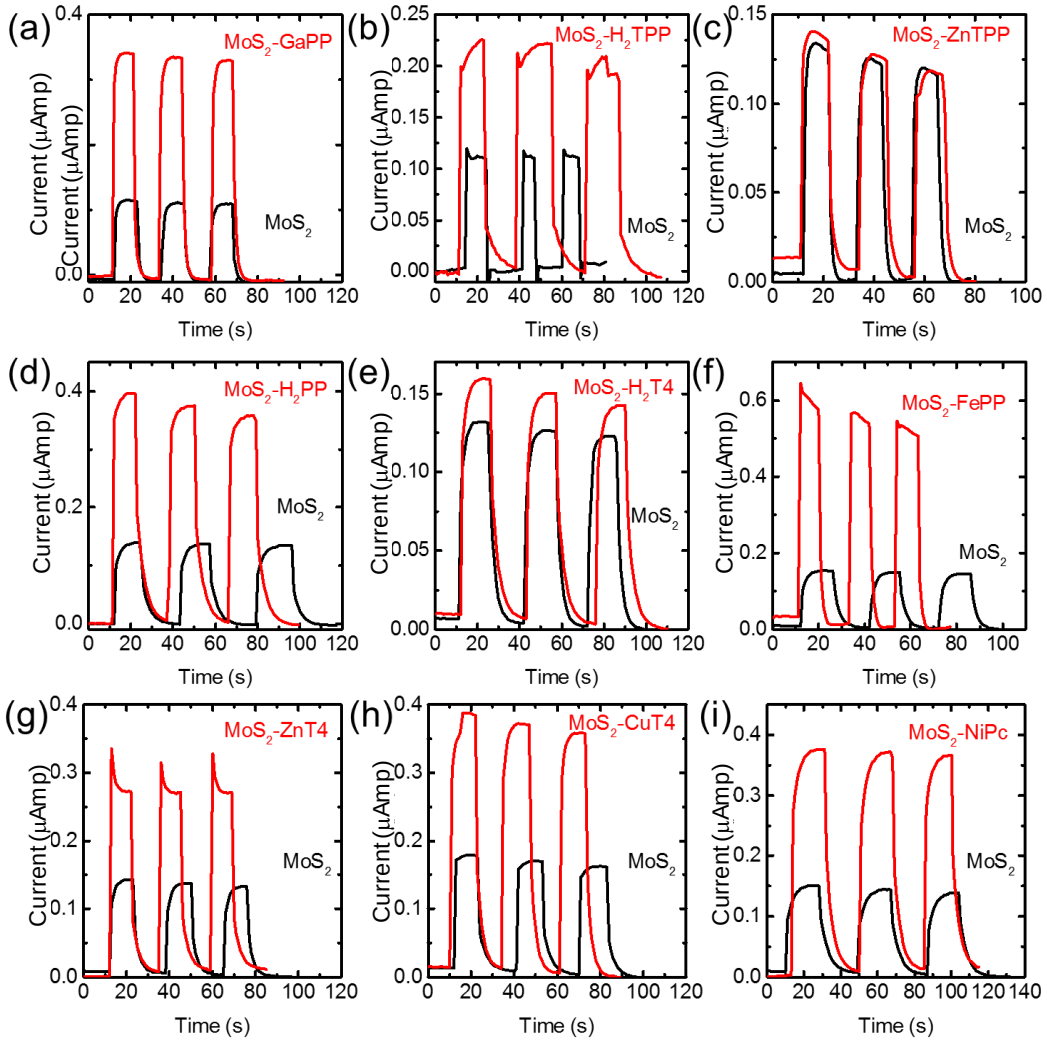


Figure 5.10. Photocurrent Measurements of $MoS_2$ Films with (Red) and without (Black) Porphyrins or Phthalocyanine.

In Figure 5.9, the photocurrents of the $MoS_2$ films strongly depends on the porphyrin species as they increase with higher HOMO level versus vacuum. For example, ZnPP demonstrates nearly an order of magnitude increase in photocurrents compared with the pristine $MoS_2$ film, whereas no significant photocurrent changes are observed after functionalization with $H_2T4$ and ZnTPP. The photocurrents of the films with ZnT4 and $H_2TPP$ molecules exhibit a 2-fold increase. The $MoS_2$ films functionalized with GaPP

and $H_2PP$ show almost the identical photocurrent enhancement, while FePP elevates the photocurrents of $MoS_2$ films by about five times. Given that ZnTPP and ZnPP show completely opposite photocurrent behaviors, it is clear that the metal cations at the porphyrin cores alone cannot explain the dependence of $MoS_2$ photocurrents on porphyrin species.

The three ligands (T4, TPP, and PP) of porphyrins may be taken into consideration for evaluating the photocurrent enhancement behaviors. T4s have four pyridium ligands that are positive charged in aqueous solution. For TPPs, a net neutral charge is provided from their phenyl functioning groups.[151] Negatively charge can be expected from carboxylic moieties of PPs in aqueous solution.

Here, both T4s and TPPs demonstrate relatively smaller photocurrent increases than that from PPs. The photocurrent enhancements of PPs show large variations within a single ligand group; for instance, 8-time increase for ZnPP and only 3-time enhancement for $H_2PP$.

The enhancement of the photocurrents is directly correlated with relative magnitude between the HOMO level of each porphyrin and valence band maximum (VBM) of $MoS_2$. The VBM of monolayer $MoS_2$ is obtained from numerical calculations in previous reports in the literature.[164] This correlation can be described in Equation (6).

$$\frac{I - I_0}{I_0} = 0.22 + 0.14\, e^{\frac{HOMO-VBM}{0.23}} \quad (6)$$

The exponential fitting well describes the interplay of photocurrent enhancements with the energy difference between the HOMO of porphyrin and the VBM of $MoS_2$.

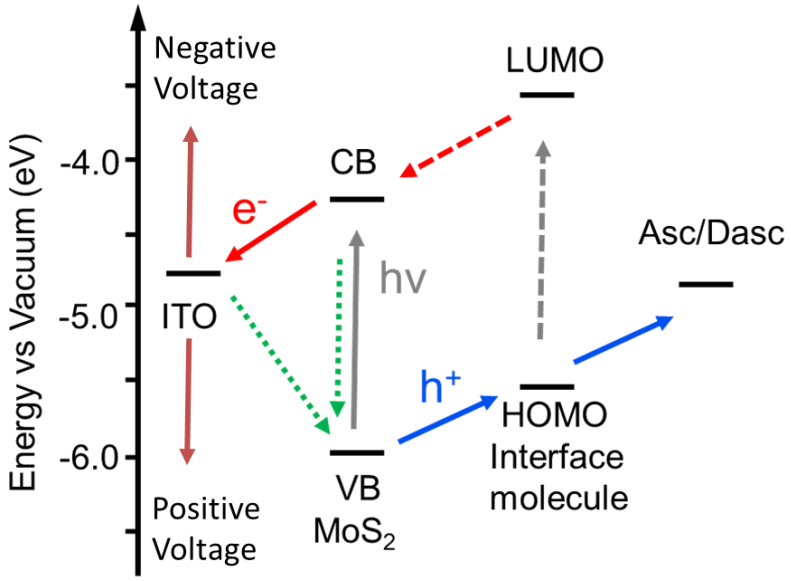


Figure 5.11. Charge Transfer Pathways for Photocurrent Enhancement in $MoS_2$ Films by Surface Engineering with Porphyrins.

To elucidate this correlation, we propose mechanisms for charge transfer processes in the $MoS_2$-porphyrin systems. Figure 5.11, red lines indicate electron injection pathways, while blue arrows represent hole transfer. Grey lines illustrate the photoexcitation, and green lines suggest prominent charge recombination. After photo-excitation, electrons in the $MoS_2$ sample are promoted into the conduction band (CB) which are ultimately collected at the ITO.[165] The holes left in $MoS_2$ can be transferred to the redox couple in electrolyte solution whose redox potential lies higher than the VBM of $MoS_2$.[166] The

oxidized products, DAsc, diffuse towards the Pt electrode and are reverted to Asc, thus generating photocurrents.

Several other processes may compete with the proposed charge transfer mechanism. For example, the electrons in the excited state can experience radiative or nonradiative quenching to the valence band (VB). There could also be recombination between the holes in the $MoS_2$ VB and electrons in the ITO. All these processes suppress the photocurrent outputs.

Porphyrin adsorption may reduce the charge recombination processes in the $MoS_2$ nanolayers, thus promoting current generation. For porphyrins that have higher HOMO levels than the VBM of $MoS_2$, the holes generated after photo-excitation may be transported to the attached molecules, thus minimizing the back reaction and recombination. The suppression of charge transfer with surface functionalized porphyrins is more prominent, compared to the pristine $MoS_2$ that simply depend on slow diffusion of the redox couple.

In above scheme, the charge transfer would be more efficient with porphyrins that have higher HOMO levels (*e.g.*, ZnPP and FePP), resulting in tremendous current increases. However, the porphyrins with similar or lower HOMO levels compared with the VBM of $MoS_2$ (such as $H_2T4$ and ZnTPP) are expected to make insignificant impacts on the photocurrent enhancement. Thus, the hole transfer from $MoS_2$ to $H_2T4$ and ZnTPP should be minimal or unfavorable. Thus, the photocurrent improvements by $H_2T4$ and ZnTPP

are negligible, which is evident in the photoelectrochemical experiments. It is worth noting that the CBM and VBM levels of $MoS_2$ in Figure 5.9 are reported for monolayer $MoS_2$, which are different from those of few-layer $MoS_2$ flakes, considering that band energies of $MoS_2$ are strongly dependent on the layer numbers.[164, 167]

Along with the porphyrins shown in Figure 5.9, there are two additional chromophore molecules tested for improving photocurrents in $MoS_2$: CuT4 and nickel tetrasulfonated phthalocyanine (NiPc), as shown in Figure 5.10h and i, respectively. However, the results are not incorporated in Figure 5.9 due to the lack of information about their HOMO/LUMO levels.

Besides the photocurrent enhancement from $MoS_2$, it is noted that there is a minor portion of photocurrent increment generated from the porphyrin molecules. As we learned from Figure 5.7b, the porphyrins such as ZnPP can modestly contribute to the photocurrents as photosensitizers, which inject electrons into $MoS_2$ (indicated by red dashed line in Figure 5.11) after photoexcitation.

The bias voltage effects may be also explained by the aforementioned mechanism. Upon applying a positive bias voltage, the work function of the ITO may be shifted downward against the vacuum, causing a larger energy difference between the working function of ITO and the CBM of $MoS_2$. As a result, the photoexcited electrons from $MoS_2$ or $MoS_2$-porphyrin films have higher chances to transfer to the ITO due to a larger driving energy for electron injection and suppressed recombination. Thus, higher anodic photocurrents

are observed with positive bias voltage applied. On the contrary, negative voltages reduce the work function of ITO, therefore decreasing the driving force for photoexcited electron transfer to the ITO. Continous increase of negative bias voltage leads to a point where the ITO work function lies above the CBM of $MoS_2$, resulting in inverted photocurrents. Futhermore, larger negative bias voltages end up as more prominent negative (i.e. cathodic) photocurrents.

The impact of porphyrin on the reversal of the photocurrent direction is evident (Figure 5.8c). The inflection point transitions from roughly -50 mV with the $MoS_2$ film to about -200 mV for the $MoS_2$-ZnPP sample. The shift of the inflection points by ~150 mV is attributed to ZnPP. However, the gap between the work function of ITO and the $MoS_2$ CBM is roughly 500 mV as shown in Figure 5.12, which is larger than the energy difference between two inflection points. This discrepancy may be explaind considering the actual gap between CBM and VBM of few-layer-thick $MoS_2$ films should be significantly smaller. This implies that the energy difference between ITO and CBM of $MoS_2$ may be much less than 500 mV. Overall, these results verify the effectiveness of interfacial porphyrin molecules on modulating $MoS_2$ properties .

## 5.4 Summary

In this Chapter, we sucessfully manufactured large-area ultrathin films from chemically exfoliated $MoS_2$ layers. Here, 8 porphyrin species were explored for modulating the photoelectrochemical properties of the $MoS_2$ films. We observed nearly an order of

magnitude photocurrent enhancement from the ZnPP-functionalized $MoS_2$ compared with the pristine film. The increase of photocurrents are strongly correlated to the HOMO energies of the functionalized porphyrins. A porphryin with a higher HOMO level displayed a greater photocurrent enhancement from the $MoS_2$ film. We attributed the phenomena to the interfacial porphyrins that significantly reduced charge recombination within the system, and thereby, enhanced the photocurrents. We also demonstrated that porphyrin functionalization effectively modulated the reversal potentials of the photocurrents (e.g. from anodic to cathodic photocurrents). Our results and explanations provide important insights about the fundamental properties of 2D $MoS_2$ nanolayers interacting with porphyrins or other organic compounds, which should form a basis for utilizing 2D TMDCs in light-harvesting applications.

# CHAPTER 6. CONCLUSIONS

## 6.1 Summary

This thesis has investigated two promising semiconducting nanomaterials integrated with porphyrin chromophores for fundamental light-harvesting studies. Novel donor-acceptor systems were designed and constructed using SWCNTs and $MoS_2$ nanolayers, and studied for the photophysical and photoelectrochemical properties.

Carbon nanotubes are conceptually rolled-up graphene sheets and are synthesized chemically as a mixture of various species, which may be either semiconducting or metallic. With the advances of SWCNT separating techniques, high-purity semiconducting SWCNTs are now available which are highly desirable as charge acceptors in a light-harvesting complex due to their ability for charge separation and high carrier mobility. To preserve the excellent physical properties of pristine SWCNTs, noncovalent chemistry may be used, which can also solubilize them in aqueous solution. In this thesis, synthetic DNA oligonucleotides were used for dual purposes of (1) noncovalently functionalizing SWCNTs and (2) recognizing target donor chromophores.

In Chapter 3, DNA-SWCNT hybrids were designed and functionalized with various porphyrin species. The DNA-assembled SWCNT-porphyrin nanohybrids were deposited

to construct large-area thin films through membrane filtration. The nanohybrid films were demonstrated for photoelectrochemical conversion. The magnitude and direction of measured photocurrents were strongly correlated with electrolyte conditions. To elucidate the photoconversion processes in the nanohybrids, several porphyrin species were examined using steady state and transient measurements of their fluorescence and phosphorescence signatures. We found that the electrons after photo-excitation at the Soret band of the porphyrins rapidly relax to the lower-lying singlet state, and are transferred to carbon nanotubes and converted to photocurrents. Once electrons undergo an intersystem crossing to a triplet state, they return to the ground state by either emitting phosphorescence or interacting with molecular oxygen in the solution. However, CuT4 experiences different relaxation pathways as the excited electrons efficiently transition to a triplet state. As a result, all nanohybrids demonstrated similar photoconversion efficiency of ~1.5% under the experimental conditions with the exception of CuT4-based hybrids.

Chapter 4 introduced a new concept of regenerative light harvesting to counteract the photo-induced degradation of donor molecules. Using DNA aptamers that selectively recognize protoporphyrins by forming a G-quadruplex structure, we designed the SWCNT-DNA-GaPP hybrids capable of system regeneration. We demonstrated that photo-damaged porphyrins could be removed from DNA-SWCNTs by modulating the chemical environment, and fresh GaPP molecules were re-assembled to form fully functional photoelectrochemical nanohybrids. As photo-degrading nanohybrids were dynamically regenerated, the resulting photocurrents were fully recovered. This new

approach could be invaluable for improving overall light-harvesting efficiency and extending the service lifetime.

Nanolayered $MoS_2$, an emerging 2D material, shows promise in light harvesting. Chapter 5 addresses two critical issues in using $MoS_2$ nanolayers in photoelectrochemical conversion. First, we introduced a scalable, cost-effective manufacturing approach that includes chemical exfoliation of MoS2 flakes from bulk crystals and membrane filtration based deposition to form large-area $MoS_2$ films. Second, an interfacial engineering strategy was developed to mitigate charge recombination within MoS2 nanolayers due to the defects and small flake sizes. Eight molecules from three distinct porphyrin families were explored as interfacial molecules to suppress charge recombination and thus to increase photocurrents. A maximum 10-fold increase of photocurrents was observed from ZnPP-functionalized $MoS_2$ nanolayers. We found that the photocurrent enhancement is strongly correlated with the potential difference between the HOMO level of porphyrins and the valence band maximum of $MoS_2$.

Overall, the scientific insights and engineering approaches explored in this thesis will be useful in designing next-generation photovoltaic and photoelectrochemical cells. The proposed new concepts and potential solutions for the current issues could transform solar cells into the most powerful renewable energy method for our society.

## 6.2 Future Study

The new scientific knowledge and engineering breakthroughs in this thesis provide an inspiration for further investigation of light-harvesting materials and systems based on SWCNTs and $MoS_2$ nanolayers. Several directions for future studies are outlined below.

The electronic gap alignment of donors and acceptors may be explored within the porphyrin/SWCNT nanohybrid based solar cells. The tunability of porphyrin chromophores modulates the electronic energy levels based on their ligand groups and cation centers. Given the combinatorial library of ligands and metal-centers, it is possible to find a matching energy level between donors and acceptors, which can directly represent the driving force of charge transfer under illumination. This is also one of the research areas in DSSCs, where chromophores serve as charge donors. In parallel, SWCNTs, used as charge acceptors in our system, may vary in chirality and species, exhibiting various electronic band structures. They demonstrate not only two (semiconducting and metallic) electronic types, but also a wide range of bandgap and energy level indexed by chirality vector (n, m). Each charity leads to a unique Fermi level. It is possible to sort the SWCNTs by their species using density gradient ultracentrifugation and select a single chirality that has a favorable electronic energy level. From the combination of porphyrins and SWCNTs, we may explore and identify a matched electronic energy level between single SWCNT species and porphyrin chromophore. Such effort will form the basis to develop high-efficiency and environmental friendly photoelectrochemical energy conversion systems.

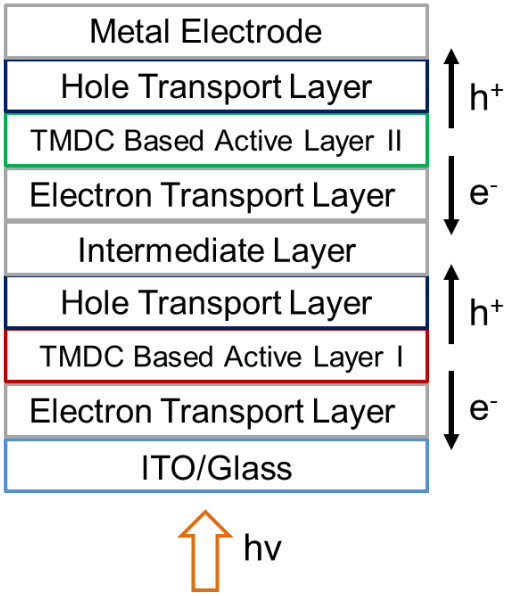


Figure 6.1. Schematic Diagram of Tandem TMDC Based Solid-State Light-Harvesting Devices.

Another important research direction is the scalable manufacturing and interfacial engineering of 2D TMDCs using porphyrins, aiming at rendering nanolayered TMDC a strong candidate for high-performance solid-state light-harvesting devices. Given the limited visible absorption by a single 2D TMDC layer, it is advantageous to design a tandem solid-state device using several nanolayered TMDCs. For example, $WS_2$ flakes have excitonic absorption peaks in purple (~ 450 nm), blue (~ 530 nm) and orange (~ 610 nm), while excitonic bands A and B of $MoSe_2$ monolayers are positioned in red (~ 708 and 810 nm).[168-170] By constructing tandem solar cells composed of multiple TMDCs nanolayers, it is possible to maximize the utilization of incident solar radiation. Therefore, future efforts may be focused on designing and constructing an efficient sub-cell for photo-excitation, charge separation and shuttling, as shown in Figure 6.1. We plan to tailor energy levels of electron and hole transport layers, as well as 2D TMDC

coated electrodes in order to provide effective pathways for photogenerated charges. Within the TMDC based photoactive layer, interfacial molecular engineering can enhance the performance, as shown in Chapter 5. By matching energy levels between TMDCs and porphyrins, it is possible to develop a photoactive layer with high internal quantum efficiency. In parallel, it is important to establish a strategy to assemble all components manufacturing all solid-state devices. For this purpose, we may apply sequential vacuum filtration depositions for photoactive and charge transport layers. Ultimately, our efforts could lead to cost-effective light-harvesting devices capable of pan-spectral light absorption and high-efficiency energy conversion.

# LIST OF REFERENCES

# LIST OF REFERENCES


[1] M. I. Hoffert, K. Caldeira, A. K. Jain, E. F. Haites, L. D. D. Harvey, S. D. Potter, M. E. Schlesinger, S. H. Schneider, R. G. Watts, T. M. L. Wigley, D. J. Wuebbles, *Nature* **1998**, 395, 881.

[2] M. I. Hoffert, K. Caldeira, G. Benford, D. R. Criswell, C. Green, H. Herzog, A. K. Jain, H. S. Kheshgi, K. S. Lackner, J. S. Lewis, H. D. Lightfoot, W. Manheimer, J. C. Mankins, M. E. Mauel, L. J. Perkins, M. E. Schlesinger, T. Volk, T. M. L. Wigley, *Science* **2002**, 298, 981.

[3] P. V. Kamat, *Journal of Physical Chemistry C* **2007**, 111, 2834.

[4] J. Tollefson, *Nature* **2011**, 473, 134.

[5] D. E. Carlson, C. R. Wronski, *Applied Physics Letters* **1976**, 28, 671.

[6] J. Britt, C. Ferekides, *Applied Physics Letters* **1993**, 62, 2851.

[7] I. Repins, M. A. Contreras, B. Egaas, C. DeHart, J. Scharf, C. L. Perkins, B. To, R. Noufi, *Progress in Photovoltaics* **2008**, 16, 235.

[8] A. Hagfeldt, G. Boschloo, L. C. Sun, L. Kloo, H. Pettersson, *Chemical Reviews* **2010**, 110, 6595.

[9] M. Gratzel, *Inorganic Chemistry* **2005**, 44, 6841.

[10] M. Gratzel, *Nature* **2001**, 414, 338.

[11] B. Oregan, M. Gratzel, *Nature* **1991**, 353, 737.

[12] B. C. Thompson, J. M. J. Frechet, *Angewandte Chemie-International Edition* **2008**, 47, 58.

[13] H. Hoppe, N. S. Sariciftci, in *Photoresponsive Polymers Ii*, Vol. 214, Springer-Verlag Berlin, Berlin 2008, 1.

[14] A. C. Mayer, S. R. Scully, B. E. Hardin, M. W. Rowell, M. D. McGehee, *Materials Today* **2007**, 10, 28.

[15] C. J. Brabec, S. Gowrisanker, J. J. M. Halls, D. Laird, S. J. Jia, S. P. Williams, *Advanced Materials* **2010**, 22, 3839.

[16] K. H. Yu, J. H. Chen, *Nanoscale Research Letters* **2009**, 4, 1.

[17] J. H. Bang, P. V. Kamat, *Acs Nano* **2009**, 3, 1467.

[18] T. Umeyama, H. Imahori, *Energy & Environmental Science* **2008**, 1, 120.

[19] J. M. Kroon, N. J. Bakker, H. J. P. Smit, P. Liska, K. R. Thampi, P. Wang, S. M. Zakeeruddin, M. Gratzel, A. Hinsch, S. Hore, U. Wurfel, R. Sastrawan, J. R. Durrant, E. Palomares, H. Pettersson, T. Gruszecki, J. Walter, K. Skupien, G. E. Tulloch, *Progress in Photovoltaics* **2007**, 15, 1.

[20] R. H. Baughman, A. A. Zakhidov, W. A. de Heer, *Science* **2002**, 297, 787.

[21] T. W. Ebbesen, H. J. Lezec, H. Hiura, J. W. Bennett, H. F. Ghaemi, T. Thio, *Nature* **1996**, 382, 54.

[22] T. Durkop, S. A. Getty, E. Cobas, M. S. Fuhrer, *Nano Letters* **2004**, 4, 35.

[23] L. B. Hu, D. S. Hecht, G. Gruner, *Chemical Reviews* **2010**, 110, 5790.

[24] R. Saito, G. Dresselhaus, M. S. Dresselhaus, World Scientific, 1998.

[25] R. Saito, M. Fujita, G. Dresselhaus, M. S. Dresselhaus, *Applied Physics Letters* **1992**, 60, 2204.

[26] E. T. Thostenson, Z. F. Ren, T. W. Chou, *Composites Science and Technology* **2001**, 61, 1899.

[27] X. M. Tu, M. Zheng, *Nano Research* **2008**, 1, 185.

[28] M. J. O'Connell, S. M. Bachilo, C. B. Huffman, V. C. Moore, M. S. Strano, E. H. Haroz, K. L. Rialon, P. J. Boul, W. H. Noon, C. Kittrell, J. P. Ma, R. H. Hauge, R. B. Weisman, R. E. Smalley, *Science* **2002**, 297, 593.

[29] S. M. Bachilo, M. S. Strano, C. Kittrell, R. H. Hauge, R. E. Smalley, R. B. Weisman, *Science* **2002**, 298, 2361.

[30] F. Wang, G. Dukovic, L. E. Brus, T. F. Heinz, *Science* **2005**, 308, 838.

[31] P. Avouris, Z. H. Chen, V. Perebeinos, *Nature Nanotechnology* **2007**, 2, 605.

[32] M. Cinke, J. Li, B. Chen, A. Cassell, L. Delzeit, J. Han, M. Meyyappan, *Chemical Physics Letters* **2002**, 365, 69.

[33] X. Peng, S. Wong, *Advanced Materials* **2009**, 21, 625.

[34] D. M. Guldi, *Physical Chemistry Chemical Physics* **2007**, 9, 1400.

[35] V. Sgobba, G. M. A. Rahman, D. M. Guldi, N. Jux, S. Campidelli, M. Prato, *Advanced Materials* **2006**, 18, 2264.

[36] M. Á. Herranz, N. Martín, S. Campidelli, M. Prato, G. Brehm, D. M. Guldi, *Angewandte Chemie* **2006**, 118, 4590.

[37] G. d. l. Torre, W. Blau, T. Torres, *Nanotechnology* **2003**, 14, 765.

[38] M. Alvaro, P. Atienzar, P. de la Cruz, J. L. Delgado, H. Garcia, F. Langa, *The Journal of Physical Chemistry B* **2004**, 108, 12691.

[39] M. Zheng, A. Jagota, E. D. Semke, B. A. Diner, R. S. McLean, S. R. Lustig, R. E. Richardson, N. G. Tassi, *Nature Materials* **2003**, 2, 338.

[40] M. H. Ham, J. H. Choi, A. A. Boghossian, E. S. Jeng, R. A. Graff, D. A. Heller, A. C. Chang, A. Mattis, T. H. Bayburt, Y. V. Grinkova, A. S. Zeiger, K. J. Van Vliet, E. K. Hobbie, S. G. Sligar, C. A. Wraight, M. S. Strano, *Nature Chemistry* **2010**, 2, 929.

[41] D. M. Guldi, G. Rahman, M. Prato, N. Jux, S. Qin, W. Ford, *Angewandte Chemie* **2005**, 117, 2051.

[42] V. Sgobba, G. A. Rahman, D. M. Guldi, N. Jux, S. Campidelli, M. Prato, *Advanced Materials* **2006**, 18, 2264.

[43] D. M. Guldi, G. Rahman, M. Prato, N. Jux, S. Qin, W. Ford, *Angewandte Chemie* **2005**, 117, 2051.

[44] P. Brown, K. Takechi, P. V. Kamat, *The Journal of Physical Chemistry C* **2008**, 112, 4776.

[45] F. D'Souza, S. K. Das, M. E. Zandler, A. S. D. Sandanayaka, O. Ito, *Journal of the American Chemical Society* **2011**, 133, 19922.

[46] T. Hasobe, S. Fukuzumi, P. V. Kamat, *Journal of Physical Chemistry B* **2006**, 110, 25477.

[47] D. M. Guldi, G. M. Rahman, F. Zerbetto, M. Prato, *Accounts of Chemical Research* **2005**, 38, 871.

[48] A. Hagfeldt, G. Boschloo, L. Sun, L. Kloo, H. Pettersson, *Chemical Reviews* **2010**, 110, 6595.

[49] E. Nyarko, N. Hanada, A. Habib, M. Tabata, *Inorganica Chimica Acta* **2004**, 357, 739.

[50] M. Gouterman, in *The Porphyrins*, (Ed: D. Dolphin), Academic Press, New York, U.S.A. 1978, 1.

[51] D. Eastwood, M. Gouterman, *Journal of Molecular Spectroscopy* **1970**, 35, 359.

[52] W. M. Campbell, A. K. Burrell, D. L. Officer, K. W. Jolley, *Coordination Chemistry Reviews* **2004**, 248, 1363.

[53] H. He, A. Gurung, L. Si, *Chemical Communications* **2012**, 48, 5910.

[54] E. Maligaspe, A. S. Sandanayaka, T. Hasobe, O. Ito, F. D'Souza, *Journal of the American Chemical Society* **2010**, 132, 8158.

[55] K. Kalyanasundaram, *Dye-sensitized Solar Cells*, EFPL Press, 2010.

[56] K. Kalyanasundaram, *Inorganic Chemistry* **1984**, 23, 2453.

[57] K. Kalyanasundaram, M. Neumann-Spallart, *Journal of Physical Chemistry* **1982**, 86, 5163.

[58] K. F. Mak, C. Lee, J. Hone, J. Shan, T. F. Heinz, *Physical Review Letters* **2010**, 105, 136805.

[59] A. Splendiani, L. Sun, Y. Zhang, T. Li, J. Kim, C.-Y. Chim, G. Galli, F. Wang, *Nano Letters* **2010**, 10, 1271.

[60] I. Song, C. Park, H. C. Choi, *RSC Advances* **2015**, 5, 7495.

[61] R. Kappera, D. Voiry, S. E. Yalcin, B. Branch, G. Gupta, A. D. Mohite, M. Chhowalla, *Nature Materials* **2014**, 13, 1128.

[62] H. Li, C. Tsai, A. L. Koh, L. Cai, A. W. Contryman, A. H. Fragapane, J. Zhao, H. S. Han, H. C. Manoharan, F. Abild-Pedersen, *Nature Materials* **2016**, 15, 48.

[63] B. Radisavljevic, A. Radenovic, J. Brivio, V. Giacometti, A. Kis, *Nature Nanotechnology* **2011**, 6, 147.

[64] J. Pu, Y. Yomogida, K.-K. Liu, L.-J. Li, Y. Iwasa, T. Takenobu, *Nano Letters* **2012**, 12, 4013.

[65] Y. Yoon, K. Ganapathi, S. Salahuddin, *Nano Letters* **2011**, 11, 3768.

[66] Y. Deng, Z. Luo, N. J. Conrad, H. Liu, Y. Gong, S. Najmaei, P. M. Ajayan, J. Lou, X. Xu, P. D. Ye, *Acs Nano* **2014**, 8, 8292.

[67] D. Lembke, A. Kis, *Acs Nano* **2012**, 6, 10070.

[68] M.-L. Tsai, S.-H. Su, J.-K. Chang, D.-S. Tsai, C.-H. Chen, C.-I. Wu, L.-J. Li, L.-J. Chen, J.-H. He, *Acs Nano* **2014**, 8, 8317.

[69] Q. H. Wang, K. Kalantar-Zadeh, A. Kis, J. N. Coleman, M. S. Strano, *Nature Nanotechnology* **2012**, 7, 699.

[70] G. Kline, K. Kam, D. Canfield, B. Parkinson, *Solar Energy Materials* **1981**, 4, 301.

[71] A. Goldberg, A. Beal, F. Levy, E. Davis, *Philosophical Magazine* **1975**, 32, 367.

[72] A. Laurie, D. J. Riley, *Journal of Materials Chemistry A* **2013**, 1, 8935.

[73] K. G. Zhou, N. N. Mao, H. X. Wang, Y. Peng, H. L. Zhang, *Angewandte Chemie International Edition* **2011**, 50, 10839.

[74] M. Buscema, J. O. Island, D. J. Groenendijk, S. I. Blanter, G. A. Steele, H. S. van der Zant, A. Castellanos-Gomez, *Chemical Society Reviews* **2015**, 44, 3691.

[75] J. Zhang, S. Najmaei, H. Lin, J. Lou, *Nanoscale* **2014**, 6, 5279.

[76] C.-J. Liu, S.-Y. Tai, S.-W. Chou, Y.-C. Yu, K.-D. Chang, S. Wang, F. S.-S. Chien, J.-Y. Lin, T.-W. Lin, *Journal of Materials Chemistry* **2012**, 22, 21057.

[77] S.-Y. Tai, C.-J. Liu, S.-W. Chou, F. S.-S. Chien, J.-Y. Lin, T.-W. Lin, *Journal of Materials Chemistry* **2012**, 22, 24753.

[78] M. Wu, Y. Wang, X. Lin, N. Yu, L. Wang, L. Wang, A. Hagfeldt, T. Ma, *Physical Chemistry Chemical Physics* **2011**, 13, 19298.

[79] G. Djemal, N. Müller, U. Lachish, D. Cahen, *Solar Energy Materials* **1981**, 5, 403.

[80] G. R. Bhimanapati, Z. Lin, V. Meunier, Y. Jung, J. Cha, S. Das, D. Xiao, Y. Son, M. S. Strano, V. R. Cooper, *Acs Nano* **2015**, 9, 11509.

[81] G. Eda, H. Yamaguchi, D. Voiry, T. Fujita, M. Chen, M. Chhowalla, *Nano Letters* **2011**, 11, 5111.

[82] M. Chhowalla, H. S. Shin, G. Eda, L.-J. Li, K. P. Loh, H. Zhang, *Nature Chemistry* **2013**, 5, 263.

[83] X. Huang, Z. Zeng, H. Zhang, *Chemical Society Reviews* **2013**, 42, 1934.

[84] V. Nicolosi, M. Chhowalla, M. G. Kanatzidis, M. S. Strano, J. N. Coleman, *Science* **2013**, 340, 1226419.

[85] J. H. Strait, P. Nene, F. Rana, *Physical Review B* **2014**, 90, 245402.

[86] H. Wang, C. Zhang, F. Rana, *Nano Letters* **2015**, 15, 8204.

[87] H. Shi, R. Yan, S. Bertolazzi, J. Brivio, B. Gao, A. Kis, D. Jena, H. G. Xing, L. Huang, *Acs Nano* **2013**, 7, 1072.

[88] H. Nan, Z. Wang, W. Wang, Z. Liang, Y. Lu, Q. Chen, D. He, P. Tan, F. Miao, X. Wang, *Acs Nano* **2014**, 8, 5738.

[89] S. Tongay, J. Zhou, C. Ataca, J. Liu, J. S. Kang, T. S. Matthews, L. You, J. Li, J. C. Grossman, J. Wu, *Nano Letters* **2013**, 13, 2831.

[90] J. Choi, H. Zhang, J. H. Choi, *Acs Nano* **2016**, 10, 1671.

[91] S. Mouri, Y. Miyauchi, K. Matsuda, *Nano Letters* **2013**, 13, 5944.

[92] M. A. Bork, C. G. Gianopoulos, H. Zhang, P. E. Fanwick, J. H. Choi, D. R. McMillin, *Biochemistry* **2014**, 53, 714.

[93] R. McGuire Jr, D. R. McMillin, *Chemical Communications* **2009**, 7393.

[94] M. C. Hersam, *Nature Nanotechnology* **2008**, 3, 387.

[95] H. Zhang, Y. Sun, K. Ye, P. Zhang, Y. Wang, *Journal of Materials Chemistry* **2005**, 15, 3181.

[96] P. Lugo-Ponce, D. R. McMillin, *Coordination Chemistry Reviews* **2000**, 208, 169.

[97] H. Zhang, B. A. Baker, T.-G. Cha, M. D. Sauffer, Y. Wu, N. Hinkson, M. A. Bork, C. M. McShane, K.-S. Choi, D. R. McMillin, J. H. Choi, *Advanced Materials* **2012**, 24, 5447.

[98] E. S. Jeng, A. E. Moll, A. C. Roy, J. B. Gastala, M. S. Strano, *Nano Letters* **2006**, 6, 371.

[99] D. Roxbury, X. Tu, M. Zheng, A. Jagota, *Langmuir* **2011**, 27, 8282.

[100] N. C. Maiti, S. Mazumdar, N. Periasamy, *Journal of Physical Chemistry B* **1998**, 102, 1528.

[101] I. Haq, J. O. Trent, B. Z. Chowdhry, T. C. Jenkins, *Journal of the American Chemical Society* **1999**, 121, 1768.

[102] N. W. Luedtke, *CHIMIA International Journal for Chemistry* **2009**, 63, 134.

[103] S. Burge, G. N. Parkinson, P. Hazel, A. K. Todd, S. Neidle, *Nucleic Acids Research* **2006**, 34, 5402.

[104] M. S. Dresselhaus, G. Dresselhaus, R. Saito, A. Jorio, *Physics reports* **2005**, 409, 47.

[105] M. Gouterman, *Journal of Molecular Spectroscopy* **1961**, 6, 138.

[106] J. Lang, M. Liu, *Journal of Physical Chemistry B* **1999**, 103, 11393.

[107] E. J. Gibbs, M. C. Maurer, J. Zhang, W. M. Reiff, D. T. Hill, M. Malicka-Blaszkiewicz, R. E. McKinnie, H. Liu, R. F. Pasternack, *Journal of inorganic biochemistry* **1988**, 32, 39.

[108] R. F. Pasternack, E. J. Gibbs, J. J. Villafranca, *Biochemistry* **1983**, 22, 5409.

[109] N. Shahabadi, S. Mohammadi, R. Alizadeh, *Bioinorganic Chemistry and Applications* **2011**, 2011, 429241.

[110] M. Tabata, K. Nakajima, E. Nyarko, *Journal of inorganic biochemistry* **2000**, 78, 383.

[111] F. J. Vergeldt, R. B. Koehorst, A. van Hoek, T. J. Schaafsma, *Journal of Physical Chemistry* **1995**, 99, 4397.

[112] P. M. Keane, J. M. Kelly, *Photochemical and Photobiological Sciences* **2011**, 10, 1578.

[113] A. M. Brun, A. Harriman, *Journal of the American Chemical Society* **1994**, 116, 10383.

[114] B. P. Hudson, J. Sou, D. J. Berger, D. R. McMillin, *Journal of the American Chemical Society* **1992**, 114, 8997.

[115] V. S. Chirvony, V. A. Galievsky, I. V. Sazanovich, P.-Y. Turpin, *Journal of Photochemistry and Photobiology B: Biology* **1999**, 52, 43.

[116] A. D. Awtrey, R. E. Connick, *Journal of the American Chemical Society* **1951**, 73, 1842.

[117] R. Gill, F. Patolsky, E. Katz, I. Willner, *Angewandte Chemie-International Edition* **2005**, 44, 4554.

[118] Y. M. Lin, J. Appenzeller, P. Avouris, *Nano Letters* **2004**, 4, 947.

[119] M.-H. Ha-Thi, N. Shafizadeh, L. Poisson, B. Soep, *The Journal of Physical Chemistry A* **2013**.

[120] W. S. Ross, C. C. Hardin, *Journal of the American Chemical Society* **1994**, 116, 6070.

[121] J. M. Wessels, M. A. Rodgers, *Journal of Physical Chemistry* **1995**, 99, 17586.

[122] J. W. Snyder, J. D. Lambert, P. R. Ogilby, *Photochemistry and Photobiology* **2006**, 82, 177.

[123] S. Hatz, L. Poulsen, P. R. Ogilby, *Photochemistry and Photobiology* **2008**, 84, 1284.

[124] S. Lebedkin, I. Kareev, F. Hennrich, M. M. Kappes, *Journal of Physical Chemistry C* **2008**, 112, 16236.

[125] M. Enescu, K. Steenkeste, F. Tfibel, M.-P. Fontaine-Aupart, *Physical Chemistry Chemical Physics* **2002**, 4, 6092.

[126] B. D. Sherman, M. D. Vaughn, J. J. Bergkamp, D. Gust, A. L. Moore, T. A. Moore, *Photosynthesis Research* **2014**, 120, 59.

[127] D. Gust, T. A. Moore, A. L. Moore, *Faraday Discussions* **2012**, 155, 9.

[128] D. Gust, T. A. Moore, A. L. Moore, *Accounts of Chemical Research* **2001**, 34, 40.

[129] S. D. Straight, G. Kodis, Y. Terazono, M. Hambourger, T. A. Moore, A. L. Moore, D. Gust, *Nature Nanotechnology* **2008**, 3, 280.

[130] J. D. Megiatto, A. Antoniuk-Pablant, B. D. Sherman, G. Kodis, M. Gervaldo, T. A. Moore, A. L. Moore, D. Gust, *Proceedings of the National Academy of Sciences* **2012**, 109, 15578.

[131] Y. Tachibana, L. Vayssieres, J. R. Durrant, *Nature Photonics* **2012**, 6, 511.

[132] M. T. Colvin, A. B. Ricks, A. M. Scott, A. L. Smeigh, R. Carmieli, T. Miura, M. R. Wasielewski, *Journal of the American Chemical Society* **2010**, 133, 1240.

[133] M. Kloz, S. Pillai, G. Kodis, D. Gust, T. A. Moore, A. L. Moore, R. van Grondelle, J. T. Kennis, *Chemical Science* **2012**, 3, 2052.

[134] M. Krieg, D. G. Whitten, *Journal of Photochemistry* **1984**, 25, 235.

[135] L. Bezdetnaya, N. Zeghari, I. Belitchenko, M. Barberl-Heyob, J. L. Merlin, A. Potapenko, F. Gulllemin, *Photochemistry and Photobiology* **1996**, 64, 382.

[136] J. Moan, K. BERG, *Photochemistry and Photobiology* **1991**, 53, 549.

[137] M.-H. Ham, J. H. Choi, A. A. Boghossian, E. S. Jeng, R. A. Graff, D. A. Heller, A. C. Chang, A. Mattis, T. H. Bayburt, Y. V. Grinkova, *Nature Chemistry* **2010**, 2, 929.

[138] Y. Li, R. Geyer, D. Sen, *Biochemistry* **1996**, 35, 6911.

[139] R. K. Jackson, A. Munro, K. Nebesny, N. Armstrong, S. Graham, *Acs Nano* **2010**, 4, 1377.

[140] H. Wójtowicz, M. Bielecki, J. Wojaczyński, M. Olczak, J. W. Smalley, T. Olczak, *Metallomics* **2013**, 5, 343.

[141] J. O. Calkins, Y. Umasankar, H. O'Neill, R. P. Ramasamy, *Energy & Environmental Science* **2013**, 6, 1891.

[142] F. D'Souza, S. K. Das, M. E. Zandler, A. S. Sandanayaka, O. Ito, *Journal of the American Chemical Society* **2011**, 133, 19922.

[143] C. Romero-Nieto, R. García, M. Á. Herranz, C. Ehli, M. Ruppert, A. Hirsch, D. M. Guldi, N. Martín, *Journal of the American Chemical Society* **2012**, 134, 9183.

[144] G. S. Cox, C. Bobillier, D. G. Whitten, *Photochemistry and Photobiology* **1982**, 36, 401.

[145] P. Travascio, Y. Li, D. Sen, *Chemistry & Biology* **1998**, 5, 505.

[146] P. George, D. Irvine, *Biochemical Journal* **1952**, 52, 511.

[147] Y. Miyata, Y. Maniwa, H. Kataura, *The Journal of Physical Chemistry B* **2005**, 110, 25.

[148] M. D. Ellison, L. K. Buckley, G. G. Lewis, C. E. Smith, E. M. Siedlecka, C. V. Palchak, J. M. Malarchik, *The Journal of Physical Chemistry C* **2009**, 113, 18536.

[149] M. S. Strano, C. B. Huffman, V. C. Moore, M. J. O'Connell, E. H. Haroz, J. Hubbard, M. Miller, K. Rialon, C. Kittrell, S. Ramesh, R. H. Hauge, R. E. Smalley, *The Journal of Physical Chemistry B* **2003**, 107, 6979.

[150] J. A. Imlay, S. Linn, *Science* **1988**, 240, 1302.

[151] K. Kalyanasundaram, *Inorganic chemistry* **1984**, 23, 2453.

[152] M. Ye, D. Winslow, D. Zhang, R. Pandey, Y. Yap, *Photonics* **2015**, 2, 288.

[153] A. Beal, J. Knights, W. Liang, *Journal of Physics C: Solid State Physics* **1972**, 5, 3540.

[154] I. De Wolf, *Semiconductor Science and Technology* **1996**, 11, 139.

[155] Z. Zhang, R. Hu, Z. Liu, *Langmuir* **2000**, 16, 1158.

[156] H. Tajima, K. Shimatani, T. Komino, S. Ikeda, M. Matsuda, Y. Ando, H. Akiyama, *Colloids and Surfaces A: Physicochemical and Engineering Aspects* **2006**, 284, 61.

[157] A. Kuc, N. Zibouche, T. Heine, *Physical Review B* **2011**, 83, 245213.

[158] E. Moons, A. Goossens, T. Savenije, *The Journal of Physical Chemistry B* **1997**, 101, 8492.

[159] N. Tao, *Physical Review Letters* **1996**, 76, 4066.

[160] K. Salazar-Salinas, L. A. Jauregui, C. Kubli-Garfias, J. M. Seminario, *Journal of Chemical Physics* **2009**, 130, 105101.

[161] T. Oku, T. Noma, A. Suzuki, K. Kikuchi, S. Kikuchi, *Journal of Physics and Chemistry of Solids* **2010**, 71, 551.

[162] T. B. Pinter, E. L. Dodd, D. S. Bohle, M. J. Stillman, *Inorganic Chemistry* **2012**, 51, 3743.

[163] A. R. Bizzarri, S. Cannistraro, *Chemical Physics Letters* **2004**, 395, 222.

[164] J. K. Ellis, M. J. Lucero, G. E. Scuseria, *Applied Physics Letters* **2011**, 99, 261908.

[165] Y. Park, V. Choong, Y. Gao, B. Hsieh, C. Tang, *Applied Physics Letters* **1996**, 68, 2699.

[166] T. Iyanagi, I. Yamazaki, K. F. Anan, *Biochimica et Biophysica Acta, Bioenergetics* **1985**, 806, 255.

[167] T. Cheiwchanchamnangij, W. R. Lambrecht, *Physical Review B* **2012**, 85, 205302.

[168] W. Zhao, Z. Ghorannevis, L. Chu, M. Toh, C. Kloc, P.-H. Tan, G. Eda, *Acs Nano* **2012**, 7, 791.

[169] W. Zhao, Z. Ghorannevis, K. K. Amara, J. R. Pang, M. Toh, X. Zhang, C. Kloc, P. H. Tan, G. Eda, *Nanoscale* **2013**, 5, 9677.

[170] K. Wang, Y. Feng, C. Chang, J. Zhan, C. Wang, Q. Zhao, J. N. Coleman, L. Zhang, W. J. Blau, J. Wang, *Nanoscale* **2014**, 6, 10530.

VITA

# VITA

## EDUCATION

Doctor of Philosophy in Mechanical Engineering, Purdue University
Expected Graduation: Dec. 2016
Major Professor: Dr. Jong Hyun Choi
Dissertation Title: *Photoelectrochemical and Photophysical Studies of Carbon Nanotube and Molybdenum Disulfide Based Light Harvesting Devices*

Master of Science in Mechanical Engineering, Purdue University Dec. 2012
Major Professor: Dr. Jong Hyun Choi
Thesis Title: *Understanding Photo-Conversion Processes in Chromophore – Carbon Nanotube Nanohybrids*

Bachelor of Science in Mechanical Engineering, Purdue University Aug. 2010

## PUBLICATIONS

1. T. Skwor, S. Klemm, H. Zhang, B. Schardt, S. Blaszczyk, and M. A. Bork, *Photodynamic Inactivation of Methicillin-Resistant Staphylococcus Aureus and Escherichia Coli: A Metalloporphyrin Comparison*, **Journal of Photochemistry and Photobiology B: Biology**, Submitted.
2. S. Ghimire, M. A. Bork, H. Zhang, P. E. Fanwick, M. Zeller, J. H. Choi and D. R. McMillin, *DNA Binding of Pd(TC3), a Conformable Cationic Porphyrin with a Long-Lived Triplet State*, **Dalton Transactions**, 45, 14277-14284 (2016).
3. H. Zhang, J. Choi, A. Ramani, D. Voiry, S. N. Natoli, B. G. Daum, M. Chhowalla, D. R. McMillin and J. H. Choi, *Engineering Chemically-Exfoliated Large-Area Two-Dimensional MoS2 Nanolayers with Porphyrins for Improved Light Harvesting*, **ChemPhysChem**, 17, 2854–2862 (2016)..
4. J. Choi, H. Zhang and J. H. Choi, *Understanding Environmental Effects on the Properties of 2D Transition Metal Dichalcogenides*, **ACS Applied Materials and Interfaces**, 8, 8864–8869 (2016).
5. H. Chen, H. Zhang, J. Pan, T. G. Cha, S. Li, J. Andréasson and J. H. Choi, *Dynamic and Progressive Control of DNA Origami Conformation by Modulating DNA Helicity with Chemical Adducts*, **ACS Nano**, 10, 4989–4996 (2016).

6. J. Choi, H. Zhang and J. H. Choi, *Modulating Optoelectronic Properties of Two-dimensional Transition Metal Dichalcogenide Semiconductors by Photoinduced Charge Transfer*, **ACS Nano**, 10, 1671–1680 (2016).
7. H. Zhang, J. Pan, S. Ghimire, M. A. Bork, M. M. Riccitelli, D. R. McMillin, and J. H. Choi, *Regeneration of Light Harvesting Complexes via Dynamic Replacement of Photodegraded Chromophores*, **ACS Applied Materials and Interfaces**, 7, 7833–7837 (2015).
8. H. Zhang, M. A. Bork, K. J. Riedy, D. R. McMillin, and J. H. Choi, *Understanding Photophysical Interactions of Semiconducting Carbon Nanotubes with Porphyrin Chromophores*, **Journal of Physical Chemistry C**, 118, 11612–11619 (2014).
9. M. A. Bork, C. G. Gianopoulos, H. Zhang, P. E. Fanwick, J.H. Choi, and D. R. McMillin, *Accessibility and External versus Intercalative Binding to DNA as Assessed by Oxygen-Induced Quenching of the Palladium (II)-Containing Cationic Porphyrins Pd (T4) and Pd (tD4)*, **Biochemistry**, 53, 714–724 (2014).
10. J. Pan, H. Zhang, T. G. Cha, H. Chen, and J. H. Choi, *Multiplexed Optical Detection of Plasma Porphyrins Using DNA Aptamer-Functionalized Carbon Nanotubes*, **Analytical chemistry**, 85, 8391–8396 (2013).
11. B. A. Baker, H. Zhang, T. G. Cha, and J. H. Choi, *Carbon Nanotube based Solar Cells*, edited by S. Yamashita, Y. Saito, and J. H. Choi in **Carbon Nanotubes and Graphene for Photonic Applications**, Elsevier (2013).
12. H. Zhang*, B. A. Baker*, T. G. Cha, M. D. Sauffer, Y. Wu, N. Hinkson, M. A. Bork, C. M. McShane, K. S. Choi, D. R. McMillin, and J.H. Choi, *DNA Oligonucleotide Templated Nanohybrids Using Electronic Type Sorted Carbon Nanotubes for Light Harvesting*, **Advanced Materials**, 24, 5447–5451 (2012).

## CONFERENCE PRESENTATIONS

1. H. Zhang and J. H. Choi, "*Understanding Photophysical Interactions of Semiconducting Carbon Nanotubes with Porphyrin Chromophores*", ASME International Mechanical Engineering Congress & Exposition (IMECE), Nov. 14-20, 2014, Montreal, Canada. (Poster)
2. H. Zhang and J. H. Choi, "*Dynamic Regeneration of Light Harvesting Complexes*", ASME International Mechanical Engineering Congress & Exposition (IMECE), Nov. 14-20, 2014, Montreal, Canada. (Poster)
3. H. Zhang, S. Ghimire, M. A. Bork, M. M. Riccitelli, D. R. McMillin, and J. H. Choi, "*Carbon Nanotube based Solar Cells That Can Regenerate*", ASME International Mechanical Engineering Congress & Exposition (IMECE), Nov. 14-20, 2014, Montreal, Canada.
4. H. Zhang, M. A. Bork, M. M. Riccitelli, K. J. Riedy, D. R. McMillin, and J. H. Choi, "*Understanding Photophysical Interactions of Semiconducting Carbon Nanotubes with Porphyrin Chromophores*", ASME International Mechanical Engineering Congress & Exposition (IMECE), Nov. 14-20, 2014, Montreal, Canada.

5. D. R. McMillin, M. A. Bork, H. Zhang, and J. H. Choi, "*The Ins and Outs of Single Oxygen Generation by Cationic Porphyrins*", 20th International Symposium on the Photophysics and Photochemistry of Coordination Compounds, Jul. 7-11, 2013, Traverse City, MI, USA.
6. H. Zhang, K. J. Riedy, and J. H. Choi, "*Carbon Nanotube Nanohybrids for Light Harvesting*", 2012 MRS Fall Meeting, Nov. 25-30, 2012, Boston, MA, USA.
7. H. Zhang, T. G. Cha, M. D. Sauffer, and J. H. Choi, "*Light Harvesting Carbon Nanotube Nanohybrids*", ASME Summer Heat Transfer Conference, July 8-12, 2012, Puerto Rico, USA.
8. H. Zhang, T. G. Cha, M. D. Sauffer, and J. H. Choi, "*Light Harvesting Single Wall Carbon Nanotube Hybrids*", 2012 MRS Spring Meeting, April 9-12, San Francisco, CA, USA.
9. H. Zhang, B. A. Baker, T. G. Cha, M. D. Sauffer, N. Hinkson, and J. H. Choi, "*DNA Oligonucleotide Programmed Assembly of Light Harvesting Carbon Nanotube Nanohybrids*", International Mechanical Engineering Congress & Exposition (IMECE), Nov. 11-17, 2011, Denver, CO, USA.
10. H. Zhang, B. A. Baker, T. G. Cha, M. D. Sauffer, N. Hinkson, and J. H. Choi, "*Biomolecular Manufacturing of Carbon Nanotube Devices*", ASME International Mechanical Engineering Congress & Exposition (IMECE), Nov. 11-17, 2011, Denver, CO, USA.

## TEACHING, MENTORING AND OUTREACH

- ME 315 Heat and Mass Transfer
  Laboratory instructor/ teaching assistant — Aug. 2014 – Dec. 2015
- ME 505 Intermediate Heat Transfer
  Teaching assistant — Aug. 2013 – May. 2014
- Senior graduate mentor for E-Mentoring Program new graduate students
  Collen Reidy, Johanna Palsdottir — Aug. – Dec. 2014
- Graduate mentor for Summer Undergraduate Research Fellowship (SURF) Students
  Adalberto Gonzalez, Kelley Riedy, Molly Riccitelli, Sawyer Morgan — 2012 – 2016
- Research outreach-engagement with high school students
  Arjun Ramani from West Lafayette High School, IN — Feb. – Aug. 2015
  Angela Filley from Harrison High School, IN — Feb. – May. 2013
- Volunteer for Purdue Nanodays, Birck Nanotechnology Center, West Lafayette, IN
  Developed a hands-on module for K-12 students, titled Glowing Grass: Observation of Photosynthetic Units — Apr. 2011 – 2015